Fall 2017

Explaining Creep-Like Deformation in the Marmara Sea: Results from AVO-Derived Vp/Vs and Pore Pressure Analysis

Rahmi M. Bolat
Southern Methodist University, rbolat@smu.edu

EXPLAINING CREEP-LIKE DEFORMATION IN THE MARMARA SEA: RESULTS FROM AVO-DERIVED Vp/Vs AND PORE PRESSURE ANALYSIS

Approved by:

_____

Prof. Matthew J. Hornbach
Professor of Geophysics

_____

Prof. Robert Gregory
Professor of Geophysics

_____

Prof. Brian Stump
Professor of Geophysics

_____

Prof. Donna J. Shillington
Lamont Associate Professor of Geophysics

_____

Prof. Maria Beatrice Magnani
Associate Professor of Geophysics

EXPLAINING CREEP-LIKE DEFORMATION IN THE MARMARA SEA: RESULTS FROM AVO-DERIVED Vp/Vs AND PORE PRESSURE ANALYSIS

Thesis Presented to the Graduate Faculty of

Dedman College

Southern Methodist University

in

Partial Fulfillment of the Requirements

for the degree of

Master of Science

Major in Geophysics

by

Rahmi Mert Bolat

BS., Geophysical Engineering, Istanbul University, Istanbul, Turkey

BS., Geological Engineering, Istanbul University, Istanbul, Turkey

December 16, 2017

ACKNOWLEDGMENTS

I am sincerely grateful to my supervisor Prof. Matthew J. Hornbach for his important guidance, support, encouragement and valuable discussions during the development of this thesis.

I would also thank my committee members for their guidance and patience, Prof. Maria Beatrice Magnani, Prof. Donna J. Shillington, Prof. Brian Stump and Prof. Robert Gregory.

Many of my friends helped me during this thesis I am grateful to all of them. I would thank to Benjamin Phrampus, Joe Batir, and all SMU Geothermal laboratory fellows.

I want to express sincere gratitude to Maria Richards and Oner Sufri for their help, generosity, and friendship.

A special thanks to my family. Without my parents' moral support, I would not have been able to take up this research, I am especially grateful to them.

Bolat, Rahmi Mert BS, Geophysical Engineering, Istanbul University, Turkey, 2012
BS, Geological Engineering, Istanbul University, Turkey, 2011

Explaining Creep-Like Deformation in the Marmara Sea: Results from AVO-Derived Vp/Vs and Pore Pressure Analysis

Advisor: Professor Matthew J. Hornbach

Masters conferred December 16, 2017

Thesis completed August 14, 2017

Recent studies suggest that high pore pressures have caused seafloor creep-like deformation and slope failure in the Marmara Sea (e.g. Shillington et al., 2012). Stratigraphic analysis provides evidence for creep-like deformation in Marmara Sea sediments, however, no detailed quantitative geophysical analysis has been conducted to determine whether elevated fluid pressures exist in the Marmara Sea sediments today, or if these sediments are potentially near-critically stressed. If fluid pressures are high and the sediments are close to failure, only minor ground accelerations from earthquakes along the active Northern Anatolian Fault might trigger failure. For this study, I use high resolution multichannel 2D seismic data collected in the Marmara Sea to estimate indirectly P-wave and S-wave velocities that I then use to detect both possible gas accumulations and zones of high pore pressure. Specifically, I integrate interval P-wave velocities (using Dix equation), rock physics models, and Amplitude Versus Offset (AVO) methods to estimate Vs velocities. With Vp and Vs constrained, I then estimate where elevated fluid pressures in shallow (<500 mbsf) sediment might exist in sediments on the southern margin of the Marmara Sea where pressure-driven creep-like deformation is hypothesized. I first characterize using forward models what normal versus overpressured AVO and Vp/Vs response should be like in the environment. Then, I compare model predictions with observations in a zone where creep-like

deformation exists. The final product provides evidence for both if and where elevated pore pressure likely exists along the zone of noted sediment creep. I conclude by noting how sediment mineralogy and sedimentation rates likely play an important role in characterizing pore pressure evolution along this margin.

TABLE OF CONTENTS

LIST OF FIGURES

LIST OF TABLES

INTRODUCTION

AVO is a tool routinely used for gas detection, and, in the right instances, can be used to estimate Shear wave velocity (Vs), and, combined with P-wave velocity (Vp) measurements, can be used to detect zones of high pore pressure (Nur et al., 1998; Mavko et al., 2009). Previous seismic studies that carefully analyze sediment stratigraphy and deformation in the Marmara Sea suggest high pore pressure drives slope failure in the Marmara Sea (Shillington et al., 2012). To date, however, no direct evidence (via drilling, velocity analysis, or pore pressure measurements) exists to confirm this hypothesis. The objective of this study is to assess pore pressure in suspected over pressured sediments in the Marmara Sea using seismic techniques, specifically, seismic velocity/AVO analysis combined with rock physics modeling. To do this, I first estimate expected AVO and Vp/Vs responses due to different scenarios such as overpressure and gas in sediments using simplified numerical forward models. Then, by comparing these forward model velocity/AVO estimations with both AVO observations estimated Vp/Vs velocities and sediment properties in the Marmara Sea, I place bounds on the pore pressures and free gas values that likely exists in the region. The analysis integrates uncertainties in sediment density, porosity and mineralogy in the region to draw conclusions regarding the cause of different seismic velocity/AVO responses in the Marmara Sea. Using these data, I determine if and where gas and perhaps elevated pore fluid pressures in the region exists, and, hypothesize why we observe these features.

CHAPTER 1

1.1 Geologic Setting

The Marmara Sea (Figure 1) formed as a result of uplift and erosion of the Intra-Pontide Suture Zone during the early Miocene (Gorur et. al., 1984). It is located in the middle of a seismically and tectonically active compressional Anatolian and extensional Aegean Sea regions (Figure 1). The North Anatolian Fault Zone (NAFZ), a right-lateral strike-slip fault system that defines the boundary between the Eurasian Plate to the north and the Anatolian micro-plate to the south, passes through the Marmara Sea (e.g. Kahle et. al., 1997). This fault system consists of three major fault segments which are the North Boundary, the Central and Ganos fault segments. The Central Marmara fault segment, approximately 105 km long, is longer than the North Boundary and Ganos fault segments (Okay et al., 2000) (Figure 3).

The motion along the NAFZ is not purely strike-slip, and the basins in the Marmara Sea shows both compressive and extensional pull-apart characteristics. The main basins located from west to east by name are the Tekirdag, Central, and Cinarcik Basins (Fig. 3). Active tectonics in the Marmara Sea result in submarine ruptures, scarps, and folds (e.g., Armijo et al., 2005).

The Marmara Sea region is under the strike-slip regime, it has also experienced significant extension. Additionally, the Central Basin has transtension characteristic along the North Anatolian strike slip fault (Bécel et al., 2010). The Thrace Basin opened during the Middle Eocene-Eocene period (Figure 3). A second stage of extension occurred during the late Miocene through

Quaternary (Aksoy et al., 1997). Paleotectonic belts show a NE-SW trend, and the basins are filled with Eocene and younger age sediments (Wong et al., 1995).

Due perhaps to significant variations in tectonic activity and seismicity, the Marmara Sea has different sedimentation rates in different regions. Previous studies utilizing core samples indicate sedimentation rates of 0.52 m/kyr on the inner southern shelf with lower values of 0.18 m/kyr on the outer shelf in the same region. This decrease continues northward, reducing to 0.1 m/kyr on the northern shelf (Cagatay et al., 2000). All of these values, however, are generally higher than sedimentation rates observed on typical sediment continental margins (e.g. Mueller & Suess, 1979). The Tekirdag, Central and Cinarcik basins, which have an average sediment thickness of 6 km, have subsidence rate of 5-6 mm/yr with 1-3 mm/yr sedimentation rate during the last 15.000 years (Beck et al., 2017). In contrast, the Western and Central Highs, where my study area is located, have an estimated average sedimentation rate of 0.2-0.5 mm/yr during the last 70.000 years according to core studies (Cagatay et al, 2017).

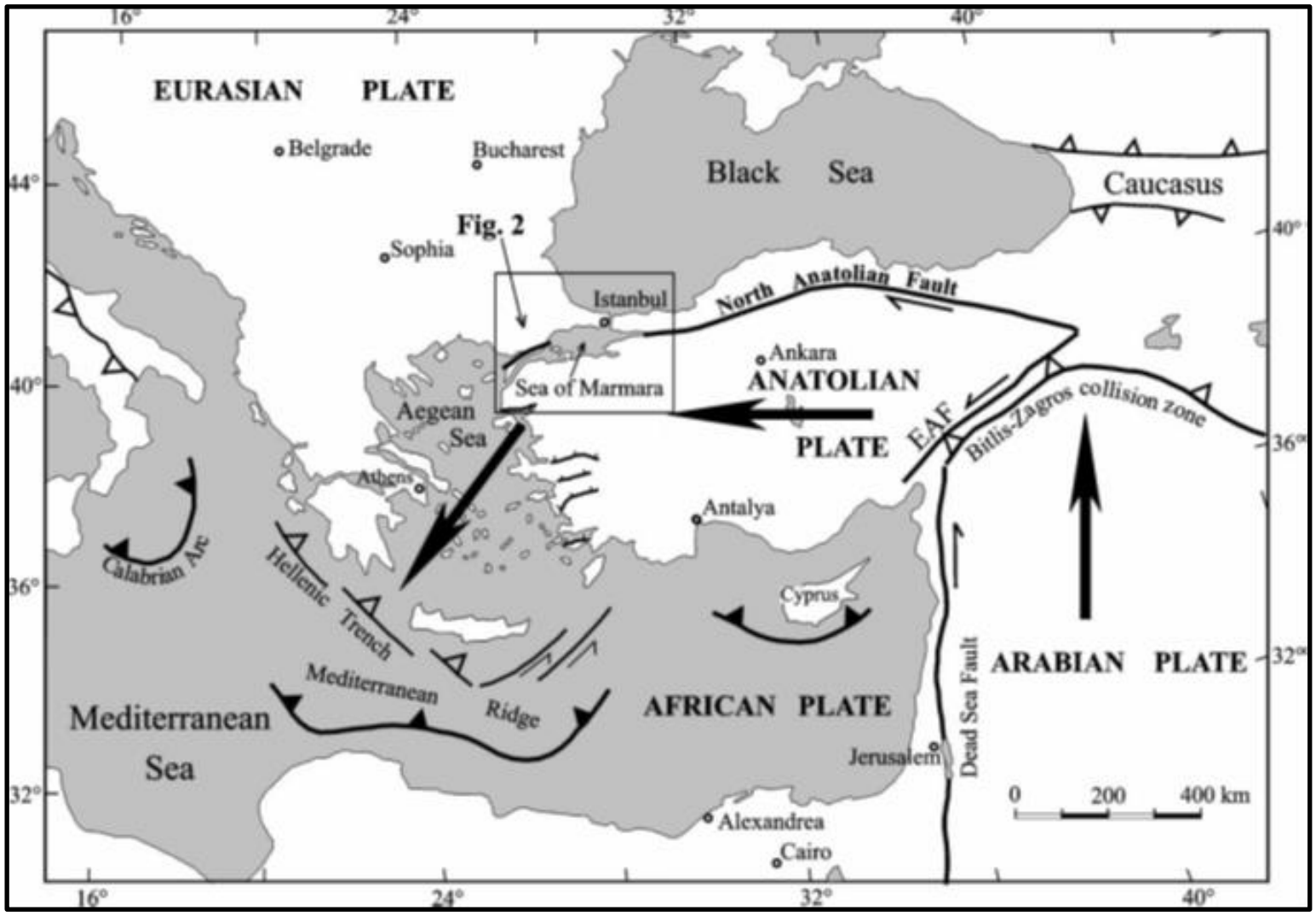

Figure 1 Regional map showing active tectonic regime in the Marmara Sea and southwestern Turkey (adapted from Okay et al., 2000). The large solid arrows are showing the motion of three lithostraphic plates in relates with the Marmara Sea.

Figure 2 Regional fault map and tectonics of the North Anatolian Fault (NAF) System for the Marmara Sea. The seismic line used for this study, located along the central high, is and shown in red.

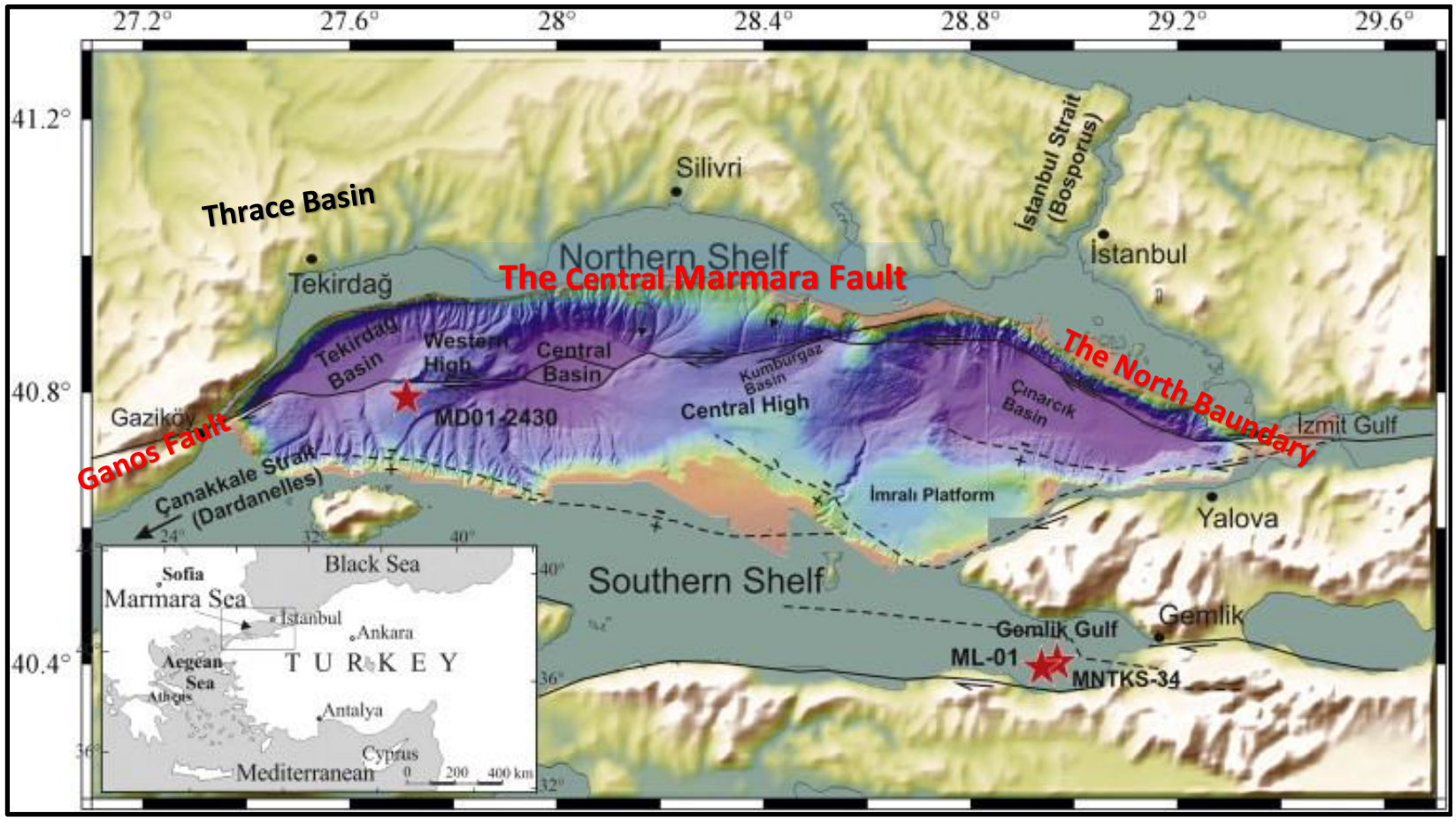

Figure 3 The Marmara Sea morphology (Adopted from Cagatay et al., 2015) Red stars are showing the location of the studied sediment cores in different areas in the Marmara Sea.

1.2 Tectonics

The Marmara Sea, an inland sea between the Black Sea and the Aegean Sea, is a tectonically active region influenced by the North Anatolian Fault Zone (NAFZ; Sengor et al., 2004). The northern part of the Marmara Sea is structurally shaped by the north branch of NAFZ, and has three main basins (Barka, 1997; Le Pichon et al., 2000; Okay et al., 1999, 2000; Imren et al., 2001), all related to the right stepping nature of the NAFZ (Gurer et. al., 2003) (Fig. 3). The basins along the NAFZ are shaped by normal faults, and they are also separated by transform faults which formed NE-SW anticlines. Both normal faulted shaped basins and transform faulted shaped anticlines form a parallel series of depocenters-anticlines overlain by younger sediments (Rangin et al., 2004).

The region is rich in hydrocarbon gases, which are observed as gas emissions at the sea floor especially in the continental shelf areas (Dupre et al., 2015). Under low temperature-high pressure conditions these gases can form gas hydrate crystals in sediments, and there is evidence that this occurs in the Marmara Sea at water depths greater than 660 m (Bourry et al., 2009). Previous research has already shown that gas anomalies and gas emissions often occur in the water column along or near active submarine fault segments (Dupre et. al., 2015). Gas hydrate and gas bubbles samples obtained from the Western High, Central High and Cinarcik Basin were chemically analyzed to determine that much of the gas from the Western High is thermogenic in origin, while gas from the Thrace Basin (figure 3) is primarily biogenic (Le Pichon et al., 2001; Bourry et al., 2009; Géli et al., 2010; Tary, 2011; Ruffine et al., 2012; Dupre et al., 2014).

The Eocene-Oligocene aged Thrace basin deposits, located in the northern part of Central High, are the likely source rocks of Central High gases (Bourry et al., 2009), as the gas samples taken from the Western High and Central High were observed to have a high ^{13}C (depleted

methane) ratio consistent with carbon from thermally altered carbon reservoirs (Bourry et al., 2009).

Since these gases formed in deeper marine environment settings as a result of decomposition of organic matter by thermal cracking, their existence at the seafloor indicates upward fluid migration (Dupre et al., 2015). Reservoirs where this gas is trapped may become pressurized with time, promoting possible overpressure and slope failure.

Gas emissions are also observed south of the NAFZ and Central High anticlinal structure, although no clear fault control associated with gas migration is observed in this region. Additionally, this region shows clear evidence of recent submarine landslides on the sea floor (Dupre et al., 2015). The deformed folded seabed with sediments progressively more deformed with depth, combined with no clear evidence for fault-controlled gas migration or emissions might support the idea that there is a creeping type deformation that develops as a result of high pore fluid pressure or high gas concentration in sediments as suggested in previous studies (Shillington et al., 2012; Dupre et al., 2015; Tary et al., 2014).

The Marmara Sea region has experienced many large earthquakes with destructive consequences (Hébert et al. 2004). During the last 2000 years, earthquakes of Mercalli Scale Magnitude VII to VIII occurred in the Marmara Sea on average every 50 years, with events of MM VIII-IX intensity every 250-300 years. The NAFZ has an average slip rate of 20-25 mm/yr along the Marmara Sea Basin (Barka, 1992; Pinar et al., 2001). The most recent devastating earthquake on this fault zone was the 1999 Izmit earthquake (M 7.4), which was also the last massive earthquake in the Marmara Sea province. It caused approximately 17,000 casualties, and left approximately half million-people homeless (Marza, 2004).

The North Anatolian Fault segment crossing the Central High has not ruptured since 1776 (Géli et al., 2010), and there is an absence seismicity northwest of this ridge (Kumburgaz Basin) (Schmittbuhl et al., 2016). The region may, therefore, be due for a large earthquake. This, combined with possible over pressured sediment in this region could lead to slope failures and possible tsunami generation.

Tsunami hazard models assuming typical seismic events of ~ M7 can produce tsunami waves of 1-2 m could affect the northern and southern coasts of the Marmara Sea (Yalciner et al., 2002). However, these estimates are lower than observed tsunami wave heights following the 1509, 1766, 1894, 1912, and 1999 earthquakes (Altinok et al., 2001). One possible explanation for this discrepancy is that modelled tsunami waves account only for earthquake deformation, and not slide-generated waves that may have also contributed more energy than calculated assuming only seismic seafloor deformation (MARSite_Annual_Public_Report-3).

In this study, I analyze one 2D seismic line collected on the Central High between the Central and Cinarcik Basins. This ridge is located at the southern end of the NAFZ strike-slip fault strand and has a NNE-SSW trend (Bourry et al., 2009) (Figure 3). I focus on this seismic line because it images potential creeping slope failure events that may have been triggered by elevated fluid pressures (Shillington et al., 2012). To assess whether high pore pressure exists at this site, I process and analyze a multichannel 2D seismic line collected in the southern part of the Central High. Specifically, I determine Vp velocities, and, using AVO methods, estimate Vs velocities in order to constrain Vp/Vs ratios of the sediment. I then compare our result with “normal” Vp/Vs ratios for marine margin sediments using standard rock-physics models to determine if and where velocity anomalies might indicate elevated fluid pressures exist.

CHAPTER 2

2.1 Methodology: Assessing Pore Pressure and Detecting Gas with Seismic Waves:

Two important types of seismic waves in seismology are P-waves and S-waves. P waves are compressive waves that propagate in the direction of particle motion. S-waves, or shear waves, propagate perpendicular to the particle motion.

Seismic S-waves and P-waves (Vs and Vp) are influenced by the density and elastic parameters of the media they travel:

$$V_P = \sqrt{\frac{K + 4/3\,\mu}{\rho}} \qquad \text{and} \qquad V_S = \sqrt{\frac{\mu}{\rho}} \tag{1}$$

where K (Pa) is bulk modulus, μ (Pa) is shear modulus, and ρ (kg/m^3) is density. The bulk modulus (the inverse of compressibility) defines the resistance of the material to compression and defines the ratio of hydrostatic stress to volumetric strain. Higher K values indicate smaller volume changes and the large stiffness of the rocks.

Shear modulus measures the resistance of rocks to shear deformation or shape change. It also defines the ratio of shear stress to shear strains. The μ values approach zero in the absence of shear stresses, such as liquid media. Therefore, S-wave velocities cannot be observed in fluids produce

compressive motion in the direction of particle motion causing both volumetric deformation and shape change in the rock. S-wave propagation causes only shape change, thus no volumetric deformation. Consequently, bulk modulus does not have any effect on S-wave velocities.

The ratio of these elastic parameters along with rock density controls the seismic velocities. The type of pore fluids strongly influences the elastic parameters of the rock and both Vp and Vs.

2.1.1 Saturation Dependence

Fluids located in the rock/sediment matrix play an important role in changing the sediment matrix density and elastic properties, and therefore, impact Vp and Vs. P-wave and S-wave velocities show different reactions to saturation of different pore fluids. This is because different percentage of pore fluids have different bulk modulus and also have different fluid densities. For instance, laboratory measurements in rock document an increase in P-wave velocity with increasing water saturation. These results showed that bulk modulus is more sensitive to fluid saturation than shear modulus (Han&Batzle, 2001). Water has a low compressibility (larger bulk modulus). The increase in water saturation in pore space, makes the rock frame more resistant to volumetric deformations along P-wave propagation with less compressible water filling pores. This effect results in higher P-wave velocities. In contrast, S- wave velocities are not influenced by pore fluid variations. While the volume of pore spaces in rocks are deformed by seismic wave propagations, the shape of the pores remains the same. Thus, the shear modulus of the rock is equal to the dry rock frame shear modulus (Gassman, 1951). To clarify this, I used arrows showing increasing (↑), decreasing (↓), and stable (↔). Elastic constants,

$$\uparrow \quad Vp = \sqrt{\frac{\uparrow K + \frac{4}{3} * \mu \ \leftrightarrow}{\rho \ \downarrow}}$$

(2)

Where gas (a high compressible fluid with low K) fills the pore space, rather than water, the saturated rock frame does not resist volumetric deformations caused by wave propagation. The stiffness of the rock frame drops, and consequently P-wave velocities are reduced. As in the water saturation case, gas saturation has no impact on the shear modulus (μ). The saturated shear modulus is equal to the dry frame rock shear modulus.

$$\downarrow \quad Vp = \sqrt{\frac{\downarrow K + \frac{4}{3} * \mu \ \leftrightarrow}{\rho \ \downarrow}}$$

(3)

The effect of different types of pore fluids on seismic velocities can be calculated from laboratory measurements of dry rock samples by using fluid substitution (Gassmann, 1951, the equations noted below). Gassmann's equations assume the porous media is isotropic and porous (a good assumption for deep-water marine sediments, e.g. Dvorkin et al., 1999).

$$Ks = Kdry + \Delta\text{Kdry}$$

$$\Delta\text{Kdry} = \frac{Kmin(1 - \frac{Kdry}{Kmin})\text{^}2}{1 - \varphi - \frac{Kdry}{K0} + \varphi * Kmin/Kf}$$

$$\mu s = \mu dry$$

(4)

Where Kmin, Kf, Kdry, and Ks, are the bulk modulus (Pa) of mineral, fluid, dry rock and the saturated rock frame (Pa), φ is porosity, μdry and μs are the dry and saturated bulk modulus (Pa).

Gassmann's equations are often integrated into effective medium models to assess physical properties of marine sediments (e.g. Dvorkin et al., 1999; Mavko 2009), and in instances where sediment properties are well constrained, to estimate *in situ* porosity, mineralogy, and gas concentration (e.g. Helgerud, 1999; Dvorkin 1999a, 1999b).

The assumptions that go along with the Gassmann equations are important and have key roles in calculations of seismic velocities. However, they might not be sufficient for real reservoir rock physics. For instance, in these assumptions the values for shear modulus are independent of fluid substation and not affected by any fluid saturations. Pores are well connected in rock, and pore fluids are able to flow between these pore spaces. In some cases where pores are not interconnected, shear stress cannot be transferred between pore spaces, and mineral grains lose their contacts with each other. In this case, pressure increases in pores and makes pore fluids less compressible and the shear strength (low μ) of rock frame is reduced (Mavko, 2005).

2.1.2 How pore pressure affects Vp and Vs

It is well recognized that pore pressure has a non-linear effect on Vp and Vs, and that S-wave velocities are particularly sensitive to pore pressure (e.g., Prasad, 2002). As pore fluid pressure increases, Vp values decrease toward water velocities (~1500 m/s), while Vs values drop proportionally much more, ultimately approaching zero as critical pore pressures develop.

Dvorkin & Nur (1999), Mavko (2009) and Hornbach & Manga (2014) have shown that pore pressure can be estimated in effective medium models using a first-principles approach if sediment porosity, mineralogy and physical properties are well constrained. This approach has been used with success in marine sediments to constrain *in situ* pore pressure in deep water environments and provides a useful technique for estimating pore fluid pressure indirectly using only Vp, Vs, and basic rock properties data. Detection and quantification of elevated pore pressure is difficult

using these methods, requiring high-quality (ideally down-hole) mineralogy, porosity, and especially Vp and Vs data (e.g., Hornbach and Manga, 2014; Hornbach et al., 2015). This is due to the non-linear effect of pore pressure on Vp and Vs. Nonetheless, this approach works well in extreme instances where pore pressure approaches lithostatic levels --levels within 10-20% of those necessary for hydraulic failure (e.g., Hornbach and Manga, 2014).

As mentioned before, increased pore pressure impacts the pore fluids, and results in an increased bulk modulus (K). Shear modulus drops, and S-wave velocity drops more significantly than P-wave velocities since the increase in bulk modulus is able to balance large decrease in shear modulus. This relation is clearly observed in the seismic velocity equations (Eq 1).

$$\downarrow\downarrow \ Vs = \sqrt{\frac{\mu \downarrow\downarrow}{\rho \downarrow}} \qquad \downarrow approach \sim 1500 m/s \ Vp = \sqrt{\frac{\uparrow K + \frac{4}{3} * \mu \downarrow\downarrow}{\rho \downarrow}} \tag{5}$$

In previous studies, *in situ* pore pressure measurements and estimates of pore pressure ratio had been constrained from consolidation tests during integrated borehole drilling. Additionally, seismic interval velocities, and reflection tomography methods were used where *in situ* measurements were absent (Sayers et al., 2002; Hornbach and Manga, 2014).

2.1.3 Pore Pressure and Effective Stress Dependence

Besides fluid saturation and fluid type, seismic velocity is also affected by fluid pore pressure as mentioned the previous section. Hydrostatic pressure, the pressure caused by the weight of overlying water, is calculated directly by estimating the weight of a water column (ρ*g*h), where ρ is water density, g is gravitational acceleration (9.8 m/s^2), and h is the height of the water column (m). A marine sediment matrix that is normally pressured (not over pressured) experiences hydrostatic pressure. A system under hydrostatic pressure implies interconnected pore spaces that allow communication of fluid between pores. In contrast, lithostatic pressure is the pressure caused by all overlying materials (including not only the weight of the water but the overlying sediment).

The lithostatic pressure is therefore calculated by multiplied by bulk density of the overlying sediment ρ_b (including fluids in the pore space), ($\frac{kg}{m3}$), by the height of the material (m) and gravity, g=9.8 m/s^2. Lithostatic pressure represents the maximum pressure a system can experience before hydraulic fracturing occurs. This is because sediments under lithostatic pressure feel the full weight of both fluids and sediments above, and the pressure in these sediments equals the full weight of the water and sediment above. In this case, the pressure therefore equals the weight of the overburden. At this pressure, the grain contacts are at or near failure, since at the micro scale, the pore pressure is at lithostatic values, and is pushing back on the grains with a value equal to the overlying weight of the sediment matrix. When lithostatic pressures exist, the system is at failure, grains act almost like fluids, and shear strength approaches zero.

$$(approaches\ zero) \downarrow\downarrow \quad Vs = \sqrt{\frac{\mu \ \downarrow\downarrow (approaches\ zero)}{\rho \ \downarrow}}$$

(6)

In most instances, the fluid pressure in marine sediments falls somewhere between hydrostatic and lithostatic values, since some sedimentary layers are more porous and permeable than others. The effective pressure or stress, is defined as the difference between lithostatic pressure (the pressure required for hydraulic fracturing) and the *in situ* pore fluid pressure.

$$The\ Effective\ Stress = Lithostatic\ Stress - Pore\ Fluid\ Pressure$$

(7)

If the pore fluid pressure is hydrostatic, the effective stress equals the following:

$$\sigma_1 = \rho_b * depth * 9.8 - \rho_W * depth * 9.8$$

(8)

However, if pore fluid is elevated, the effective stress converges towards zero as pore-fluid pressures approach lithostatic.

Under normal marine deposition conditions where sediments have higher porosity/ permeability, sedimentation rates are low, and pores are interconnected, so the weight of overlying rock is not "felt" by the pore fluids, and we can assume a hydrostatic pore pressure condition. In a normal hydrostatic system where sediments have high permeability, the pore fluid pressure follows hydrostatic pressure gradient with depth since the fluids in the sediment pores only feel the pressure of the water column within the above sediments. In cases where sediments are low permeability and fluids are not fully interconnected between pores, or sedimentation rates are high

and fluids cannot drain easily, the pore fluid pressure may be elevated above hydrostatic pressure. In this instance, pore fluid pressure stops following a hydrostatic pressure gradient, and overpressures develop as pore fluids feel the weight not only of the overlying water but sediment matrix (Figure 4).

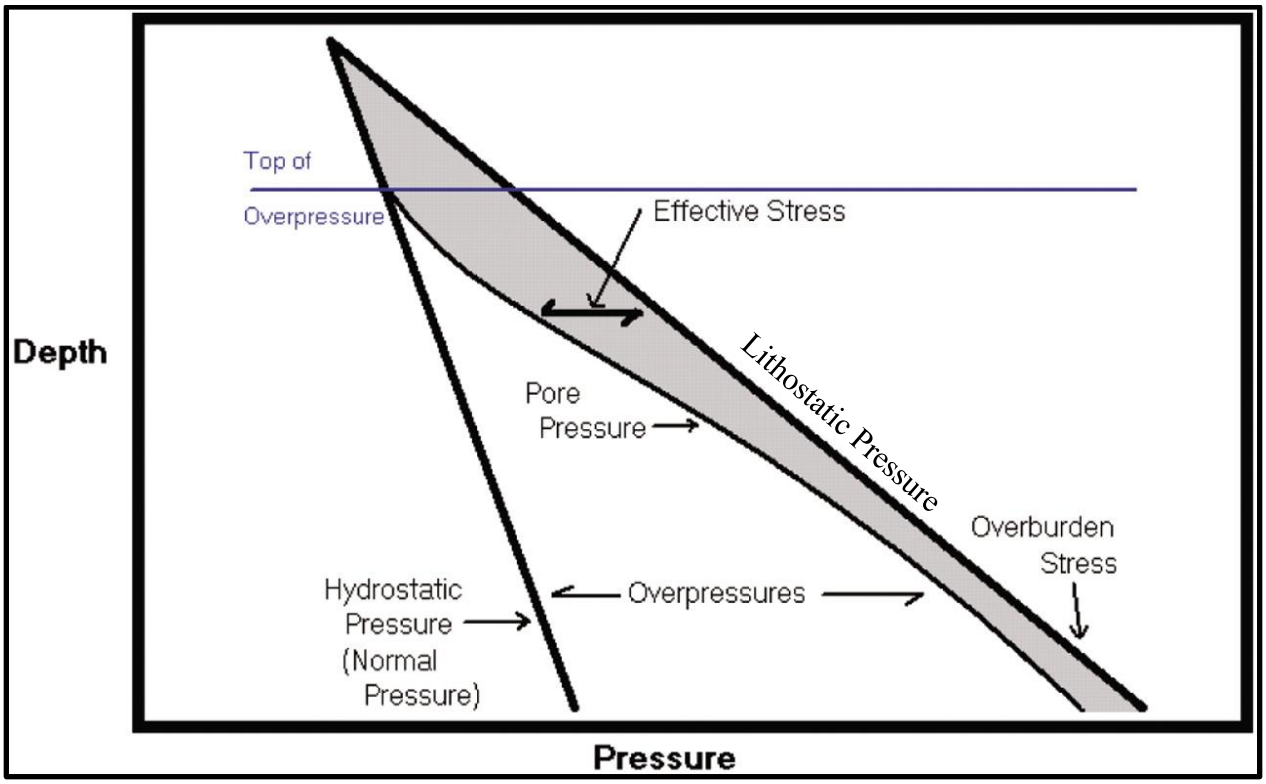

Figure 4 Elevation of pore fluid pressure. At the top of overpressure zone, pore fluid pressure departs from hydrostatic pressure gradient and approaches confining pressure gradient. The effective stress also reduces inversely with the elevated pore pressure ratio, and overpressure arises in sediments (Adopted from Bruce and Bowers, 2002).

One simple way to assess the level of overpressure in sediment is to use the pore pressure ratio (λ*), which is defined as the measured fluid pressure above hydrostatic divided by the hydrostatic effective stress:

$$\lambda^* = \frac{P^*}{(\sigma_1 - P_h)} \tag{9}$$

Here, P* is the measured fluid pressure above hydrostatic. Note that λ* is zero when P* is zero (pore pressure is hydrostatic), and λ* is 1 when the effective pore pressure is lithostatic and the system is at failure. Hornbach and Manga (2014) demonstrate that for typical shallow (<200 mbsf) marine sediments, pore pressure ratio (λ*) values in excess of 0.6 are detectable if Vp and especially Vs velocities are well constrained (Figure 5).

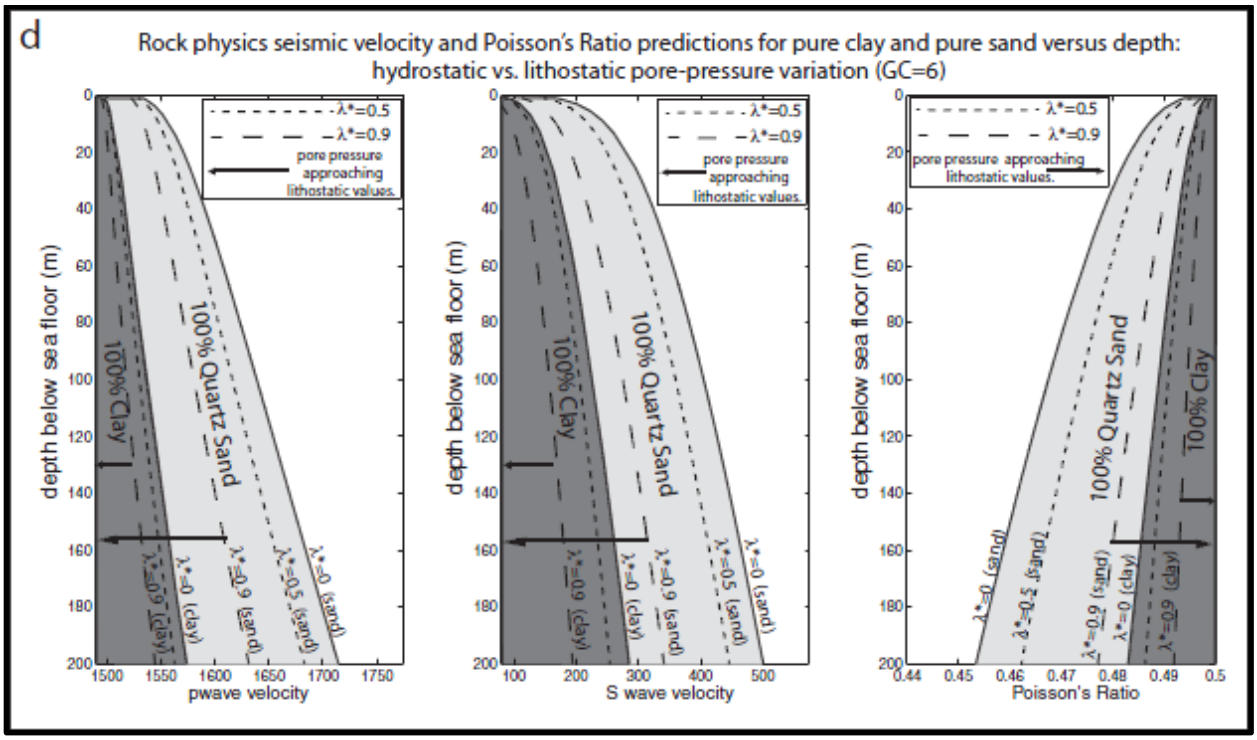

Figure 5 Estimates of seismic velocities and Poisson's Ratio depend on pore fluid pressure variations for pure clay and pure sand versus depth (adopted from Hornbach and Manga, 2014). Note that Vs is significantly more sensitive to pore pressure compared to Vp, with Vs velocities reducing to zero as pore pressure approaches lithostatic values.

2.2 Vp/Vs ratios as a first order tool for detecting elevated pore pressure

In the past, numerical models used P-waves velocities to make rough estimates of where high pore pressures exist (e.g Dutta, 2002). This method is problematic, since P-wave velocities decreases under conditions of overpressure and pore-fluid content (e.g., the presence of gas). In contrast, Vs decreases only with overpressure and is unaffected by changes in fluid properties (gas versus water filling pore space) as long as no significant changes in fluid pressure occur.

Thus, more recent studies have used both Vp and Vs, and, in particular Vp/Vs ratios to detect where elevated fluid pressures exist (e.g. Prasad, 2002; Hornbach et al., 2015). For example, Prasad analyzes the sensitivity of seismic velocities to overpressure in different grain sized sands;

he observed significant differences between P-waves and S-waves responses. This is because as pore pressure increases, Vs velocities decrease significantly faster more than Vp velocities (as shown in equation 5 and discussed in section 2.1.2), with Vp/Vs ratios increasing above values of 5 in zones of overpressure (Figure 6). Under normal marine depositional conditions where normal consolidation with depth occurs, the Vp/Vs ratio follows a clear and a predictable pattern (Figure 6).

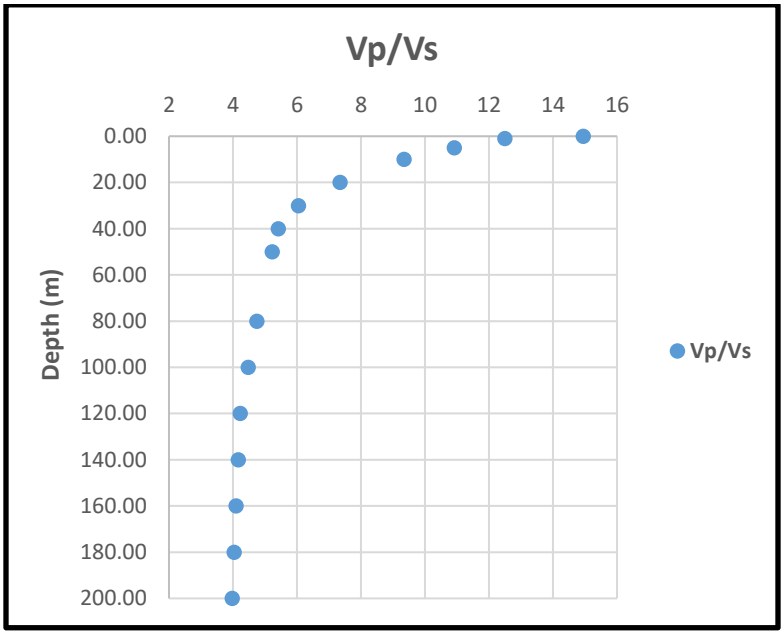

Figure 6 Vp/Vs ratio for initial 200 m below seafloor (0 depth). Note, how values converge with depth as the sediments become more compacted (Hamilton, 1979).

For typical marine environments Hamilton (1979) assumes soft marine sediments are fully saturated, consisting of soft mudstones and shales, that grade with depth. Vp/Vs ratio is about 13 at the sea floor and about 2.6 at 1000 m depth (Hamilton, 1979). It has a very high gradient in the upper 50 m of sediments, and generally ranges between 2 and 5 (Figure 6). However, if trace

amounts of gas are present in the pore space, Vp drops while Vs is unaffected, resulting in anomalously low Vp/Vs values below 2. In contrast, if pore pressure increases, Vs values drop significantly compared to Vp values (that can only reduce to ~1500 m/s), and as a result, Vp/Vs values are anomalously high.

The Vp/Vs ratio provides a simple first-order tool for assessing both where trace amounts of gas fill pore space (low Vp/Vs) or significant over pressures might exist (high Vp/Vs). By assessing both Vp and Vs, and analyzing the Vp/Vs ratio, I can therefore make a first order estimate to determine if and where elevated pore fluid pressure potentially exists, or whether zones have high gas content. Obviously, if both exist, there will be some ambiguity, and addressing this issue is beyond the scope of this study (and likely requires higher resolution data, and ideally, down-hole measurements). The key issue in using Vp/Vs ratios, is the need for Vs data at the site. Specifically, Vp is routinely estimated using multichannel CMP gathers and Dix's equation. Vs, however, is more difficult, as there is no direct measurement for shear velocity. I discuss how to obtain first-order estimates for Vs in the following section.

2.2.1 Obtaining Vs: AVO as a tool for quantifying Vs and detecting high fluid pressure

Although, ideally, rigid physical properties measurements are needed to make high-precision pressure estimates in marine environments (e.g., Hornbach & Manga, 2014), an alternative first order method can be used to determine if or where near-critical pore pressures exist in the subsurface if we know Vp and Vs seismic velocities. A major problem with using Vs data to estimate pore fluid pressure in the marine environment is that Vs data are not routinely available. Vp data are easily estimated using multichannel seismic methods and the Dix equation (Dix, 1955). In contrast, Vs data are rarely collected, because collecting such data is difficult and expensive, requiring coupling to the seafloor via ocean bottom cable or ocean bottom seismometers to account

for shear effects. Nonetheless, there is an indirect way we can estimate Vs values using amplitude versus offset techniques. When seismic wave encounters an interface between two layers with different P-wave and S-wave, part of the wave energy is reflected while another part is refracted. Additionally, if the wave is not at zero incidence angle, part of the wave is converted to S-waves that are also reflected and refracted. In an isotropic medium the S-wave is polarized in both vertical plane and horizontal plane as Sv and S_H waves. Karl Heinz Zoeppritz (1919) describes this relationship between the amplitudes of the incident P-wave, and transmitted P and S waves as a function of incidence angle. Zoeppritz equations (table 1) show that wave amplitude depends on the angle of incidence. These equations are simplified by linearization in Aki-Richards (1980) and Shuey (1985) three-term approximations (table 2). Both of them are not interested in S_H wave component in their approximations. They assume reflected S-waves equal to reflected S_V wave component (Figure 7). Wave amplitudes for both Vp and Vs depend on not only the angle of incidence, but also on physical parameters such as density, bulk and shear moduli (Aki and Richards, 1980) of the rocks.

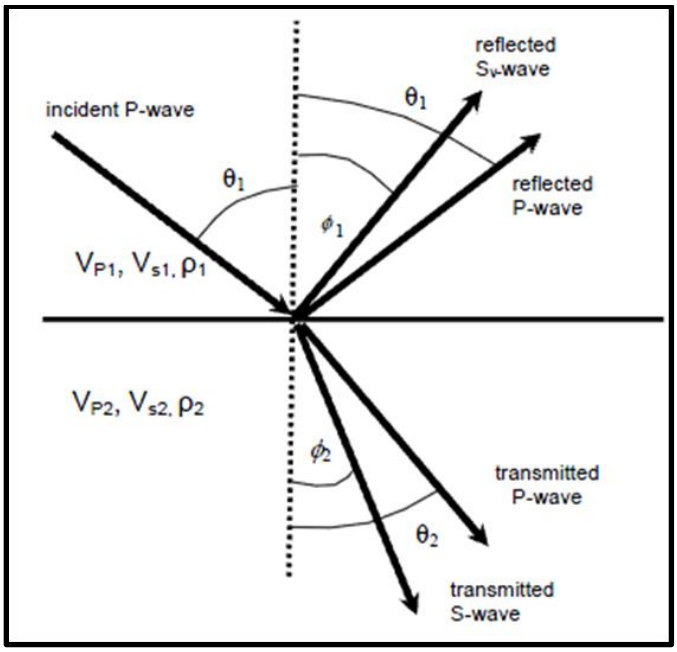

Figure 7 Incident P-wave, transmitted P and S- waves, and reflected P- and S-waves related to the angle of incidence and density.

$$\begin{bmatrix} R_{\mathrm{P}} \\ R_{\mathrm{S}} \\ T_{\mathrm{P}} \\ T_{\mathrm{S}} \end{bmatrix} = \begin{bmatrix} -\sin\theta_1 & -\cos\phi_1 & \sin\theta_2 & \cos\phi_2 \\ \cos\theta_1 & -\sin\phi_1 & \cos\theta_2 & -\sin\phi_2 \\ \sin 2\theta_1 & \frac{V_{\mathrm{P1}}}{V_{\mathrm{S1}}}\cos 2\phi_1 & \frac{\rho_2 V_{\mathrm{S2}}^2 V_{\mathrm{P1}}}{\rho_1 V_{\mathrm{S1}}^2 V_{\mathrm{P2}}}\cos 2\phi_1 & \frac{\rho_2 V_{\mathrm{S2}} V_{\mathrm{P1}}}{\rho_1 V_{\mathrm{S1}}^2}\cos 2\phi_2 \\ -\cos 2\phi_1 & \frac{V_{\mathrm{S1}}}{V_{\mathrm{P1}}}\sin 2\phi_1 & \frac{\rho_2 V_{P2}}{\rho_1 V_{P1}}\cos 2\phi_2 & \frac{\rho_2 V_{S2}}{\rho_1 V_{P1}}\sin 2\phi_2 \end{bmatrix}^{-1} \begin{bmatrix} \sin\theta_1 \\ \cos\theta_1 \\ \sin 2\theta_1 \\ \cos 2\phi_1 \end{bmatrix}$$

Table 1 Zoeppritz equations (Zoeppritz, 1919)

Rp: Reflected P-wave amplitude Rs: Reflected S-wave amplitude

Tp: Transmitted P-wave amplitude Ts: Transmitted S-wave amplitude

$$R(\theta) \cong R(0) + (G)sin^2\theta_I + F(tan^2\theta_I - sin^2\theta_I)$$

where R(0) is the normal incidence reflection coefficient, G is the AVO gradient and indicates the variation of reflection coefficients at given intermediate ($0 < \theta < 30$ degrees) AVO offset angles less than 30 degrees while F is referred for the variation of reflection coefficients at far offset near the critical angle.

$$R(0) = \frac{1}{2}\left(\frac{\Delta Vp}{Vp} + \frac{\Delta\rho}{\rho}\right)$$

$$G = \frac{1}{2}\frac{\Delta Vp}{Vp} - 2\frac{Vs^2}{Vp^2}\left(\frac{\Delta\rho}{\rho} + 2\frac{\Delta Vs}{Vs}\right)$$

$$F = \frac{1}{2}\frac{\Delta Vp}{Vp}$$

$$Vp = \tfrac{1}{2}(Vp_2 + Vp_1) \quad \Delta Vp = Vp_2 - Vp_1 \quad Vs = \tfrac{1}{2}(Vs_2 + Vs_1)$$

$$\Delta Vs = Vs_2 - Vs_1 \quad \rho = \tfrac{1}{2}(\rho_2 + \rho_1) \quad \Delta\rho = \rho_2 - \rho_1$$

Table 2 Shuey approximation (Shuey, 1985)

Since the third term has a small effect equals approximately zero for small AVO offset angles, the Shuey (1985) approximation simplifies these formulas for angles less than 30 degrees and demonstrates that if we know for a region of sediment in the subsurface (1) the average P-wave velocity, (2) the approximate bulk density (β), and (3) the incident angle of the P-wave (i), we can back-calculate an average S-wave velocity. Therefore, in theory, if we find regions where Vs is

anomalously low (i.e., 80-90% lower than expected values for typical marine sediments), we can infer either significant unexpected changes in regional lithology, or, alternatively, high pore pressure.

If the Shuey AVO approximation is simplified for intermediate offset angles less than 30 degrees by ignoring third term, the reflection coefficient for a given angle, R (θ) is calculated from 2 main terms which are the normal incident (zero offset) reflection coefficient, R (0) and gradient, G (Avseth, 2004).

$$R(\theta) = \mathrm{R}(0) \ + G * sin^2(\theta) \tag{10}$$

Therefore, for the given reflectors and angle obtained from a seismic reflection data, I solve this equation for gradient (G).

$$G = \frac{R(\theta) - R(0)}{sin^2(\theta)} \tag{11}$$

If gradient (G) is known, Vs (Vs_2) below the seafloor and can be back calculated from the Shuey approximation for gradient (G);

$$G = \frac{1}{2}\frac{\Delta \mathrm{Vp}}{\mathrm{Vp}} - 2\frac{\mathrm{Vs}^2}{\mathrm{Vp}^2}\left(\frac{\Delta \rho}{\rho^2} + 2\frac{\Delta \mathrm{Vs}}{\mathrm{Vs}}\right)$$

$$Vp = \frac{1}{2}(Vp_1 + Vp_2);\ Vs = \frac{1}{2}(Vs_1 + Vs_2);\ \rho = \frac{1}{2}(\rho_1 + \rho_2)$$

$$\Delta Vp = (Vp_2 - Vp_1);\ \Delta Vs = (Vs_2 - Vs_1);\ \Delta\rho = (\rho_2 - \rho_1)$$

(12)

Where Vp_1 and Vp_2 are estimated from P-wave velocities calculated from the multichannel (Common-Mid Point) CMP gathers and Dix equation.

I assume that the deep marine environments have pelagic clay sediment lithology, and the porosity (φ) profile is assumed to follow Hamilton's (1976) model. Then ρ_1 and ρ_2 are derived as bulk densities from Gassmann (1951) equations using the Hamilton (1976) porosity profile. Below is the empirical equation from Hamilton (1976) used to estimate the porosity change with depth in typical deep-water marine environments?

$$\varphi = 0.814 - 0.813 * depth(km) + 0.164 * (depth(km))^2 \text{ (Hamilton, 1976)}$$

(13)

The equation to calculate bulk density becomes

$$\rho_b = \varphi * \rho_f + (1 - \varphi) * \rho_s \text{ (Gassmann, 1951)}$$

(14)

Where ρ_b is bulk density (kg/m^3), and ρ_f and ρ_s equal 1032 kg/m^3 and 2580 kg/m^3 respectively as water and solid densities (kg/m^3).

Since S-waves cannot propagate in fluids (section 2.1), I know the S-wave velocity at seafloor (Vs_1) equals zero. Additionally, reflectors are normalized according to sea-floor reflector values at a given angle which I assume is 20 degrees, and thus the gradient (G) equals zero at seafloor.

$$Vs_1 = 0 \text{ (at seafloor)}$$

$$G = \frac{R(20) - \mathrm{R}(0)}{sin^2(20)} = 0 \quad (15)$$

Then I solve the gradient (G) equation for Vs_2 velocity value provides G equals zero. Once I obtain the Vs_2 velocity below the seafloor, I am able to calculate subjacent Vs velocities by taking the gradient (G) as the average change in absolute amplitude values of subjacent zones for a given reflection at 20 degrees.

2.3 Methodology for Estimating how Vp and Vs values vary with changing density, mineralogy, pore fluids, or pore pressure in marine sediments: Effective Medium Modelling

Once Vp and Vs values are known, I need to determine whether these values are consistent with normally pressured sediment, or instead, indicative of possible overpressure. An empirical way to do this is to simply examine Vp/Vs ratios (previously discussed). Alternatively, a physically more robust way to understand if and how Vp and Vs values are influenced by changing physical conditions involves using the first-principles effective medium modeling approach of Dvorkin et al. (1999) that uses Hertz-Mindlin (1949) and Gassmann (1951) equations to estimate bulk & shear

modulus of saturated clay-rich sediments. For this study, I make use of both the empirical and first-principles approach, but discuss the first-principles effective medium approach below.

For the effective medium approach, we need to assume a porosity/density profile for normally consolidated marine sediment, a mineralogy for the sediment grains, a pore fluid type, a grain contact number, a critical porosity at which compaction/lithification occurs, and a pore fluid pressure (see equations 16 below). It should be noted that porosity, and mineralogy represent the most important factors typically influencing Vp and Vs, in addition to them only high pore pressures have a significant impact (Hornbach and Manga, 2014). Grain contact number has only a second order effect on velocity for shallow marine sediments.

For the initial analysis, I assume normally pressured sediment, a constant grain contact number (n) of 6, and a critical porosity (φ_c) of 36%, consistent with experimental observations and previous effective medium models used in marine environments (e.g. Helgerud et al., 1999; Mavko, 2009).

To estimate porosity and bulk density, as I assumed in the previous section, I use the standard Hamilton (1976) model for porosity (φ) derived from pelagic-clay and Gassman (1951) equations that are typical of deepwater environments likely consistent with the Marmara Sea. Regional drilling mud-logs from the Marmara Sea indicate that the upper few hundred meters of our study site are mud-rich, with a sand rich layer located ~198 m below the seafloor (Marmara-1, Final well report). This change to sand represents the only likely significant variation in mineralogy at the study site, and only occurs at depths >200 mbsf. For this study, the solid phase of the lithology is assumed to consist of variations of clay and quartz (sand) constituents with water (and in some instances possible gas) filling the pores.

The Poisson's ratio (σ) of the solid mineral grains is defined based on bulk (K) and shear modulus (μ) in the solid phase. The effective shear (G_{hm}) and bulk (K_{hm}) modulus at the critical porosity (φ_C) are estimated with the average number of contacts (n) via Hertz-Mindlin (1949) contact theory.

$$\sigma = 0.5 * (K - \frac{2}{3} * G)/(K + \frac{1}{3} * G)$$

$$K_{hm} = \left(n^2 * (1 - \varphi_C)^2 * \frac{G^2}{18 * \pi^2 * (1 - \sigma)^2} * P\right)^{1/3}$$

$$G_{hm} = \frac{5 - 4 * \sigma}{5 * (2 - \sigma)} * \left(3 * n^2 * (1 - \varphi_C)^2 * G^2 * \frac{P}{2 * \pi^2 * (1 - \sigma)^2}\right)^{1/3}$$

(16)

where P (MPa) is the effective pressure, the difference between lithostatic and pore fluid pressures that affect sediments from the seafloor to the target depth.

Both the effective (Khm, Ghm) and the pure solid (K, G) elastic modulus indicates two end points or borders of elastic modulus-porosity profile. The effective elastic modulus represents the dry rock elastic modulus by assuming a rock in sphere pack subject to confining pressure (P) at critical porosity whereas the pure solid elastic modulus represents the dry rock elastic modulus by assuming a rock in a solid phase at zero porosity (e.g. Dvorkin, J., & Nur, A., 2002)

Effective bulk (Kdry) and shear (Gdry) modulus of the dry frame are the mixture of the effective and solid phase elastic modulus. It is derived from effective shear (Ghm) and bulk (Khm) modulus at critical porosity (φ_C).

$$K_{dry} = \left(\frac{\frac{(1-\varphi)}{(1-\varphi_C)}}{K_{hm+}\left(\frac{4}{3}\right) * G_{hm}} + \frac{\frac{(\varphi-\varphi_C)}{(1-\varphi_C)}}{\left(\frac{4}{3}\right) * G_{hm}} \right)^{-1} - \left(\frac{4}{3}\right) * G_{hm}$$

$$G_{dry} = \left(\frac{\frac{(1-\varphi)}{(1-\varphi_C)}}{G_{hm} + \left(\frac{G_{hm}}{6}\right) * \left(\frac{9 * K_{hm} + 8 * G_{hm}}{K_{hm} + 2 * G_{hm}}\right)} + \frac{\frac{(\varphi-\varphi_C)}{(1-\varphi_C)}}{\left(\frac{G_{hm}}{6}\right) * \left(\frac{9 * K_{hm} + 8 * G_{hm}}{K_{hm} + 2 * G_{hm}}\right)} \right)^{-1} - \left(\frac{G_{hm}}{6}\right) * \left(\frac{9 * K_{hm} + 8 * G_{hm}}{K_{hm} + 2 * G_{hm}}\right)$$

(17)

Then, the saturated bulk and shear modulus are calculated with a bulk modulus of pore fluid (Kf) based on Gassmann's equations where the saturated shear (Gsat) modulus should equal the shear modulus (Gdry) of the dry frame (Gassmann, 1951).

$$K_{sat} = \frac{K * \left(\varphi * K_{dry} - \frac{(1-\varphi) * K_f * K_{dry}}{K} + K_f\right)}{(1-\varphi) * K_f + \varphi * K - \frac{K_f * K_{dry}}{K}}$$

$$G_{sat} = G_{dry}$$

(18)

The P-wave and S-wave velocity profile is constructed with bulk and shear modulus and the density of saturated sediments.

The calculation of seismic velocities by using this effective medium methodology provides the ability to produce forward model for the expected *in situ* Vp and Vs values in a typical deep-sea

sediment lithology with no overpressure zones. I will compare observed versus model-predicted values, will calculate if and where elevated fluid pressure and gas concentration may exist.

2.3.1 Determining key factors that control Vp, Vs, Vp/Vs and AVO response

As noted above, the main factors affecting seismic velocities are

1.) Porosity

2.) Mineralogy

3.) Gas (Vp)

4.) Pore-fluid pressure (Vs and Vp)

I use these factors as a starting point for predicting expected Vp, Vs, Vp/Vs and AVO responses in marine sediments, and to determine how changes in porosity, lithology, pressure, and gas concentration impact seismic velocities and their AVO responses in typical marine (not overpressured and not gas-rich) sediments.

Once I complete this preliminary analysis, I then compare these values, especially Vp/Vs ratios and AVO responses, predicted with Hamilton-like sediments, with AVO responses for data collected in the Marmara Sea, and from this, I draw initial conclusions about the sediment character and stress state for Marmara Sea sediments. I then use these results to estimate Vs, and, from this draw conclusions about where (1) elevated gas concentrations and (2) elevated pore pressure values may exist.

As already noted, since there is no well data available for our study area, Vp, Vs, Vp/Vs ratio and AVO responses are calculated assuming mud-rich sediments observed in typical deepwater environments that are likely consistent with the Marmara Sea based on Hamilton's models and

using the effective medium model approach. P-wave and S- wave velocities are first calculated using the effective medium approach. I then compare the estimates Vp of and Vs with those observed in the Marmara Sea.

2.3.1a Sensitivity analysis #1: Influence of changes in porosity on Vp, Vs, Vp/Vs, and AVO response.

In the first scenario of our model, I assume 100% clay-rich sediment to 400 m depth below the seafloor with porosity derived from a pelagic-clay lithology (Hamilton, 1976). For the calculated Vp and Vs response, I assume a seismic imaging resolution of 10 m, and calculate the AVO response at 10 m intervals with depth by assuming pure clay lithology (Clay 100%). In addition, I apply an anomalous 5% decrease/increase in porosity, and compare the results to the Hamilton model estimates at ~190 m depth to determine what effect this has on Vp/Vs ratios. Again, for this example, no lithology changes, and no overpressure or gas exists in the pore space. By varying porosity in the pure clay lithology, I assess how sediment porosity can influence the velocity, Vp/Vs and AVO response at the depths of interest for our study area. P-wave and S- wave velocities are first calculated using the effective medium approach, and the AVO response is then calculated via the Shuey AVO approximation formula. Results (Table 5 and Table 6), show that a 5% decrease/increase in porosity results in 1% change in Vp and 10% change in Vs, with the Vp/Vs ratio changing by 10%. From an empirical Vp/Vs approach, the resulting Vp/Vs values are consistent with typical marine sediments (Vp/Vs), with values remaining between 3 and 8—consistent with what is typically observed in marine sediments (Prasad, 2002). This implies that an anomalous 5% change in porosity will not likely result in a detectable or spurious zone of Vp/Vs that might be associated with gas or overpressure development.

Elastic Parameters Used in This Model	
Parameter	Value
Number of contacts per grain (n)	6
Critical porosity (φ, %)	36
Pore fluid density (kg/m)	1032

Table 3 Elastic Parameters Used in Scenario 1

Constituents	Percentage (%)	Density (kg/m$^{3)}$	K (Pa)	G (Pa)
CLAY	100	2580	21*10^9	6.85*10^9

Table 4 Ratio of constituents with their density, bulk (K) and shear (G) modulus for the target sediment layer lithology in solid phase in Scenario 1

Depth(m)	Vp(m/s)	Vs(m/s)	Density(kg/m3)	Fractional Porosity	Poisson's Ratio	Vp/Vs
10	1512	104	1332	0.80	0.498	14.5
50	1518	151	1382	0.77	0.495	10.1
100	1527	188	1443	0.73	0.492	8.1
150	1539	220	1503	0.69	0.490	7.0
190	1550	244	1550	0.67	0.487	6.4
190	1569	269	1627	0.62	0.485	5.8
200	1574	276	1639	0.61	0.484	5.7
200	1554	250	1562	0.66	0.487	6.2
250	1572	279	1619	0.62	0.484	5.6
300	1592	308	1675	0.58	0.481	5.2

Table 5 Derived velocity profile and elastic parameters for Scenario 1. 100% clay (mud-rich) sediment to 400 m depth is shown in grey, assuming a 10-m-thick sediment layer of the same lithology (shown in green) has 5% less porosity than Hamilton porosity profile. The analysis indicates that Vp/Vs ratios are typically less than 8 for all values at depths greater than ~100

mbsf—the direct result of lower sediment porosity with depth. These results are consistent with what we would expect for standard marine sediments.

Depth(m)	Vp(m/s)	Vs(m/s)	Density(kg/m3)	Fractional Porosity	Poisson's Ratio	Vp/Vs
10	1512	104	1332	0.80	0.498	14.5
50	1518	151	1382	0.77	0.495	10.1
100	1527	188	1443	0.73	0.492	8.1
150	1539	220	1503	0.69	0.490	7.0
190	1550	244	1550	0.67	0.487	6.4
190	1537	219	1472	0.72	0.490	7.0
200	1539	224	1484	0.71	0.489	6.9
200	1554	250	1562	0.66	0.487	6.2
250	1572	279	1619	0.62	0.484	5.6
300	1592	308	1675	0.58	0.481	5.2

Table 6 100% clay (mud-rich) sediments (grey fill) to 400 m depth, assuming a 10-m-thick sediment layer of the same lithology (shown in green) has 5% higher porosity than Hamilton porosity profile. Even though Vp/Vs ratio increased in the target depths (190-200 m) these values are still less than 8, which suggests a potential high pore pressure indicator (Prasad, 2002).

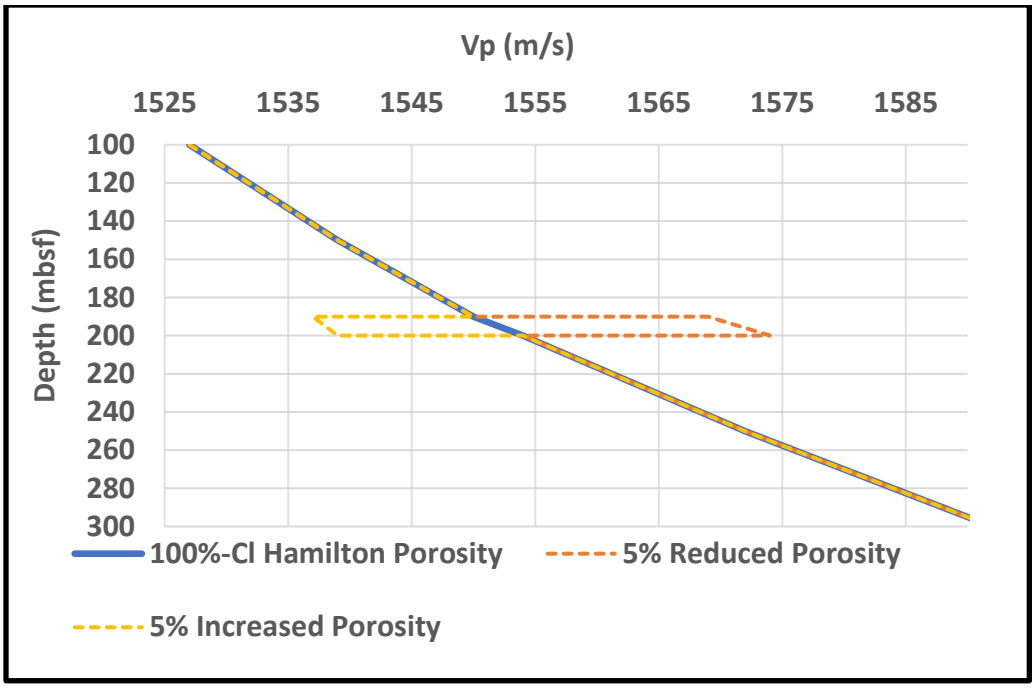

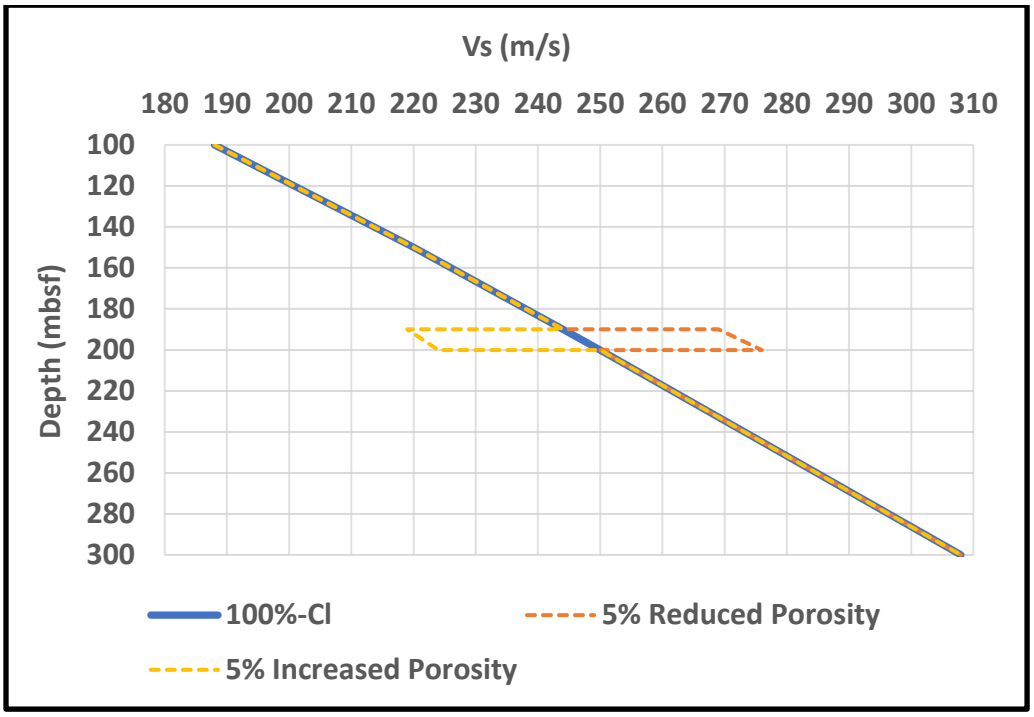

Figure 8 P-wave and S wave velocity profiles for the target sediment layer has 5% less/bigger porosity than Hamilton porosity profile Cl:Clay, mbsf: meters below sea floor.

Here are key results from this thought experiment: As expected, I observe a general decline in porosity with depth and an increase in seismic velocities due to increasing shear and bulk modulus with depth. Even for significant porosity reduction in target sediment layer of 5%, S-wave velocity is only increased by 10%. The effect on Vp is even smaller, with an increase of about 1%. Conversely, the increase in the porosity profile leads to a decrease in both the P-wave and S-wave velocities (~1% and 10% respectively) (Figures 7, and 8). Despite of the 10% change in Vp/Vs ratio, these values are not high (over 8, Figure 9) enough to be considered as overpressure or not low enough to be considered as gas concentration (lower 3) (Prasad, 2002).

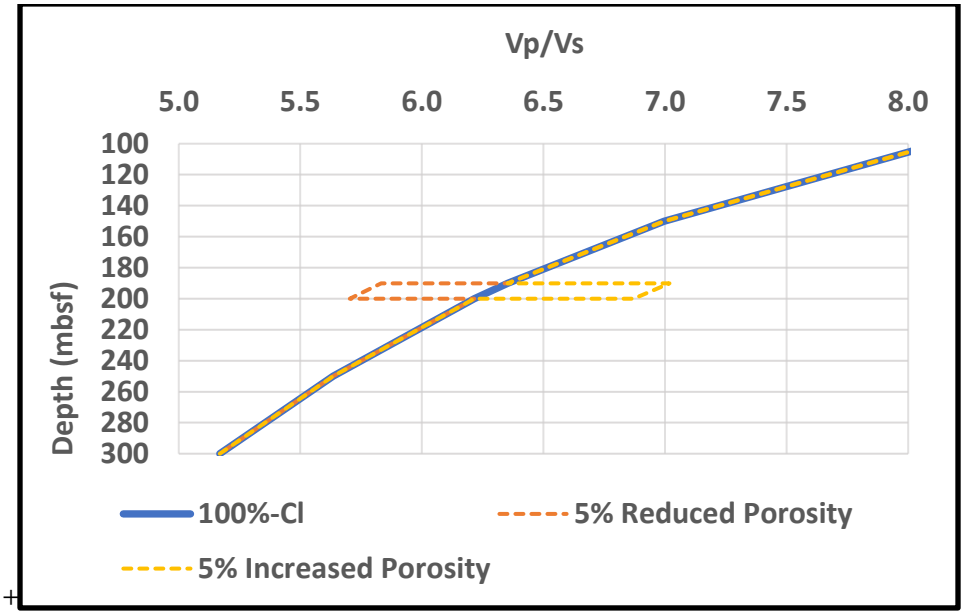

Figure 9 Vp/Vs for the target sediment layer with 5% less/more porosity than Hamilton porosity profile Cl:Clay, mbsf: meters below sea floor. Note that, increased porosity profile causes the increasing of Vp/Vs ratio till 7 but not >8 as suggested for typical high pore pressure zones in marine sediment (Prasad, 2002)

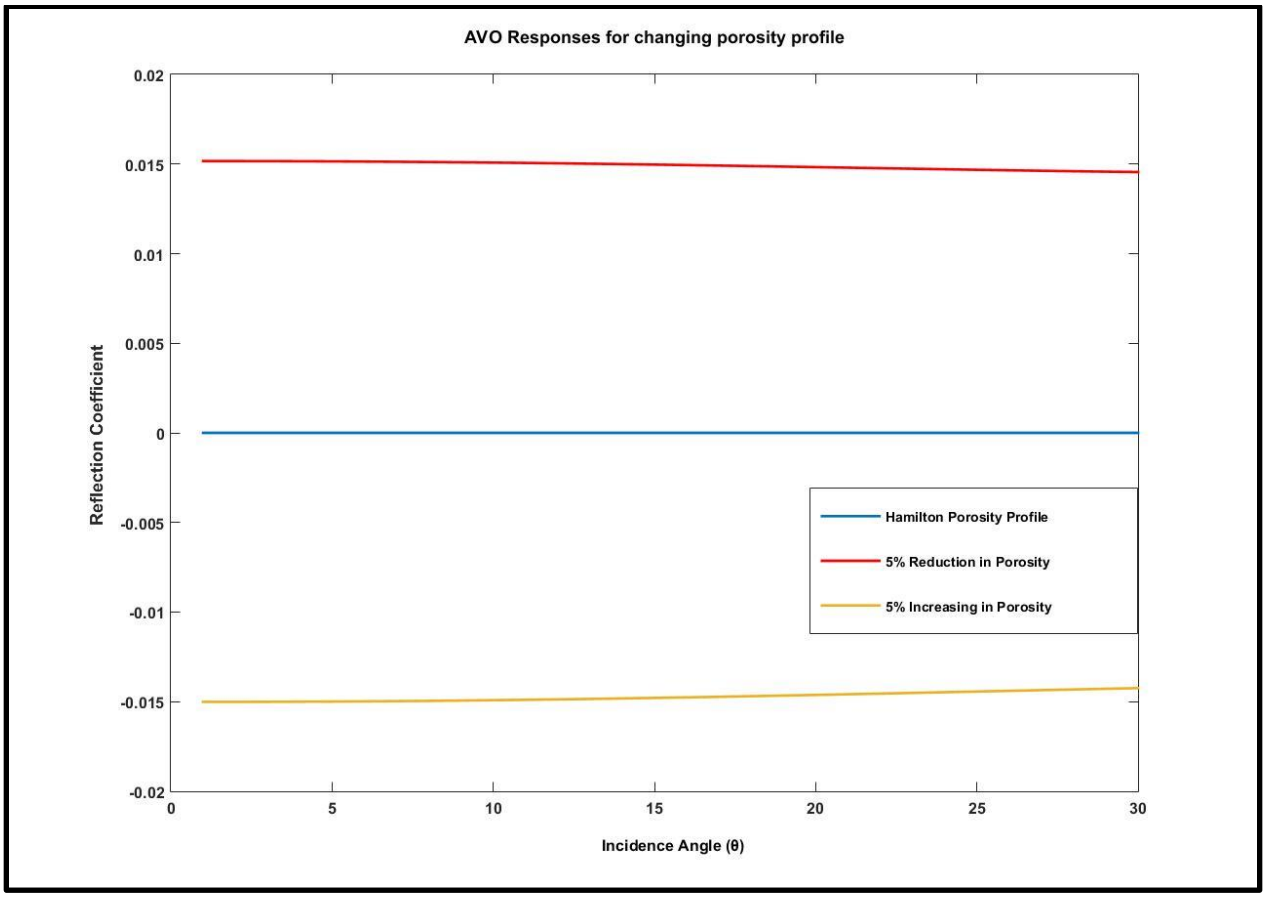

Figure 10 AVO responses due to changing porosity (+/- 5%) in target zone with pure clay lithology (100%-Cl 0%-Qtz). Though the amplitude change is significant at zero offset, note that the AVO response is relatively insensitive to porosity (the amplitude change with offset for each case is quite small). Since we will use AVO response to estimate Vs velocity, this results hints at the difficult in estimating Vs: only the most significant AVO responses (and changes in Vs) will be are clearly detectable.

.

As in Vp/Vs ratios, the AVO responses as they relate to porosity changes are not significant. They are not expected to produce detectable Vs anomalies that would be identified as high pore pressure zones.

2.3.1b Sensitivity analysis #2: Influence of changing mineralogy on Vp, Vs, Vp/Vs and AVO response.

In the second modeling scenario, I assume 100% clay-rich sediment to 400 m depth below the seafloor with porosity characteristics derived from pelagic-clay lithology (Hamilton, 1976). In order to estimate Vp, Vs, Vp/Vs, and the AVO response, I calculate values at 10 m intervals of depth by assuming pure clay initially, then vary the mineralogy from 100% clay to 100% sand (using 25% step change intervals) at 190 m depth to determine how mineralogy might change these values. Again, for this example I assume no variations in the porosity profile, and that no overpressure or gas exists in pore space. By varying the sand versus clay content by 25% from pure clay to pure sand, we assess how sediment mineralogy effects the velocities, Vp/Vs ratio, and AVO response at these depths.

Depth(m)	Vp(m/s)	Vs(m/s)	Density(kg/m3)	Fractional Porosity	Poisson's Ratio	Vp/Vs
10	1512	104	1332	0.80	0.498	14.5
50	1518	151	1382	0.77	0.495	10.1
100	1527	188	1443	0.73	0.492	8.1
150	1539	220	1503	0.69	0.490	7.0
189	1550	243	1549	0.67	0.487	6.4
190	1636	428	1573	0.67	0.463	3.8
200	1643	438	1585	0.66	0.462	3.8
201	1554	251	1563	0.66	0.487	6.2
210	1557	256	1573	0.65	0.486	6.1
250	1572	279	1619	0.62	0.484	5.6
300	1592	308	1675	0.58	0.481	5.2

Table 7 Derived velocity profile and elastic parameters for Scenario 2. 100% clay mud-rich sediment to 400 m depth is grey color filled, except between 190 and 200 m (green fill), where it is assumed a pure sand layer has pure sand mineralogy. Note that, the Vp/Vs ratios reduce significantly (more than Scenario1-reduction 5% porosity) in target layer.

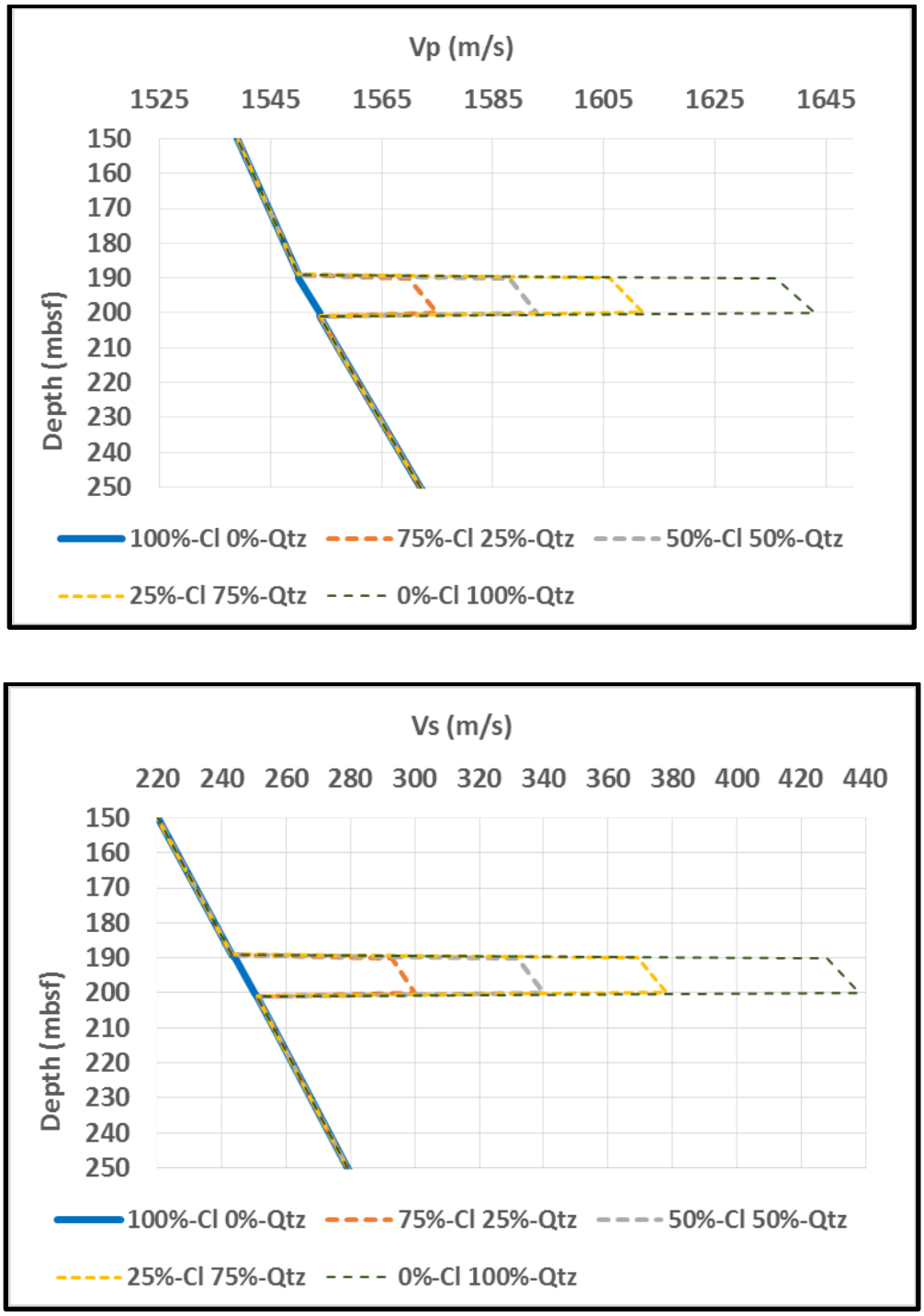

Figure 11 P-wave and S-wave velocity profiles for the target sediment layer with changing lithology from 100% clay to 100% Quartz Cl: Clay, Qtz: Quartz, mbsf: meters below sea floor.

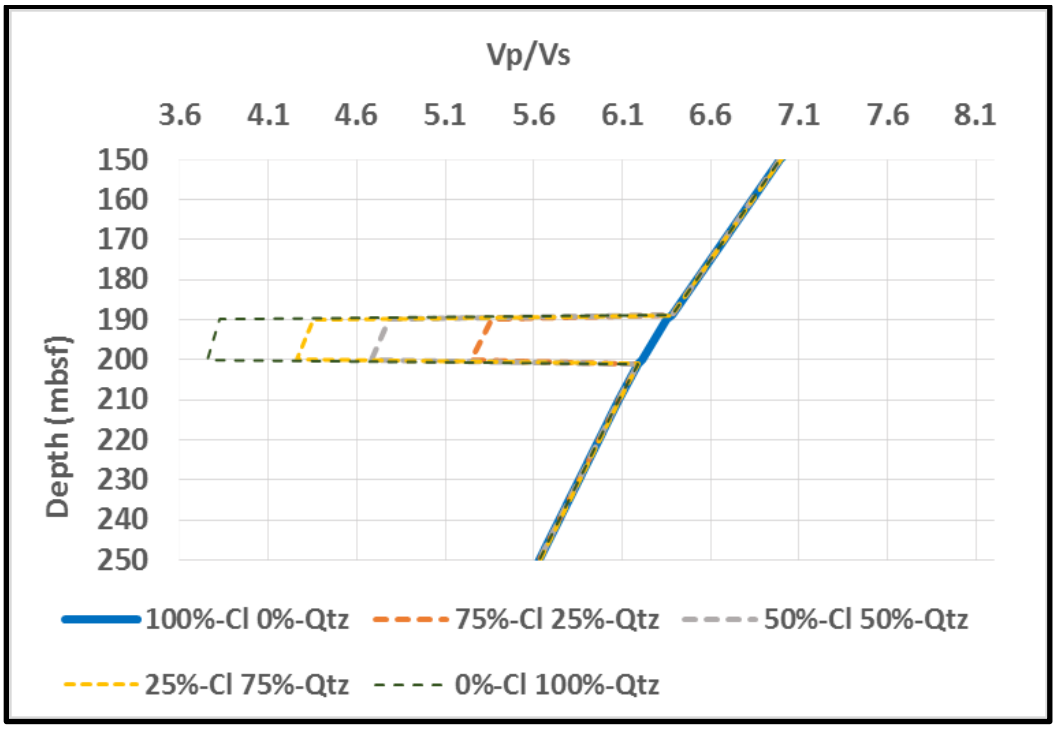

Figure 12 Vp/Vs values for the target sediment layer with changing lithology from 100% clay to 100% sand (quartz) Cl:Clay, Qtz: Quartz, mbsf: meters below sea floor.

As the target sediment lithology from pure clay to pure sand changes at 190-200 mbsf both P and S wave velocities increase, but in different percentages. For instance, as an extreme variation, Vs increases by 75% and, Vp increases by 5.5% if the target layer has pure sand lithology. This demonstrates the higher sensitivity of Vs relatively to Vp associated with lithology changes from pure clay to pure sand (Figure 11).

Hence, the Vp/Vs ratio is 40% lower and reaches a 3.8 ratio in the target sediment layer if it has a pure sand lithology, which is also an extreme change. However, this ratio does not reach Vp/Vs less than 3 that are suggestive as a free gas indicator for unconsolidated sediments (Lee, 2003). It should be noted that if we see an increase of sand with depth (as anticipated in the sea of

Marmara) and no other significant changes occur, we would expect a reduction in Vp/Vs with depth at the site—the opposite of what will occur if pore pressures increase, but it will not be distinguishable than gas.

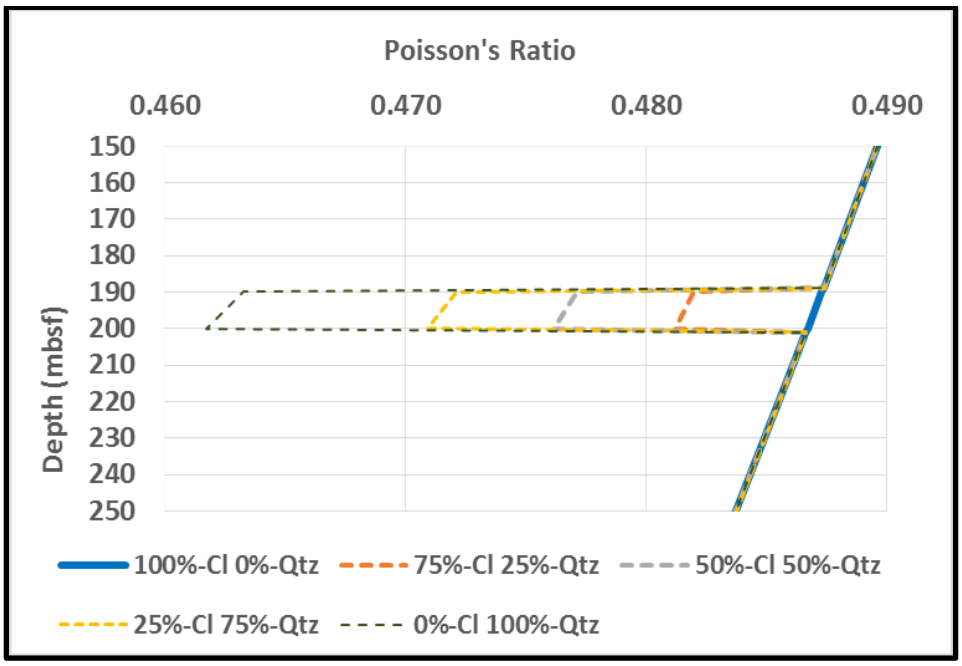

Figure 13 Poisson's Ratio for the target sediment layer (190 to 200 m) with changing lithology from 100% clay to 100% quartz

By changing the mineralogy from pure clay to pure sand, AVO responses are observed with generally negative slope changes in amplitude at all depths (Figure 14). With a lithology that has less than 50% sand, the AVO responses are relatively smaller. Bigger amplitude anomalies from zero offset through far offset are observed for the lithologies with over 50% sand since sand becomes the dominant in sediment lithology. Though the amplitude change is significant at zero

offset, note that the AVO response is relatively insensitive to porosity (the amplitude change with offset for each case is quite small). Since we will use AVO response to estimate Vs velocity, this results hints at the difficulty in estimating Vs: only the most significant AVO responses (and changes Vs) will be clearly detectable.

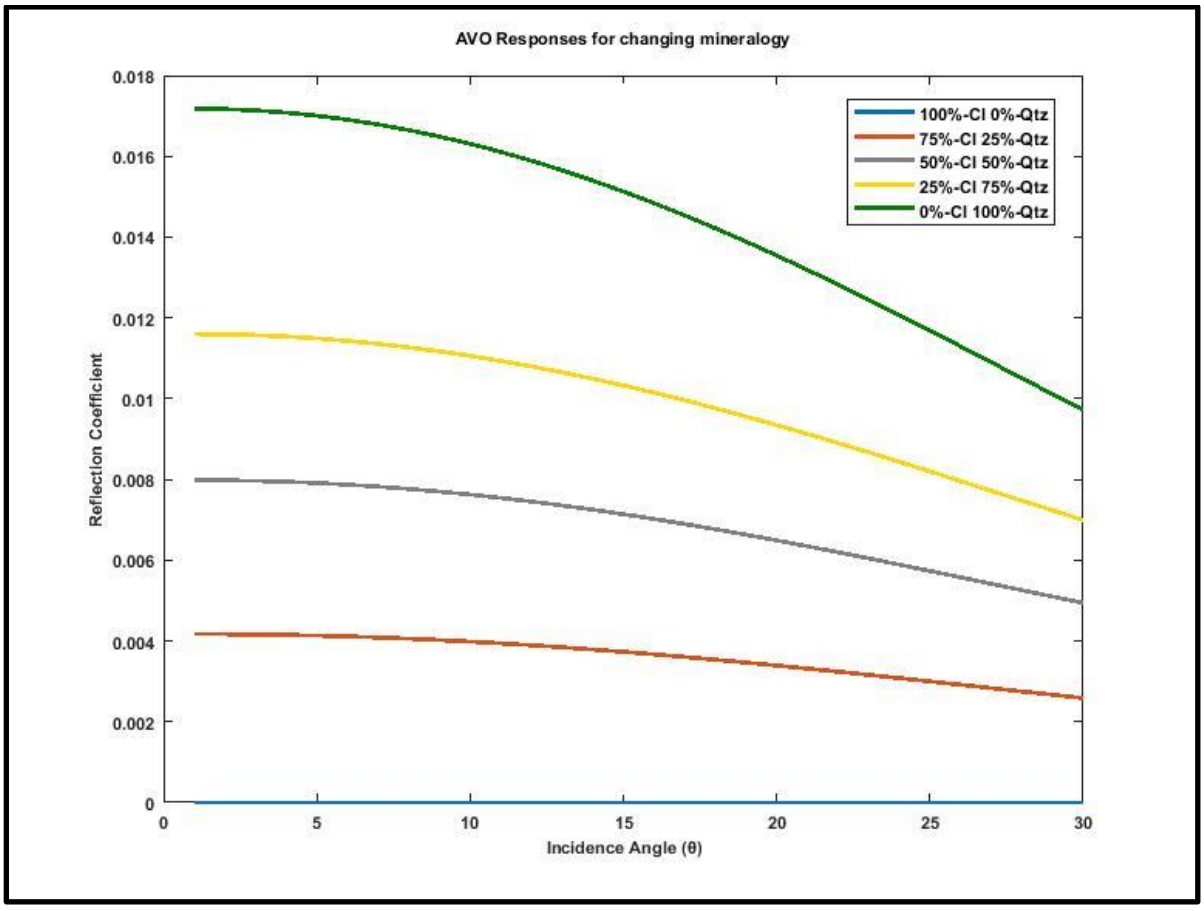

Figure 14 AVO responses due to changing lithology from pure clay to pure sand (Clay 100%- Clay 0%). Note that the relative change in amplitude with offset is small, but the effect appears greater than what I observe with a 5% porosity change (although these are extreme changes in minerology).

2.3.1c Sensitivity Analysis #3: Influence of elevated pressure on Vp, Vs, Vp/Vs, and AVO

To assess the role of pore pressure on Vp and Vs, in the third scenario I assume 100% clay sediment to 400 m depth below the seafloor with porosity characteristics derived from pelagic-clay lithology (Hamilton, 1976). The target pure clay sediment layer at 190 m depth has a 10-m thickness and also has high pore pressure that changes from hydrostatic to 90% of the lithostatic value, or a pore pressure ratio (λ^*) of 0.9.

Using the Hamilton model with a high pore pressure zone, we derive the P-wave and S- wave velocities using the effective medium model and AVO response is calculated by the Shuey AVO approximation.

Depth(m)	Vp(m/s)	Vs(m/s)	Density(kg/m3)	Fractional Porosity	Poisson's Ratio	Vp/Vs
10	1512	104	1332	0.80	0.498	14.5
50	1518	151	1382	0.77	0.495	10.1
100	1527	188	1443	0.73	0.492	8.1
150	1539	220	1503	0.69	0.490	7.0
190	1550	244	1549	0.67	0.487	6.4
190	1530	167	1550	0.67	0.494	9.2
200	1533	171	1562	0.66	0.494	9.0
200	1554	250	1563	0.66	0.487	6.2
250	1572	279	1619	0.62	0.484	5.6
300	1592	308	1675	0.58	0.481	5.2

Table 8 Derived velocity profile and elastic parameters for Scenario 3. 100% clay mud-rich sediment to 400 m depth is in grey, assuming a sediment layer is in same lithology has 10 m thickness from 190 to 200 m with high pore pressure λ^*=0.9 ratio at 190 m depth is highlighted in green color. This profile shows that Vp/Vs ratio increases to a value beyond 8 in the zone of interest. These values are consistent with overpressure Vp/Vs values predicted by Prasad (2002).

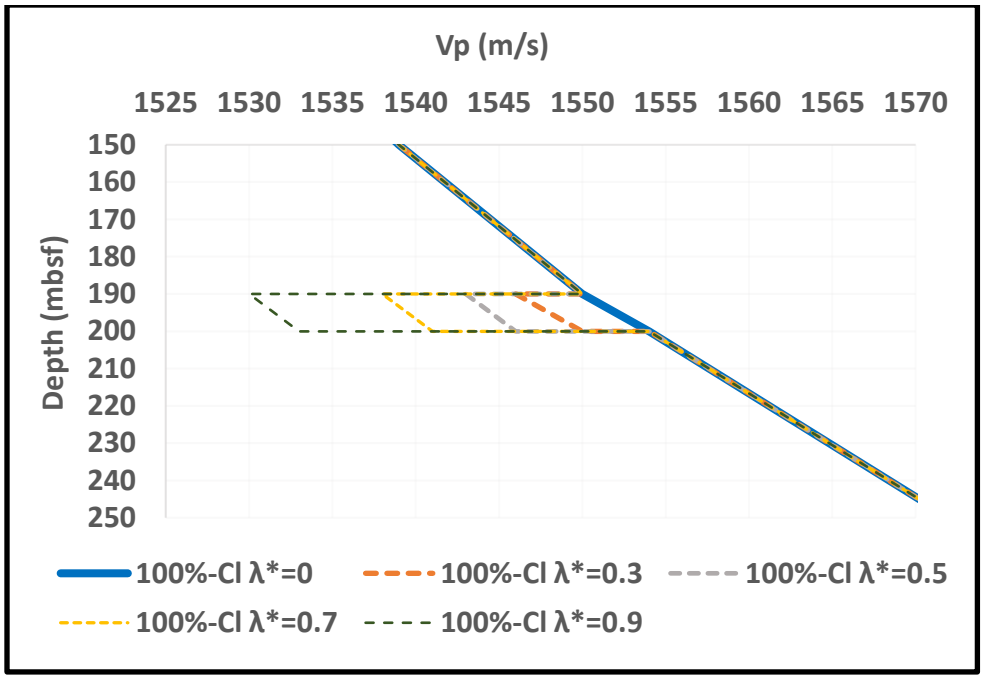

Figure 15 P-wave velocity profile for target 100% clay lithology has changing high pore pressure from 90% to 0%.

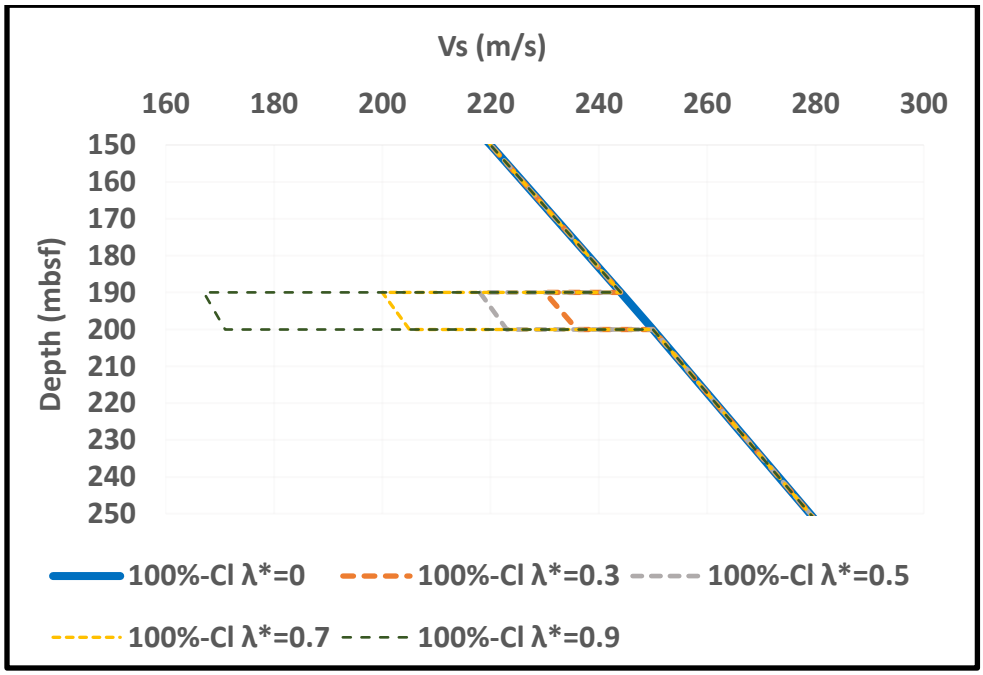

Figure 16 S-wave velocity profile for the target 100% clay lithology has changing high pore pressure from 90% to 0%.

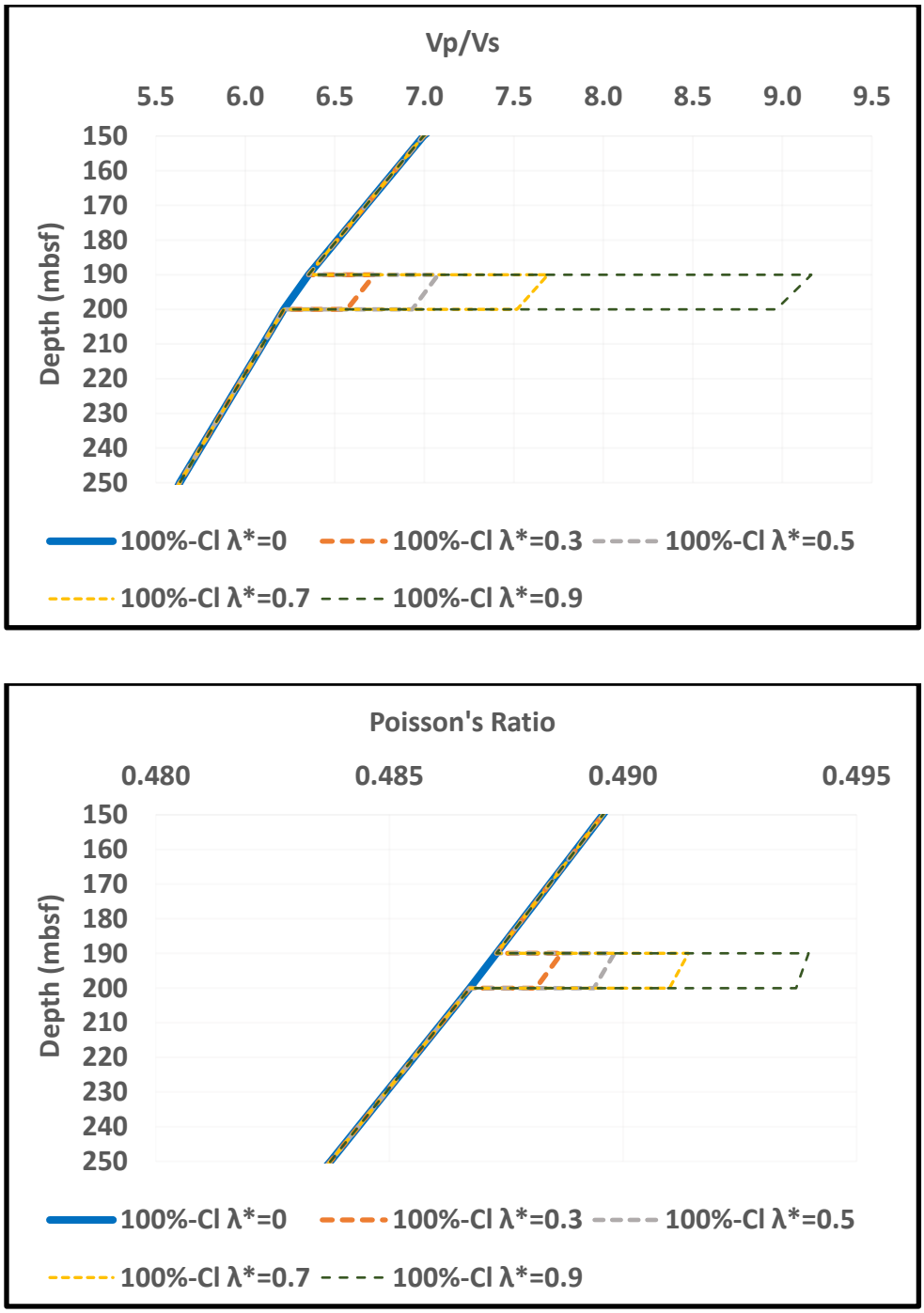

Figure 17 Vp/Vs and Poisson's Ratio profiles for target 100% clay lithology has changing high pore pressure from 90% to 0%. These figures demonstrate the non-linear effect pore pressure has on velocity: significant pore pressure ratios (>0.7) are necessary for significant (detectable) changes in Vp/Vs and Poisson's ratio to occur.

In this scenario, a decreasing gradient is observed for both P-wave and S-wave velocity profiles at different ratios as pore pressure increases in the zone of overpressure. Vp decreases about 1.5%, whereas Vs decreases about 32.5% with an increase in the Vp/Vs ratios (Figures 15,16, and 17). This demonstrates how Vs is more sensitive to pore pressure change than Vp (Figure 17).

Most notably, the Vp/Vs ratio equals 9.2 at 190 m depth for λ^* of 0.9, this value clearly exceeds typical values of 3 to 8, indicating strong evidence for elevated fluid pressure and a more liquefied layer located at this depth (Figure 17).

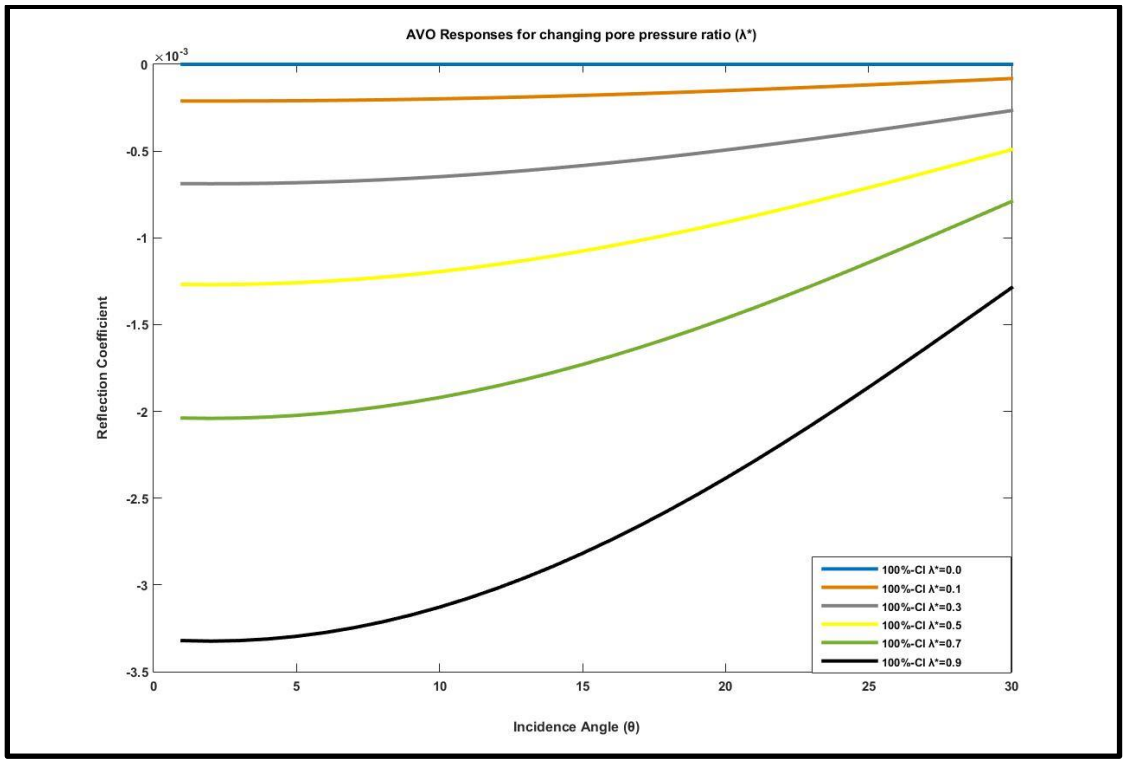

Figure 18 AVO response for changing pore pressure for 100% clay lithology with pore pressure ratio varying from 0 to 0.9. At 190 to 200 mbsf, velocities are significantly reduced as pore pressure approaches lithostatic values. This effect is also seen as a non-linear AVO response. Note that the AVO response is not only strong at zero offset but has a stronger far offset response when the pore pressure ratio is 0.9, with long offset (20 degree) amplitude reduced by 32%. This is 11% larger than what we observe for mineralogy changes and 29% compared to porosity changes at this angle.

In addition to high Vp/Vs ratios associated with near lithostatic pressures, a greater decrease in amplitudes at far-offsets (about 66% decreasing for $\lambda^*=0.9$) is another useful indicator I can use in this study to detect high pore pressure zones in the Marmara Sea region.

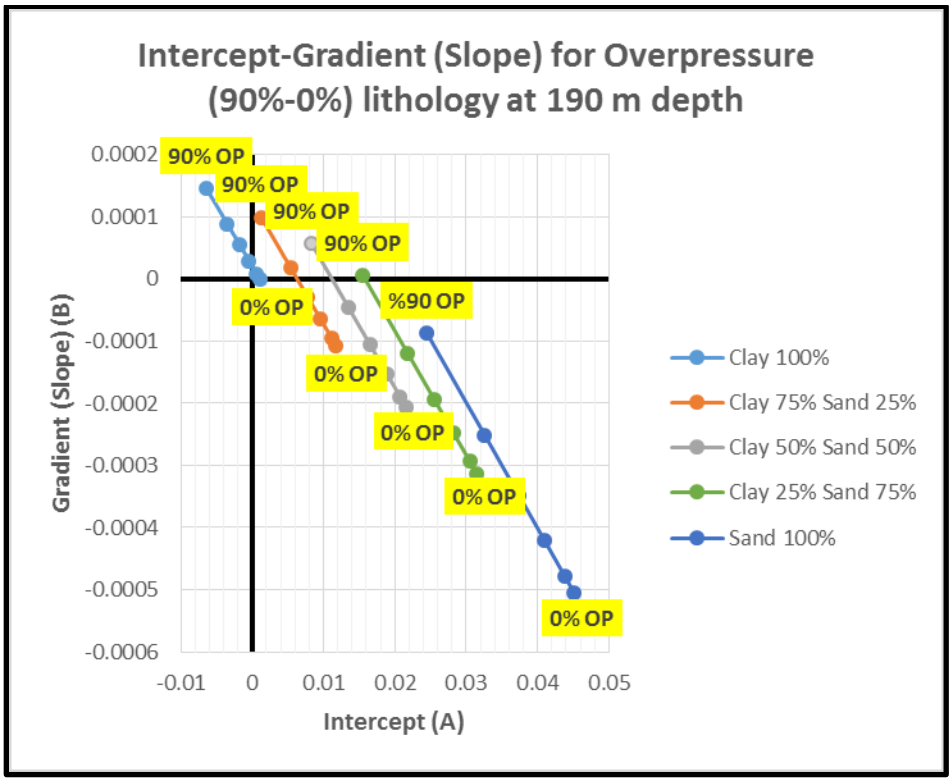

Figure 19 Intercept-Gradient (Slope) for Overpressure (90%-0%) in lithology (100% clay-0% clay) at 190 m depth. Note that for high pore pressure, the slope (gradient) of the AVO response is much more severe for pure clay lithology, and is always negative, implying a very significant decay in the amplitude effect with offset where high pore pressure exists.

2.3.1d Sensitivity analysis #4: Influence of Gas in Pore Space on Vp, Vs, Vp/Vs, and AVO

In the final scenario, I analyze the role of gas by assuming 100% clay mud-rich sediment to 400 m depth below the seafloor with porosity characteristics derived from Hamilton (1976). The target pure clay sediment layer has a 10-m thickness at 190 m depth and has gas that changes between 10% and 0% in the pore space.

Since this scenario assumes that gas fills 10% to 0% of the pore space in the target layer, where Sh is the concentration of gas in pore space, Kw is the bulk modulus of water, the bulk modulus of pore fluid (Kf) is calculated with this gas in the pore space.

$$S_{h=} ratio\ of\ gas/\varphi \tag{19}$$

$$K_f = \left(\frac{S_h}{K_h} + (1 - S_h)/K_w\right)^{-1} \tag{20}$$

For this, I assume the gas is patchy and not part of a large, interconnected gas column, and therefore, imparts no significant overpressure in the system. P- and S- wave velocities are derived using the effective medium approach and AVO response for the target layer is calculated via the Shuey AVO approximation.

Depth(m)	Vp(m/s)	Vs(m/s)	Density(kg/m3)	Fractional Porosity	Poisson's Ratio	Vp/Vs
10	1512	104	1332	0.80	0.498	14.5
50	1518	151	1382	0.77	0.495	10.1
100	1527	188	1443	0.73	0.492	8.1
150	1539	220	1503	0.69	0.490	7.0
190	1550	244	1549	0.67	0.487	6.4
190	955	251	1496	0.67	0.463	3.8
200	959	257	1508	0.66	0.461	3.7
200	1554	250	1563	0.66	0.487	6.2
250	1572	279	1619	0.62	0.484	5.6
300	1592	308	1675	0.58	0.481	5.2

Table 9 Derived velocity profile and elastic parameters for Scenario 4. 100% clay mud-rich sediment to 300 m depth is in grey color, assuming a sediment layer is in same lithology has 10 m thickness 10% gas filled (indicates an extreme value) in pore space at 190 m depth in green color. Since S-wave velocities are insensitive for gas concentrations in pore space, this profile shows that Vp/Vs ratio decreases significantly in the zone of interest such as mentioned in previous research (Lee, 2002) and shows the range of Vp/Vs ratio values I should expect in the presence of possible gas concentrations in the Marmara Sea region.

In the last scenario, a lower velocity is observed for only the P-wave velocity. By assuming as an extreme gas concentration such as 10% gas in pore space, P- wave velocity dramatically decreases by about 40%, but no alteration is observed in the S-wave profile (only about 1% increasing due to density change, which might be ignored): Vs continues to increase in its normal gradient with increasing depth. (Figure 20). Depending on the decrease in P-wave velocities versus non- affected S-waves, Vp/Vs ratio also drops significantly approaching 3.

This observation is consistent with the results from previous studies and shows that P-wave velocities and Vp/Vs ratios are useful indicators of possible gas concentrations.

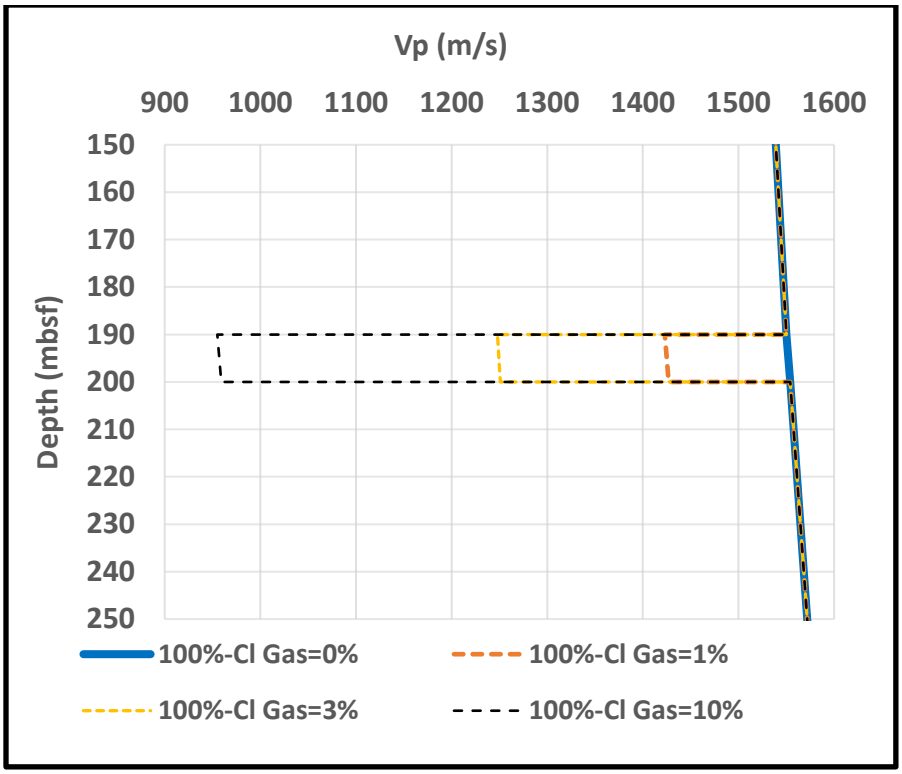

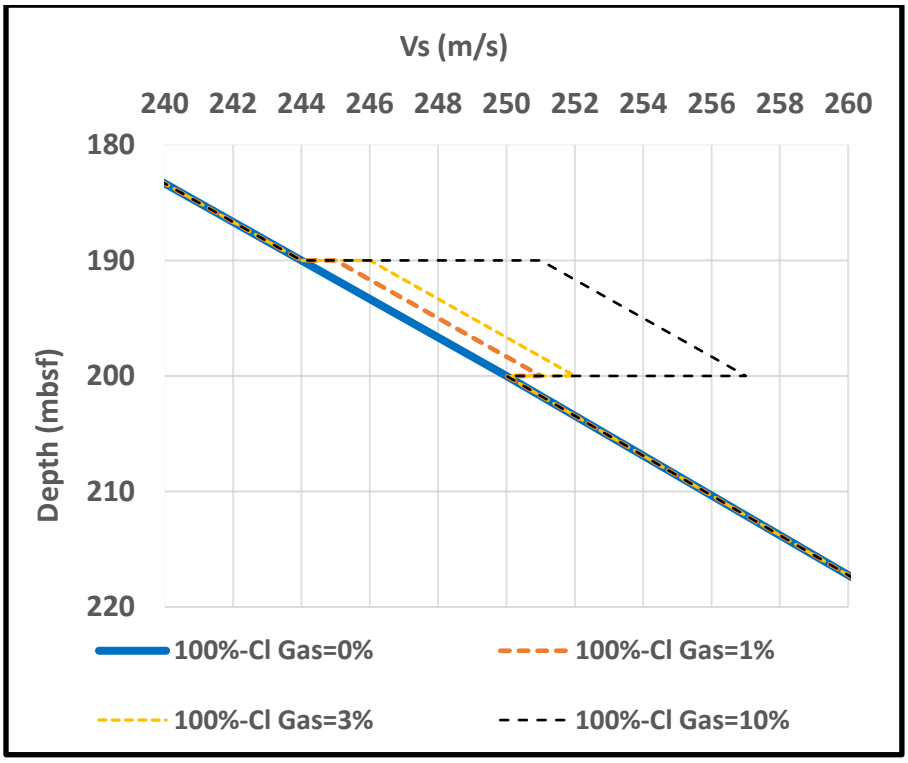

Figure 20 P-wave and S-wave gradients due to target 100% clay lithology has different amount of gas between 10% and 0% in pore space.

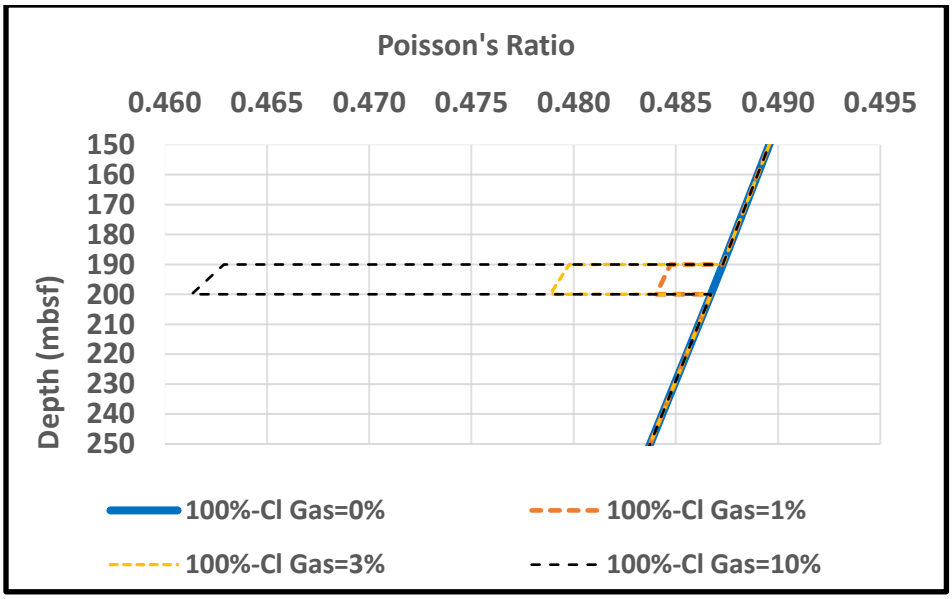

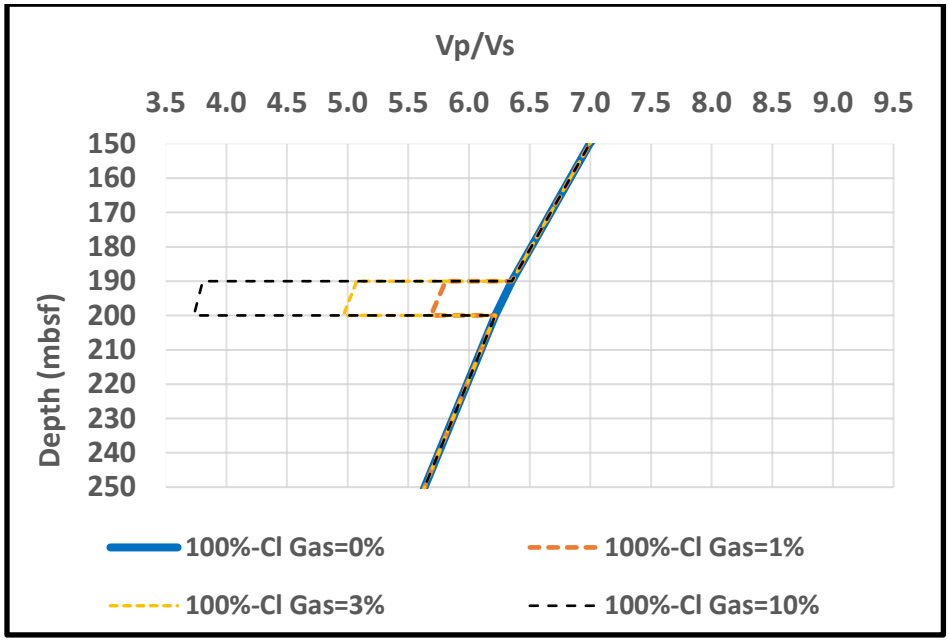

Figure 21 Poisson's Ratio and Vp/Vs gradients due to target 100% clay lithology has different amount of gas between 10% and 0% in pore space. Both of these ratios drop significantly through the increasing amount of gas concentration in target layer. In case of 10% gas concentration, Vp/Vs ratio drops to 3.8 and indicates high gas concentration, this value is consistent with the Vp/Vs ratio for gas concentrations in unconsolidated sediments has greater porosity than 40% (Lee, 2002).

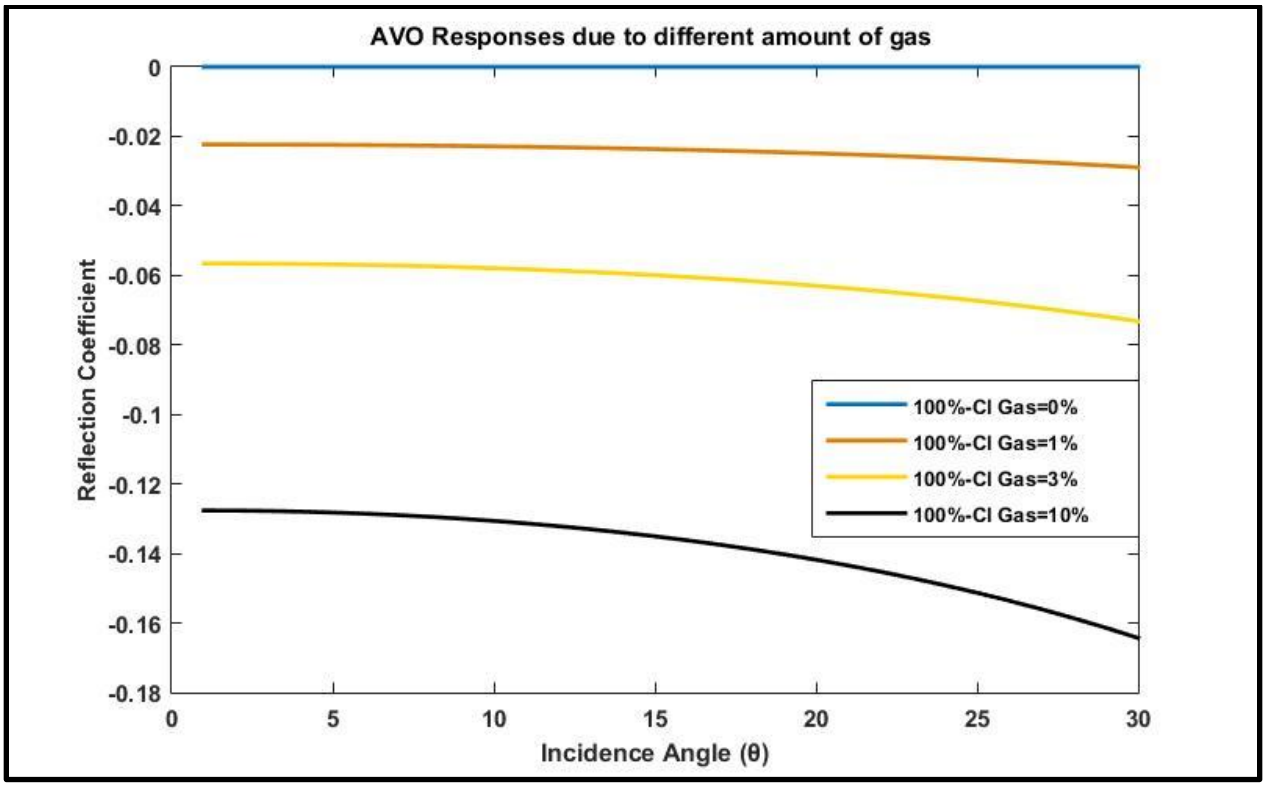

Figure 22 AVO responses for target layer has pure clay lithology (100%-Cl) has gas concentrations varies from 3% to 0% in pore space at 190 m depth. Amplitudes start to be distinctive through gas increasing after 3% gas concentration in pore space. Notably, the AVO response for these gas concentration is only about %10 at 20 degrees. This response is again less than what we might observe for near lithostatic pore pressure.

As a summary of the above scenarios, it is observed that a 5% porosity increase in sediment lithology and the high pore pressure ratio ~0.5 have a similar effect on seismic velocities and AVO responses. High pore pressure ratios exceeding $\lambda^*=0.7$ and approaching 0.9 lead to significant reduced S-wave velocities and Vp/Vs ratios of ~8 or more. Observations of Vp/Vs ratios in this range should therefore act as tell-tale indicators for overpressure in this environment.

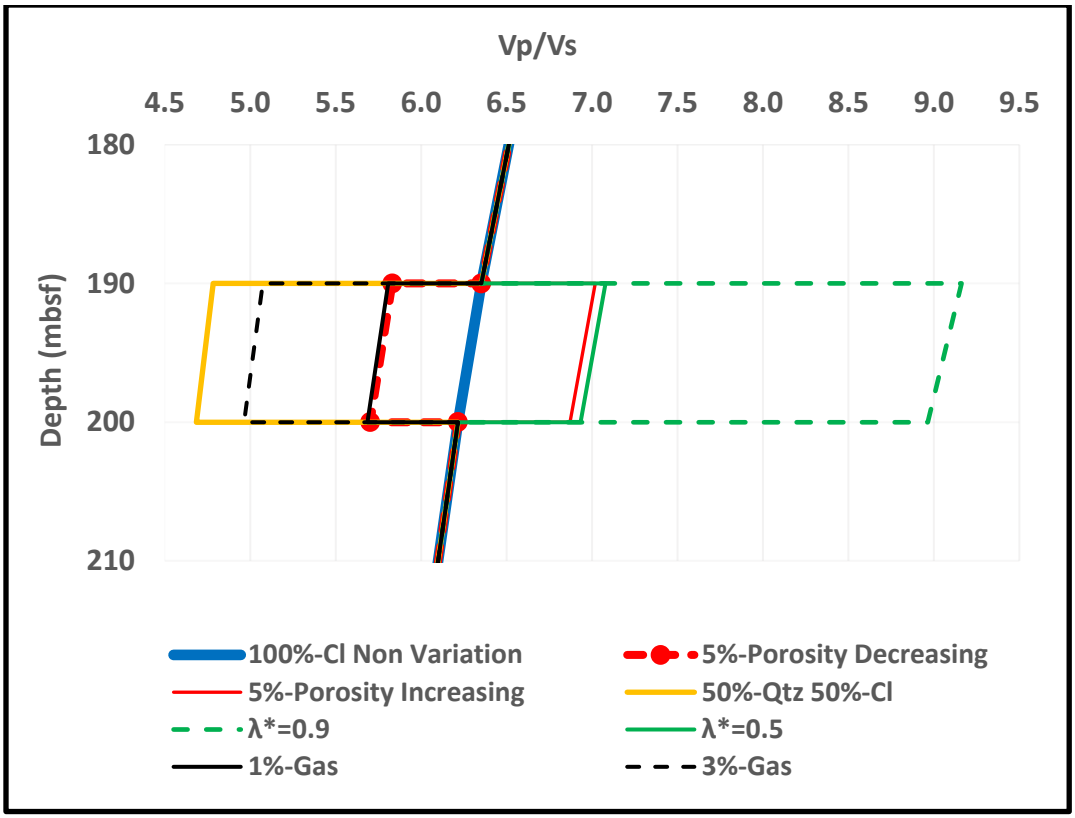

Figure 23 Vp/Vs ratios for all scenarios considered, including variations of porosity, mineralogy, high pore pressure and gas concentrations at target depths for my study. Note that, the pore pressure ratio $\lambda^*=0.5$ (solid-green line) has a comparable influence as a 5% increase in porosity and that any mineralogy change towards sand with depth (as I might expect at my study site) would drive Vp/Vs towards lower values. Vp/Vs ratios are observed as to approach 8 for high pore pressure ratios $>\sim \lambda^*=0.7$.

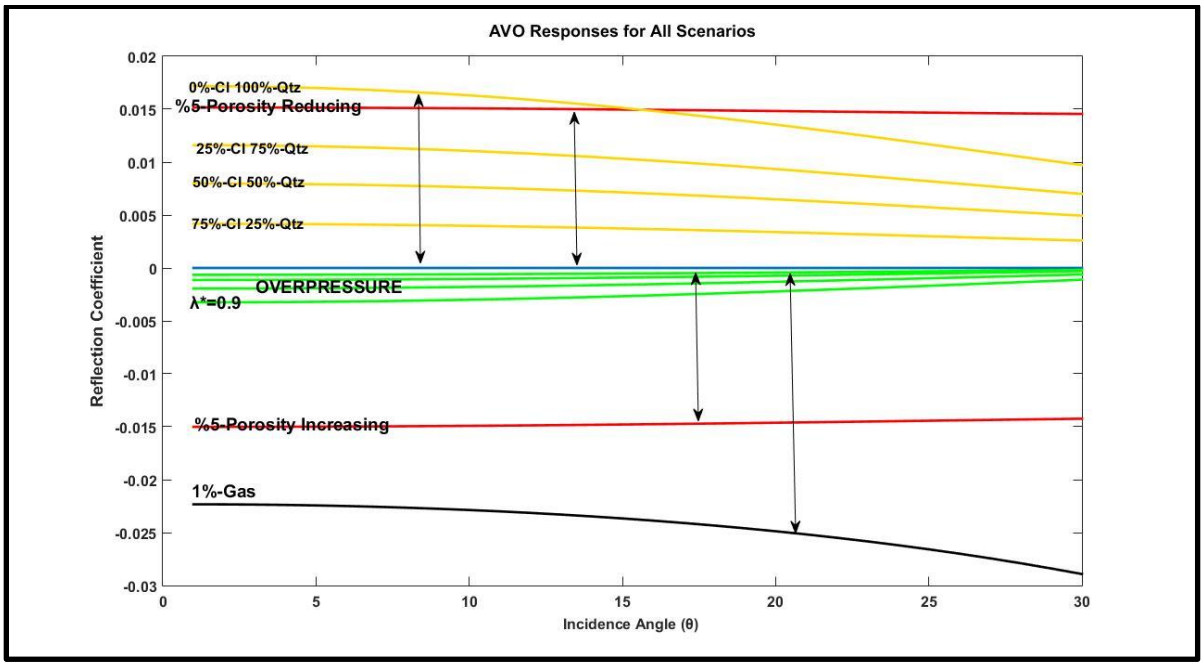

Figure 24 AVO responses for all scenarios consider variations of porosity, mineralogy, high pore pressure and gas concentrations in target sediment lithology. Note that, even small gas concentration as 1% in pore space causes greater amplitude anomaly relatively other variations.

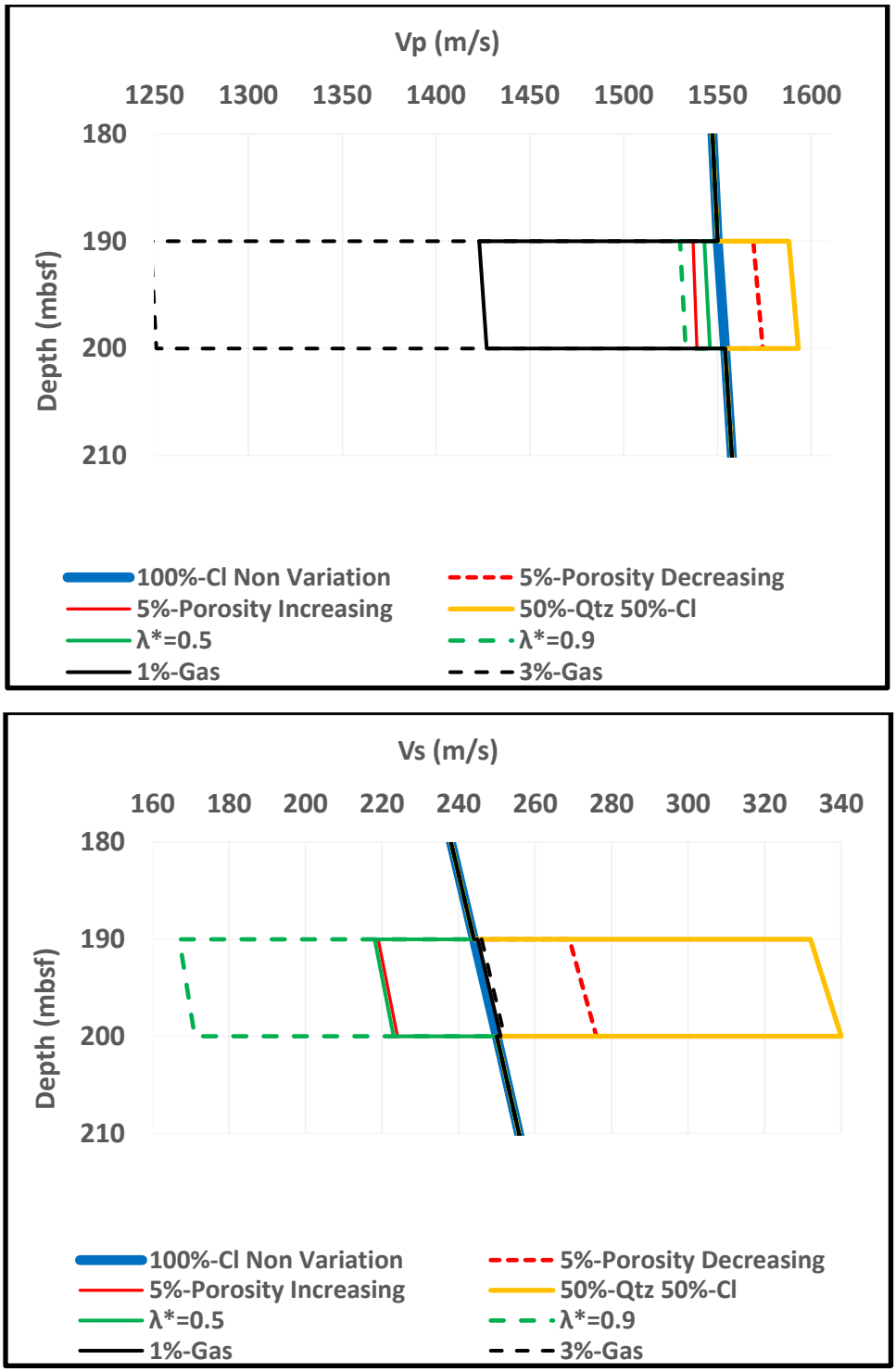

Figure 25 All scenarios effect on P-wave and S-wave velocities. Note that, some variations in porosity and mineralogy profiles have similar effect which might be caused by high pore pressure and gas concentrations such as porosity increasing-high pore pressure. These variations in sediment lithology are important because they show the values that overpressure and gas concentrations need to reach to be detectable.

Based on these scenarios, I assume that pore pressures cannot be easily detectable in Vp, Vs, Vp/Vs, or AVO responses where lithology differences between sand versus clay exceed ~50% (Figure 25). However, given that evidence exists only for increasing sand content with depth at this site (Marmara-1, Final well report)**,** I would expect Vp/Vs values to drop perhaps more than Hamilton models predict. Any increase in Vp/Vs beyond predicted Hamilton values at the Marmara Sea Site can only be attributed to two things—increased porosity, increased pore pressure, or both. Notably, both are signs of elevated fluid pressure, since an anomalous increase in porosity is generally associated with higher sedimentation and lower compaction rates that lead to increased fluid pressure. In summary, if I find zones where Vp/Vs ratios are above values predicted by Hamilton, I have strong evidence for elevated fluid pressure at the site.

2.4 Using Normal Distribution - AVO Analysis to Detect Over-pressure

To determine how well I can detect high pore pressure, I also conducted a sensitivity study where I ran a normal distribution simulation showing how well I can detect elevated pore fluid pressure when I assume typical (0-5%) porosity uncertainty and 20-100% subsurface sediment mineralogy (clay to sand) uncertainty. I focus on variations in porosity and mineralogy, since these elements have the largest impact on Vp and Vs. I calculated P and S-wave velocities 10.000 times at the target layers at different depths below seafloor (190, 290, and 390 mbsf) which have (0-5%) porosity uncertainty and various elevated pore pressures (λ^*=0, 0.5, 0.7, and 0.9).

In the first simulation, I observe the sensitivity of P-wave and S-wave velocities for $\lambda^* = 0.5$ and $\lambda^* = 0.9$ elevated pore pressure ratios in an assumed target sediment layer at 190 mbsf depth with random 0-5% porosity variation and random 20%-100% clay vs. sand mineralogy. For λ^*=0.5, I observe anomalously low P-wave velocities below the 2-sigma (standard deviation) value only 5% of the time (Figure 26). This indicates that λ^*=0.5 will not be detectable. For

λ^*=0.9, I observe anomalously low P-wave velocities below the 2-sigma value 30% of the time (Figure 26). This indicates that I would only be able detect near-lithostatic pressure using P-wave velocities half the time. The ability to detect elevated pore pressure using S-wave velocities is higher. For λ^*=0.9, S-wave velocities are 2-sigma lower than mean values 99% of the time and this is the maximum value, indicating I can detect near-lithostatic pore pressure a majority of the time by analyzing S-waves. (Figure 26).

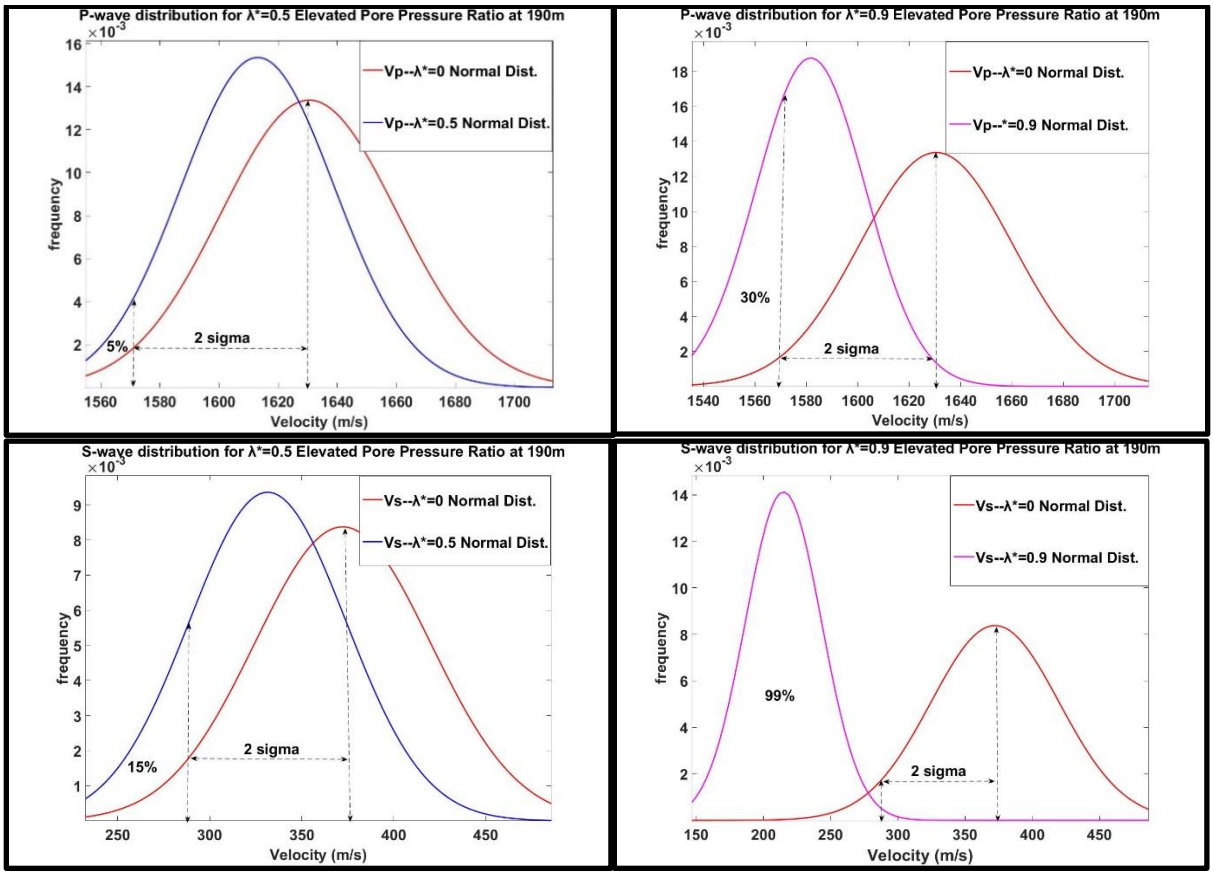

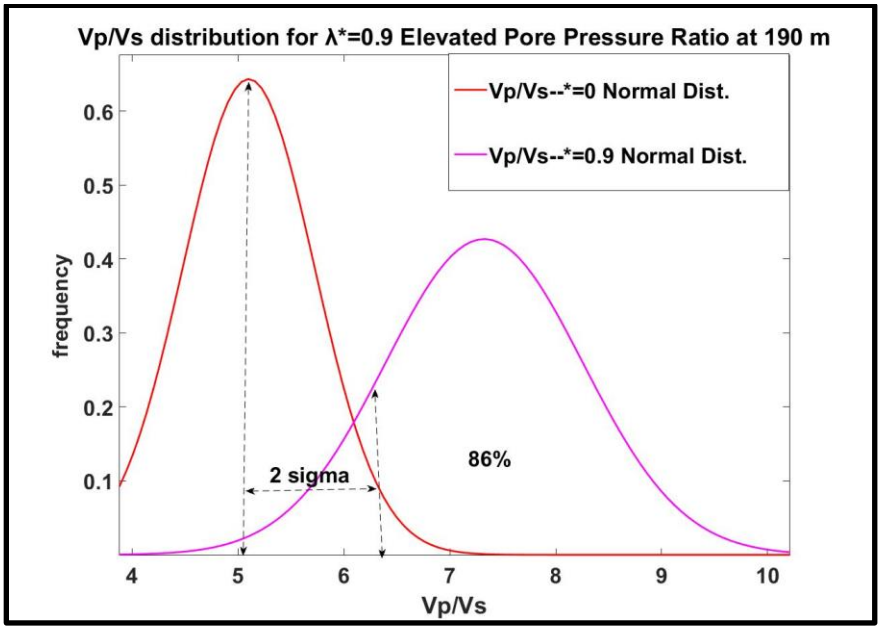

Figure 26 P-wave and S-wave velocity sensitivity for a target sediment layer at 190 mbsf depth that has random 0-5% porosity variation and random 20-100% clay vs. sand mineralogy. The normal distribution model is run 1000 times for each example. Results show the velocity range for P-wave and S-wave velocities assuming hydrostatic pore pressure (red), λ*=0.5 overpressure (blue), and λ*=0.9overpressure (magenta).

For the λ^*=0.9 overpressure example, 30% of calculated P-wave velocities and 99% of S-wave velocities are below the 2-standard deviation confidence level where no overpressure exists.

In the second simulation, I observe the sensitivity of P-wave and S-wave velocities within the same porosity and mineralogy ranges for the same elevated pore pressure ratios at 390 mbsf depth. For λ^*=0.5, low P-wave velocities below the 2-sigma value were almost equal to first simulation results as only 5% of the time (Figure 27) and illustrates that λ^*=0.5 will not be detectable. For λ^*=0.9, P-wave velocities below the 2-sigma value significantly increase relatively to the first simulation to 85% of the time (Figure 27). For λ^*=0.9, S-wave velocities are 2-sigma lower than mean values 96% of the time, a small percentage less than first simulation. Additionally, with significantly increased P-wave velocities, Vp/Vs ratios below the 2-sigma value reach maximum 97% (Figure 27) of time and provides higher detection rates of near-lithostatic pore pressure by analyzing Vp/Vs ratios.

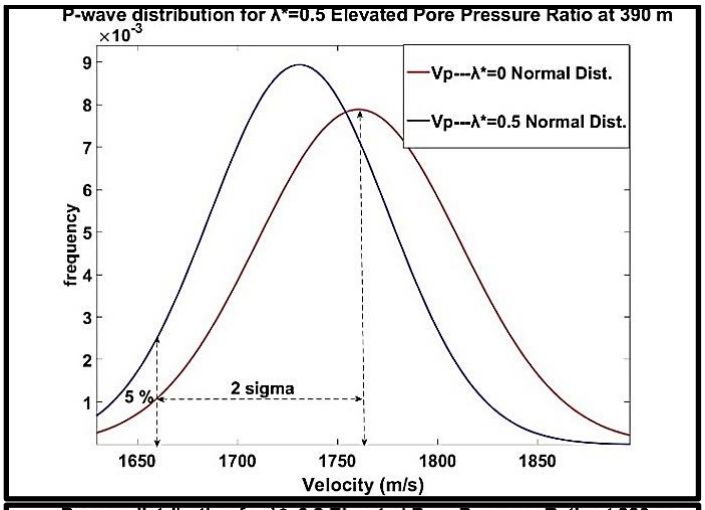
P-wave distribution for λ*=0.5 Elevated Pore Pressure Ratio at 390 m
×10^-3
Vp---λ*=0 Normal Dist.
Vp---λ*=0.5 Normal Dist.
frequency
5 %
2 sigma
Velocity (m/s)

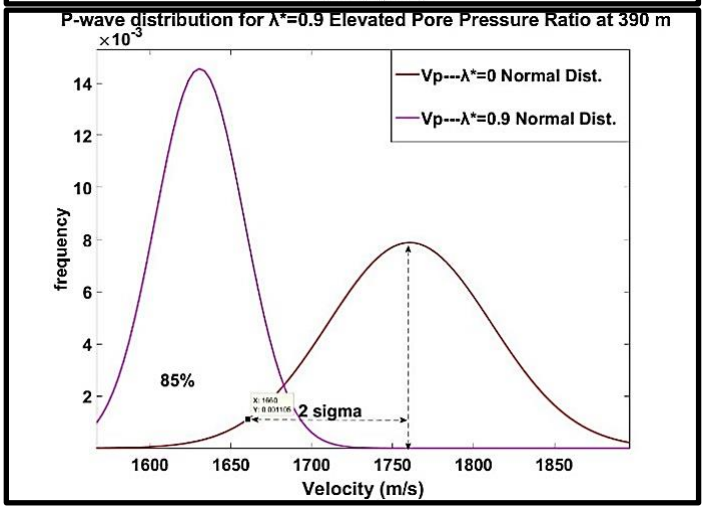
P-wave distribution for λ*=0.9 Elevated Pore Pressure Ratio at 390 m
×10^-3
Vp---λ*=0 Normal Dist.
Vp---λ*=0.9 Normal Dist.
frequency
85%
2 sigma
Velocity (m/s)

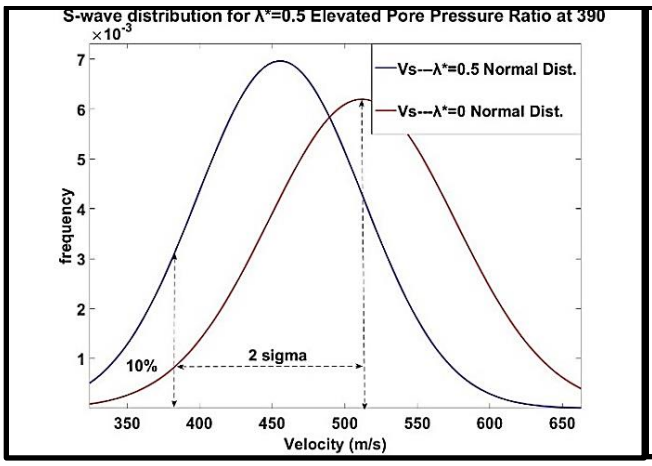
S-wave distribution for λ*=0.5 Elevated Pore Pressure Ratio at 390
×10^-3
Vs---λ*=0.5 Normal Dist.
Vs---λ*=0 Normal Dist.
frequency
10%
2 sigma
Velocity (m/s)

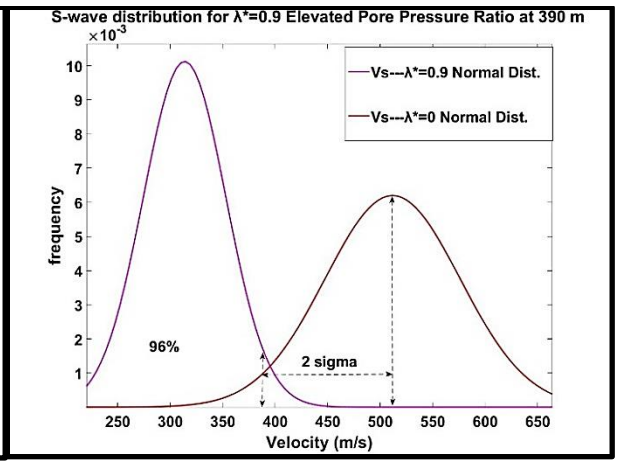
S-wave distribution for λ*=0.9 Elevated Pore Pressure Ratio at 390 m
×10^-3
Vs---λ*=0.9 Normal Dist.
Vs---λ*=0 Normal Dist.
frequency
96%
2 sigma
Velocity (m/s)

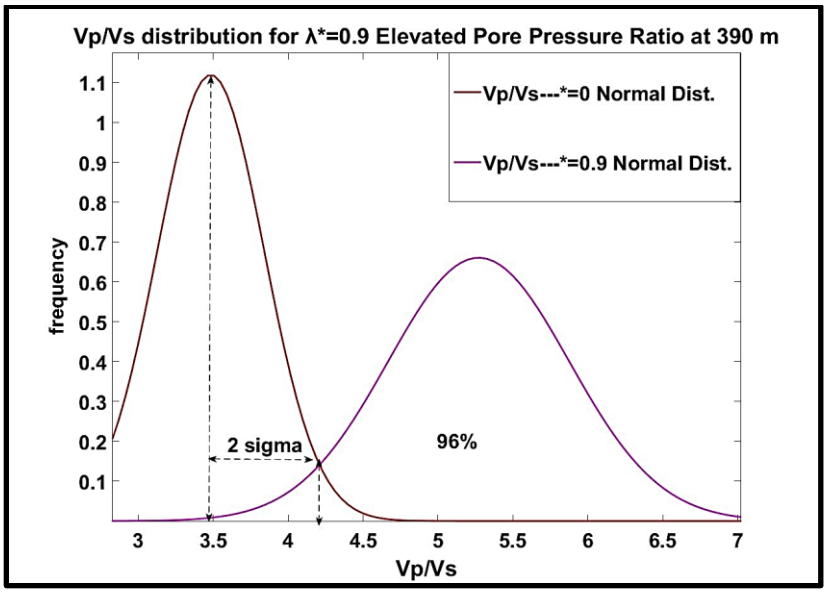

Figure 27 P-wave and S-wave velocity sensitivity for a target sediment layer at 390 mbsf depth that has random 0-5% porosity variation and random 20%-100% clay vs. sand mineralogy. The normal distribution sensitivity model is run 1000 times for each example. Results show the velocity range for P-wave and S-wave velocities assuming hydrostatic pore pressure (red), λ*=0.5 % overpressure (blue), and λ*=0.9 overpressure (magenta). Note that, for the λ*=0.9 overpressure example, 85% of calculated P-wave velocities and 96% of S-wave velocities are below the 2-standard deviation confidence level where no overpressure exists and provides 96% of calculated Vp/Vs ratios below the 2-standard deviation confidence level.

My sensitivity calculation analysis indicates that, even in the absence of significant (<1%) gas concentration in the pore space, high pore pressures should only be detectable using P-wave velocities in the most extreme cases (when sediment pore pressure is more than 90% (λ*=0.9) of lithostatic values). In contrast, S-wave velocity (which are insensitive to gas in pore space) appears much more sensitive to elevated pore pressures, and appears detectable more than ~50% of the time when pore pressures exceed ~70% of lithostatic pressure, and are clearly detectable at 90% of lithostatic values. When pore pressure approaches lithostatic (λ*=0.9) and both P-wave and S-wave velocities approaching maximum of time, Vp/Vs ratios also approaches the maximum of

time. However, after they reach maximum of time, these values decrease at greater depths with decreasing porosity.

Therefore at least in theory, using seismic velocity analysis, and especially S-wave velocities and Vp/Vs ratios derived from AVO techniques, I should be able to locate zones where near lithostatic pore fluid pressure exists.

CHAPTER 3

3.1 First Approach Test Case: Blake Ridge

As an initial test case to confirm that my approach of estimating Vp from Dix Equation and Vs from AVO analysis works properly, I run a test case at the Blake Ridge, off-shore the United Southeastern coast. There are three reasons I used this site as an initial test case. First, the seismic data on the Blake Ridge are of higher quality with longer offsets than the Marmara Sea and therefore, easier to initially process and interpret. Second, The Blake Ridge, unlike the Marmara Sea, has both well-logs and core samples available, and therefore, subsurface mineralogy, porosity and subsurface velocity are well constrained to within a few percent; and third, drilling results on the Blake Ridge clearly show both where gas and (2) elevated fluid pressures (as well as high sedimentation rates that can drive overpressure development) likely exist in the subsurface. With the physical properties at Blake Ridge well constrained, I can therefore test how well gas and over pressured zones can be detected. If the approach is successful at Blake Ridge where physical properties are well constrained, then I will feel comfortable applying it to a less constrained system like the Marmara Sea.

In this approach, I analyze one 2D seismic section, Line 11X_SIN1-600. The upper 500 m of sediment in this seismic line consist mostly of Pliocene and Miocene age sediment deposited at a high rate (0.1 - 0.35 m/kyr). The data clearly show a significant Bottom Simulating Reflector (BSR) associated with the gas hydrate phase boundary at a depth of approximately 400 mbsf. For

this seismic survey, shots were recorded by 324 groups of channels at a 2 ms sample rate with the streamer and airguns towed at depth of 2.5 mbsl. The water depth is 2875 m, the Nyquist frequency is 250 Hz; the minimum offset between the first channel and source is 60 m while the group interval spacing is 12.5 m for a maximum offset of 4097.5 m, and the shot interval is 37.5 m. I initially loaded and processed this seismic line starting with the raw shot gathers using Promax Software and these processing steps included;

1-Loading raw data and quality control application by Ormsby band-pass filtering the shot gathers, and removing bad traces dominated by noise,

2-The sorting of filtered data into CMP gathers by assigning traces to the midpoint location between shot point and receivers based on field geometry (Yilmaz, 2001).

3-Velocity Analysis conducted Dix equation on CMP gathers for the entire line.

Then, for the AVO analysis I,

4-Applied a spherical divergence correction using the velocities derived from velocity analysis, and checked the amplitude spectrum of near and far offset traces

5- Applied NMO (Normal Move-out) correction using the velocities derived from velocity analysis, then stacked separately both near and far offset traces to improve signal to noise,

6-Since the data in time (Two Way Travel Time-TWTT) domain, applied time-depth conversation using;

$$\text{Depth}(m) = \frac{\frac{1}{2}\text{TWTT(s)}}{\text{Water Velocity } (1500\ m/s)} \quad (21)$$

equation where Water Velocity equals 1500 m/s which is P-wave velocity in water.

7-Calculated the relative change in amplitude compared to the seafloor at 75 mbsf depth intervals,

8-Statistically compared over 75 mbsf depth intervals the average change in absolute value of the amplitude versus the offset from zero to 20 degrees, and

9-Calculated the Vs value necessary to cause these change in amplitude using equation (Section 2.14 Vs derivation from G)

I then plot Vp/Vs ratio profile and compared values with those measured at Blake Ridge. I use these results to estimate where both gas and elevated overpressures likely exist at this site.

3.1.1 Data Filtering

In first editing step, the raw data from shot gathers were analyzed in frequency domain and both swell noises sourced by sea waves at low frequencies and random noises at higher frequencies were attenuated by Ormsby Band-Pass filter with 9-15-200-250 Hz. corners.

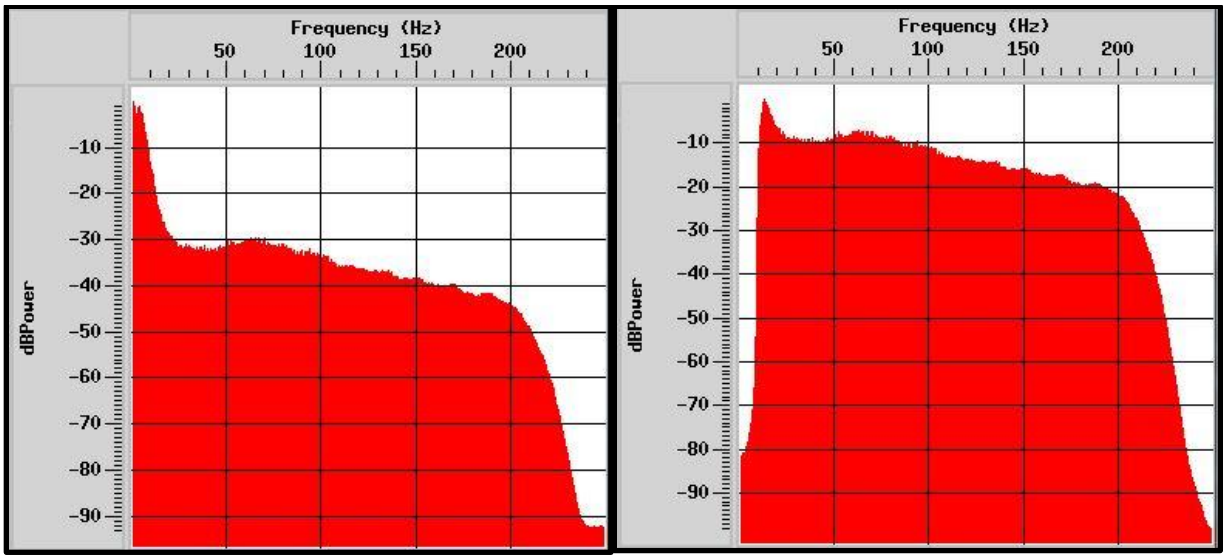

Figure 28 The Frequency Spectrum of Shot No: 3 Note that swell noises were observed with high amplitudes at low frequency band in unfiltered data (left) then they were attenuated with bandpass filter 9-15-200-250 Hz (right).

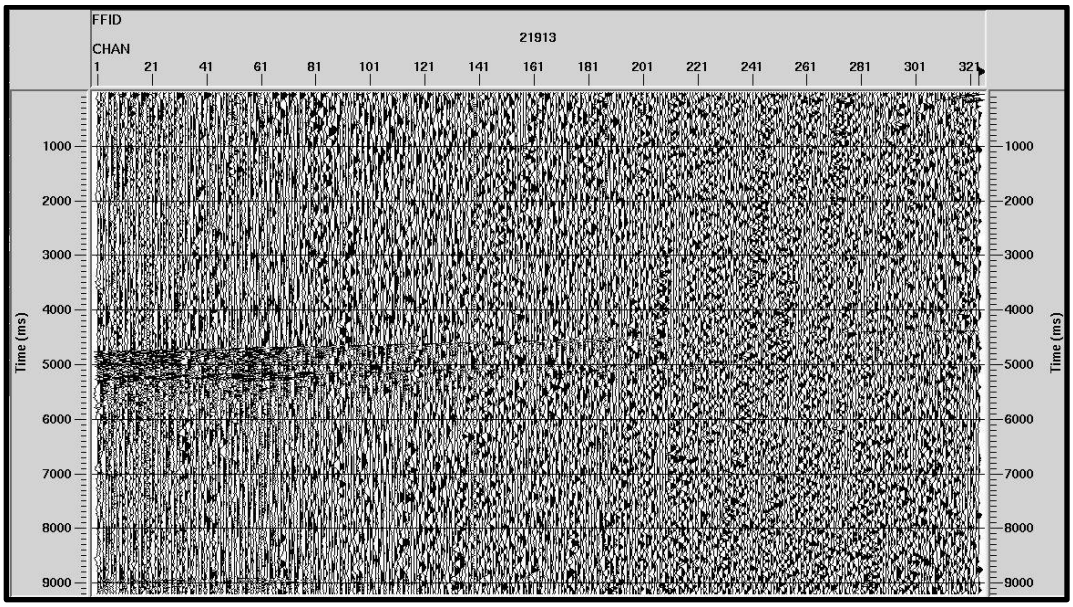

Figure 29 Line 11X_SIN1-600 Raw Seismic Reflection Section of Shot Gather (Shot No: 3)

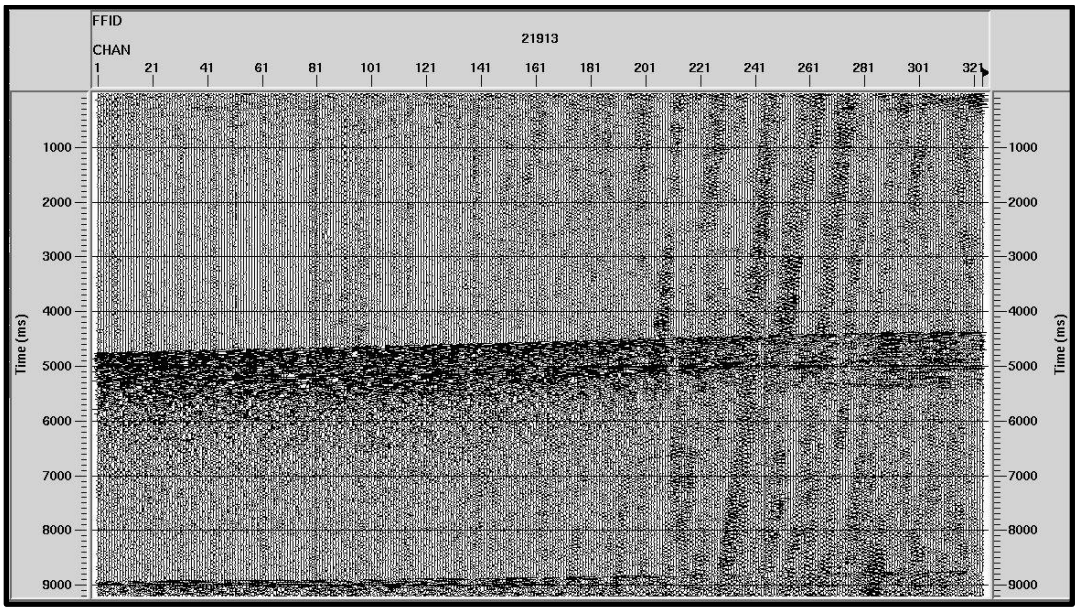

Figure 30 Line 11X_SIN1-600 Edited Shot Gather (Shot No: 3) with band-passed filter. Note that swell noises at low frequencies are attenuated and also direct wave appears in seismic section.

3.1.2 Common Depth Point (CDP) Gathering

According to Snell's Law, the reflection angle equals to incidence angle. In seismic surveys, with multiple shots, waves are recorded at channels as traces coming from common depth points (CDP) in the subsurface with different arrival times. Thus, each of CDP has a certain number of traces representing the same subsurface point. The combining all these traces in one gather for each CDP location increases signal to noise ratio and provides higher data quality for velocity analysis. The maximum number of traces or reflectors also known as fold, is calculated based on group interval, shot interval and number of receivers.

$$\text{Fold} = \frac{\text{Number of Receivers} * \text{Group Interval}}{2 * \text{Shot Interval}} \quad (22)$$

For the analyzed dataset;

$$54 = \frac{324 * 12.5\ \mathrm{m}}{2 * 37.5\ \mathrm{m}}$$

For Line 11X_SIN1-600, fold number was calculated as 54. The aim of sorting seismic data by CDP gathers is stacking band-pass filtered traces at zero offset after normal moveout correction to increase signal-noise ratio (S/N) and to allow access to AVO characteristics that I can use to derive Vs, as the reflection points are the same but the angle of incidence is different for each CMP trace.

3.1.3 Velocity Analysis and Normal Moveout (NMO) Correction

In reflection seismology, reflected waves are recorded by each receiver at different offset with different arrival times caused by shot-receiver offset. This reflection arrival time (t) is a function of shot-receiver offset (x), velocity of medium (V) and two-way travel time (t_0) at zero offset (Yilmaz, 2001). Thus, arrival times increase with increasing offset, however each of them are coming from same subsurface location in CDP gathering. These late arrivals form a hyperbola in time offset plots for each reflective layer.

$$t^2 = (t_0)^2 + \frac{x^2}{V^2} \quad (23)$$

To make a proper image that allows us to stack all the CMP gathers together, the later arrival times (t) of these hyperboal need to be flattened with normal moveout (NMO) correction before

traces are stacked. This correction (Δt_{NMO}) is the difference between arrival times (t) at offsets > 0 and the two-way travel time at zero offset (t_0),

$$\Delta t_{NMO} = t - t_0$$

where;

$$\Delta t_{NMO} = t_0 * \left[\sqrt{1 + (\frac{x}{V_{NMO} * t_0})^2} - 1 \right]$$

(24)

For accurate NMO correction and flattening traces at zero offset, the root-mean-squared (RMS) velocities (V_{RMS}) from the velocity analysis are used as NMO velocities (V_{NMO}). After I converted them to interval velocities using Dix equation (Dix, 1955), I obtained both Vp values constrained (using Dix equation for flatting longer offset CMP trace reflectors) and a Vp velocity model I used to make an initial stacked seismic section for the line. With Vp constrained, I used AVO next to estimate Vs.

3.2 AVO Analysis: Initial Processing of near and far offset CMP data

For the initial AVO analysis I use to determine Vs, I compared amplitude from 3-degree offset (the nearest offset traces) to 19-degree offset (the largest offset where we observe minimal streamer feathering, ensuring the CMP gathers at this offset truly capture the right CMP location).

3.2.1 Spherical Divergence Correction

Seismic waves lose their energy depth while propagating to increasing depth through subsurface layers due to the wavefront spreading out with time. For a layered earth; amplitudes decrease by $1/V^2$*travel time (where V is RMS velocity function (V_{RMS}), which needs to be recovered as a function of travel time (Yilmaz, 2001).

In this step, I applied spherical divergence correction to recover amplitudes in the time domain and use the gain function g(t) equation.

$$g(t) = (\text{Vrms})^2 * \text{travel time} \tag{25}$$

It is important to note that near offset and far offset must have the same shaped frequency spectrum to compare during AVO analyses (Lazaratos, 2003). For the unprocessed CMP data, I observed that the near offset traces have higher frequency content than far offset, and this difference must be corrected for to ensure accurate AVO response comparisons. To address this, I filtered the CMP data with a Band-Pass filter with 9-10-40-41 Hz corners to obtain same frequency spectra both for near and far offset CDP sections.

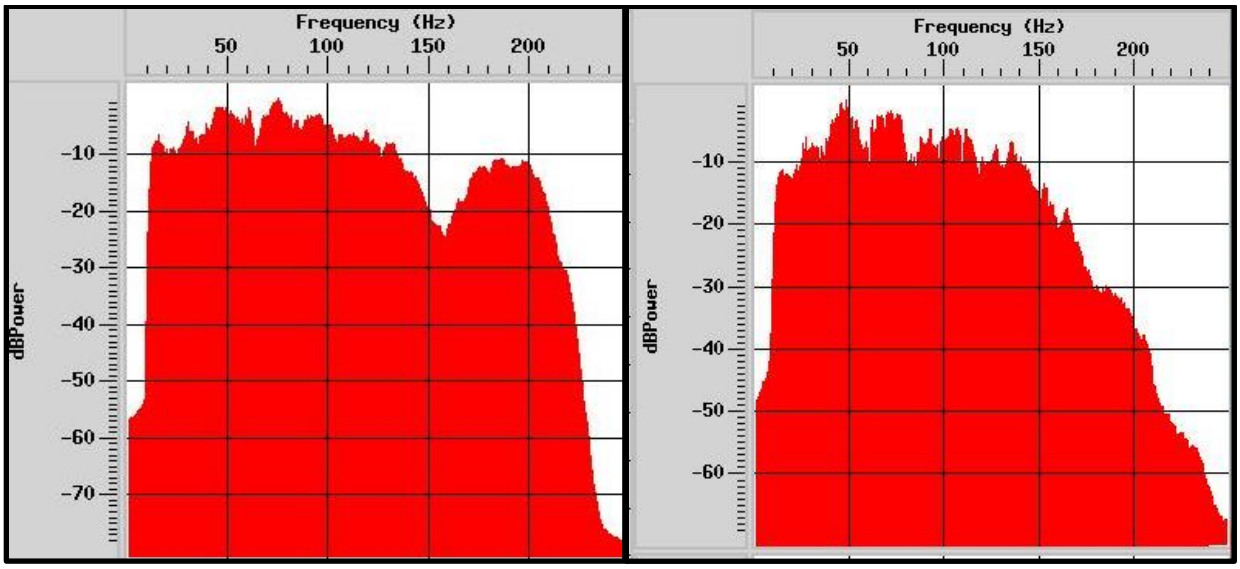

Figure 31 Near (3-degree) (Left) and Far (19-degree) Offset (Right) of entire line CDP sections frequency spectrum between 9-15-200-250 Hz. Note that above ~45 Hz we begin to observe significant differences in frequency content with far offset data having a peak frequency at 45 Hz, and near-offset data generating a peak frequency at 75 Hz. To properly compare, I filtered these data so that frequency content between near and far offset data matches, resulting in more reliable AVO comparison, but in general, lower frequency data.

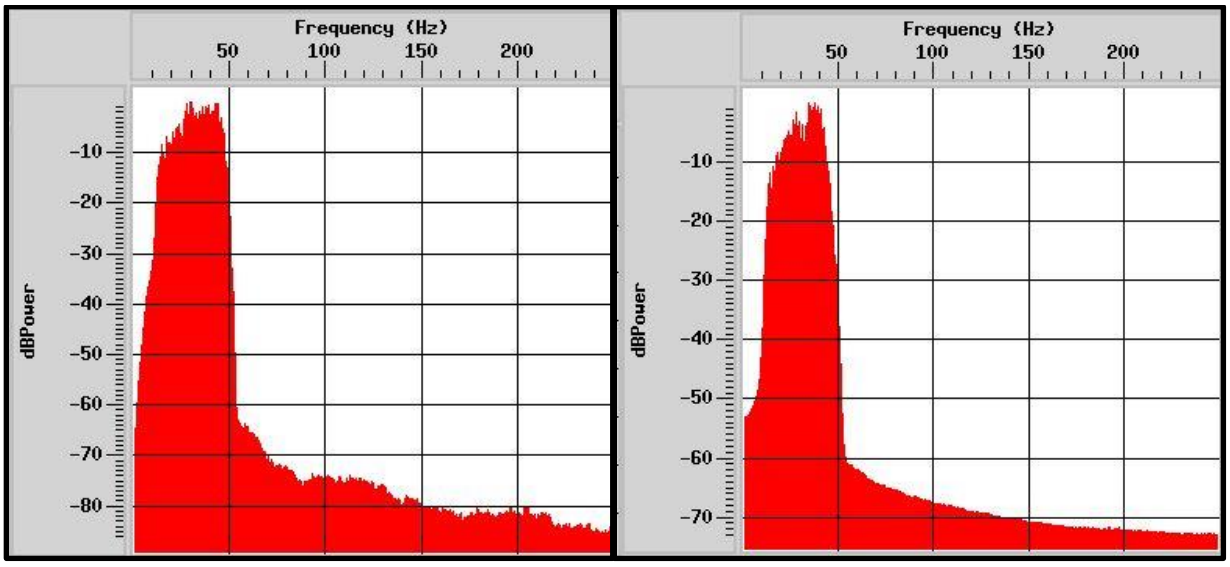

Figure 32 Near (Left) and Far Offset (Right) of entire line CDP sections has same shaped frequency spectrum between 9-15-40-55 Hz. corners.

3.2.2 Stacking separately both near and far offset traces to improve signal to noise

The main goal of AVO analysis is observing amplitude anomalies with offset, which I then intend to use to estimate Vs. Once NMO and Spherical Divergence Corrections are applied to the band-passed CDP gathers, I stacked near and far offset traces in the CDP gather separately to improve signal to noise, at the expense of losing some spatial resolution. Specifically, I stacked all traces between in range Channel 280-Channel 324 that average 3 degrees as near offset, next I stacked all traces in between range Channel 100 to Channel 160 that average 19 degrees as far offset. This provided me one near offset section and one far offset stacked section for future AVO analysis.

3.3 AVO Analyses in MATLAB

For the initial AVO analyses, I displayed near and far offset stacked CMP sections. After stacking near and far offset CDPs for Line 11X_SIN1-600 in MATLAB, I normalized each stacked trace by taking the absolute value of amplitude and dividing their amplitudes to the amplitude of sea floor reflection.

3.3.1 Analyzing Absolute Values of Near and Far Offset Amplitude

As a first step of AVO analyses for Line 11X_SIN1-600, I took the absolute values of near and far stack trace amplitudes from seafloor to a depth of ~450 mbsf, then I calculated the relative change in amplitudes.

Then I calculated the relative change in amplitude compared to the seafloor at 75 mbsf depth intervals from depth-converted lines. The average change between the absolute value of far and near offset traces in 75 mbsf depth intervals indicates amplitude anomalies along 20 degrees offset. I used these values to calculate S-wave velocities (Vs) from the gradient equation described in Section 2.2.2.

After the derivation of S-wave velocities in 75 mbsf depth intervals, Vp, Vs and Vp/Vs ratio profile are plotted (Figures 33, and 34).

The high Vp/Vs ratios (>8) suggested for higher sedimentation rates (Hornbach et. al., 2008) are generally observed in shallow sediments until 200 meters depth below sea-floor and are suggested for higher pore pressure, whereas the lower Vp/Vs ratios (<3.5) below BSR are consisted with free gas which is already known from ODP (Ocean Drilling Program) Leg 164 at deeper levels (Paull et. al., 2000).

Results of AVO analyses of Blake Ridge for my test case approach are not definitive, but they are consistent with what I would expect to observe in this region.

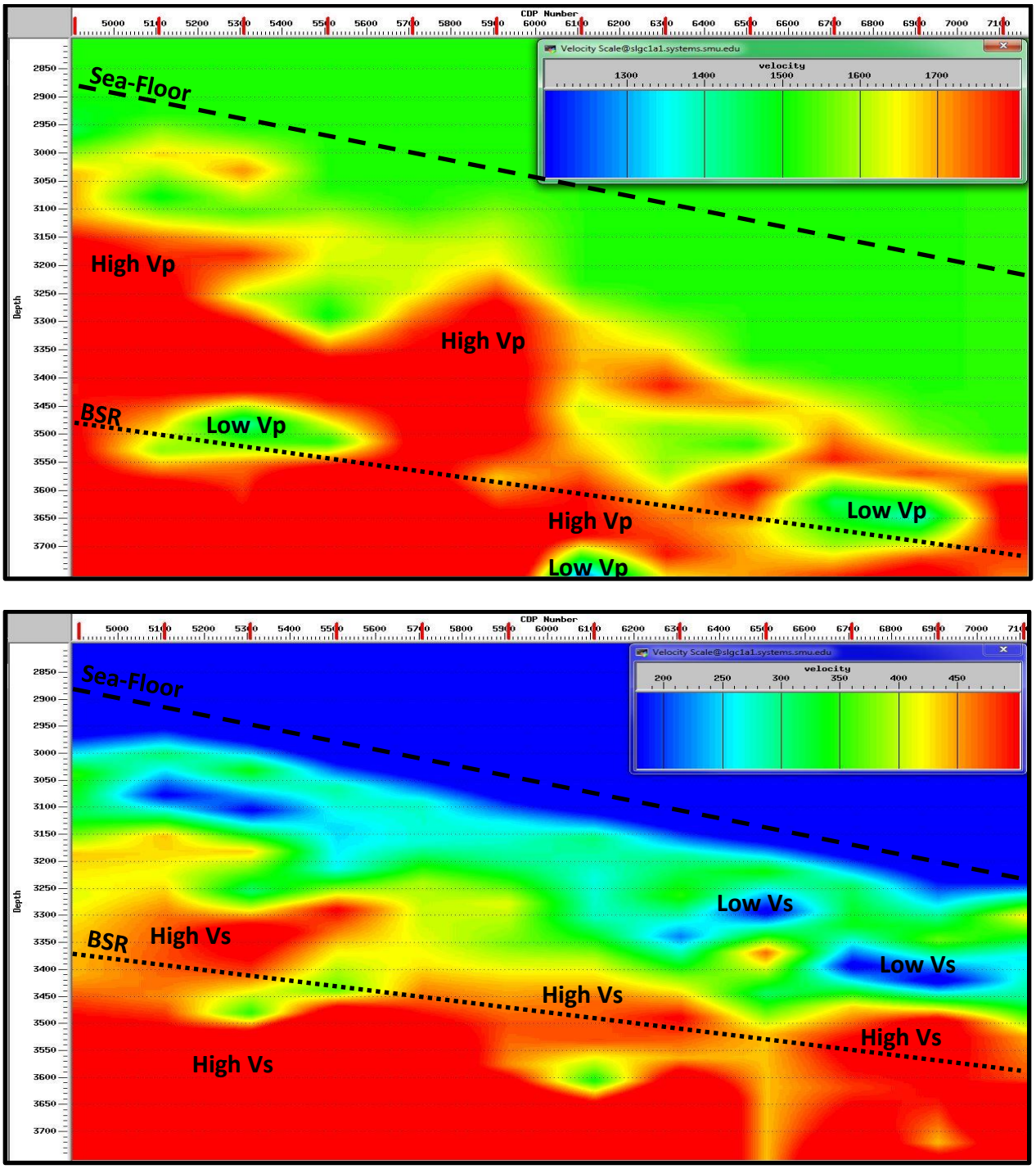

Figure 33 Blake Ridge Line 11X_SIN1-600 Vp (top) and Vs (below) velocity profiles. In both velocity profiles low velocity zones are shown by blue colors and high velocity zones are shown by red colors.

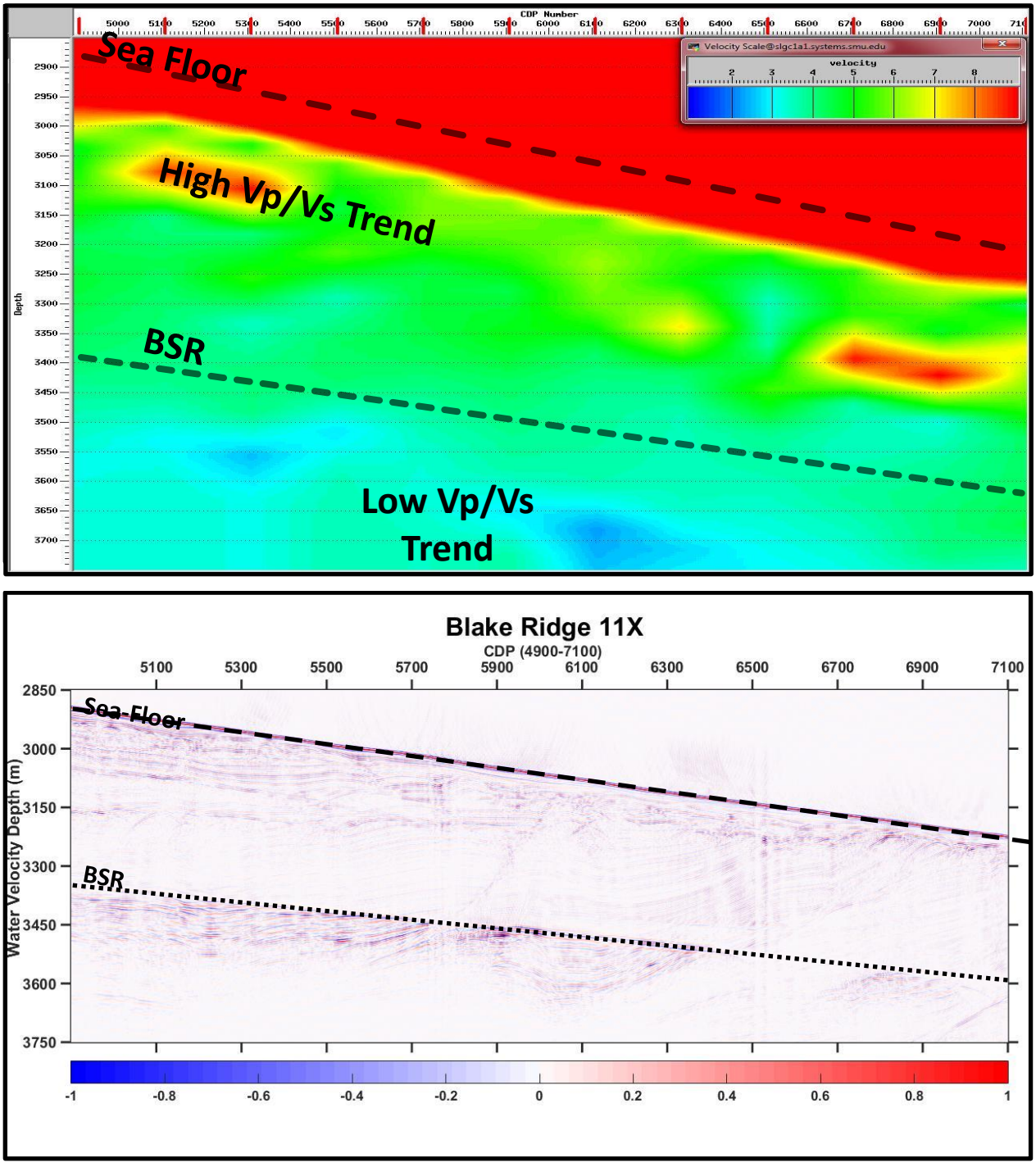

Figure 34 Vp/Vs ratio profile (top) and Blake Ridge Full Stack Seismic Section (below). The high Vp/Vs ratios (>8) suggested for high sedimentation rate, are generally observed in shallow sediments until 200 meters depth below sea-floor, whereas the low Vp/Vs ratios (<3.5), suggested gas concentrations, are observed at deeper levels.

CHAPTER 4

4.1 The Marmara Sea-2D Seismic Line

Initial Vp, Vs, Vp/Vs, and AVO analysis from Blake Ridge showed my results are consistent with what I would expect for gas detection and possible overpressure detection. As the next step of my study, I applied the same technique to the Marmara Sea, where stratigraphic interpretations suggest elevated pore pressures may exist in the upper ~150 m of seafloor sediment (Shillington et al., 2012). Specifically, I analyzed in detail one of the 2D seismic lines acquired at Central High between the Central and Cinarcik basins in the Marmara Sea (Fig. 2b. S3-Figure 35) where creep deformation is hypothesized to occur due to elevated fluid pressures (Shillington et al., 2012) (Figures 35, and 36).

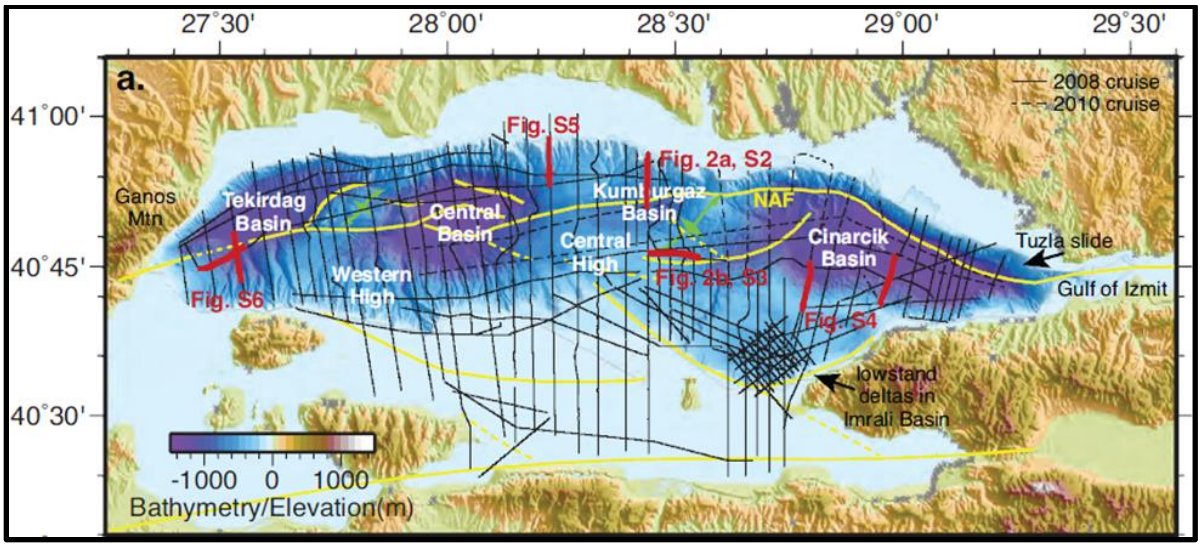

Figure 35 The bathymetry of the Marmara Sea (Rangin et al., 2001) and 2D Seismic lines (Fig. 2b. S3), collected between Central and Cinarcik Basins. Red lines show examples of MCS (Multichannel Seismic) profiles where creep like deformations is observed in this region. The yellow and green lines show major faults in this region. NAF: North Anatolian Fault) Black lines indicate the multichannel seismic lines collected during TAMAM (Turkish-American Marmara Multichannel) project (Adopted from Shillington et. al., 2012) (Dr. Magnani asked to remove Fig 2a… writes but it is hard to remove)

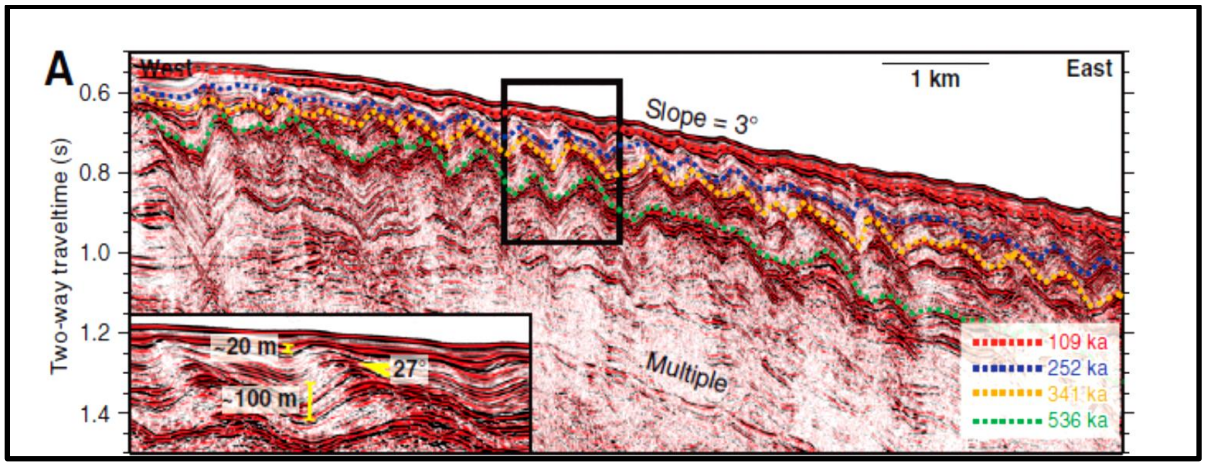

Figure 36 MCS profile (Fig. 2b. S3) indicates creep fold deformations on Central High with their stratigraphic ages. (Vertical exaggeration ~4:1 (assuming 1800 m/s) There is a 3 degree of slope, and folds continue between wave structures (Adopted from Shillington et al. 2012).

The Central High, which is an anticline between two basins, is also known to exhibit thermogenic methane release from upper sedimentary layers into the water column (Géli et al., 2010; Tary, 2011), with source rocks located in Eocene-Oligocene Thrace basin deposits below (Bourry et al., 2009). As noted with the Blake Ridge, the presence of gas in the Marmara Sea has the ability to distort Vp/Vs results, since P-wave velocities are significantly reduced by gas. I therefore looked for anomalously low Vp values to detect gas, while to detect pore pressure my focus was especially centered on AVO-derived Vs values, since these values are unaffected by possible gas presence. My hypothesis is that if I observe low Vs values in the upper 150 m of sediment that are generally below values of Hamilton (1976) or Blake Ridge (a region which consists also of mud-rich sediment like the Marmara Sea) this would provide additional geophysical evidence that the systems is indeed over pressured, and near failure (as I need over pressures approaching lithostatic values for Vs anomalies to be detected).

4.1.1 Seismic Data Background and Previous Interpretation

The seismic data from the Marmara Sea were collected on the R/V *K. Piri Reis* during of July 2008 and the June 2010 as a joint project between Columbia University and Dokuz Eylul University. The data were recorded using a 72-channel streamer longs 611.75 m, with a 12.5 m shot interval spacing, a 6.25 m receiver spacing, and a sampling interval of 1ms (See Cruise report in the appendix). The area where suspected seafloor creep exists along the upper edge of the margin, was imaged in seismic line Mar08-50. As shown in Shillington et al. (2012) (Figures 35, and 36), the evidence for creep at this site was revealed by the steady increase in sediment deformation with depth to a depth of approximately ~150 m, where the reflective character of the sediment changes. This depth (~150 m) may also be the depth where higher sand content exists within the sediments, as suggested by the Marmara-1 well log report (Marmara-1, Final well report). Shillington et al. (2012) suggest that at ~150 m depth, a decollement exists (perhaps caused by this transition in sediment mineralogy from clay-to-sand) resulting in a basal boundary for deformation. Notably, as shown by Hamilton (1976), where higher sand content exists, higher Vp and higher Vs values should exist. The sediment has sand-rich versus clay mineralogy due to better grain contacts and lower porosity is typically observed in shallowly buried marine sediment (Hamilton, 1976). Furthermore, sandy sediments with a clay cap on an anticline represent an ideal trap for fluids, promoting overpressure development. I therefore hypothesize that if the system is indeed over-pressured, I should observe anomalously low Vs and Vp velocities in the upper 150 m of sediment.

To assess whether elevated pore pressure exists, I applied the method applied for the Blake Ridge, where I derived Vs from AVO data and Vp from Dix equation to assess where anomalous Vp/Vs values exist along the Central High. The raw data was filtered by Band-Pass filtering with

19-20-200-250 Hz. corners, additionally Channel 13 and Channel 61 are observed with high noise level, and they are removed.

Again, I sorted the data into CMPs, applied spherical divergence and filtering to ensure the frequency spectrum for near and far offset data matches and then normalized amplitudes to the seafloor reflector.

For Marmara 2D Seismic Line, fold number was calculated as 18 for CMP gathering.

$$\text{Fold} = \frac{\text{Number of Receivers} * \text{Group Interval}}{2 * \text{Shot Interval}}$$

$$18 = \frac{72 * 6.25\ \text{m}}{2 * 12.5\ \text{m}}$$

(26)

During the semblance velocity analysis, I had no ability to pick expected velocities at sea floor for several CMP locations. Although the velocity value is expected to be consistent at sea floor and is approximately ~1500 m/s which equals the water velocity, traces are flattened with velocities over 1500 m/s for CMP 1200, 1300, 1800 locations (Figure 37).

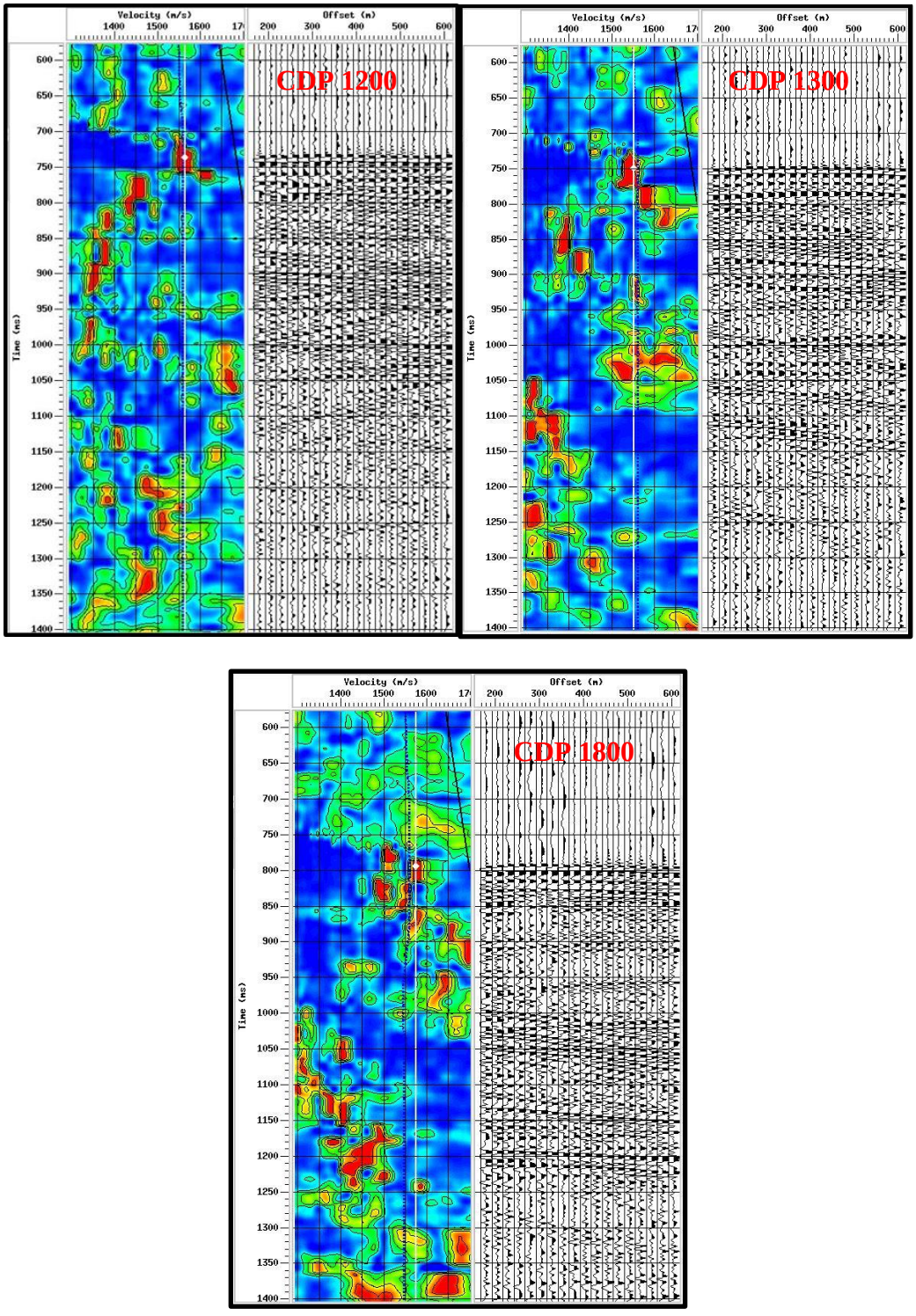

Figure 37 The interactive velocity analysis for CDP 1200 (top-left), CDP 1300 (top-right), CDP 1800 (bottom) locations that there is no ability to pick expected velocity at sea floor. Traces are flattened with velocities over 1500 m/s.

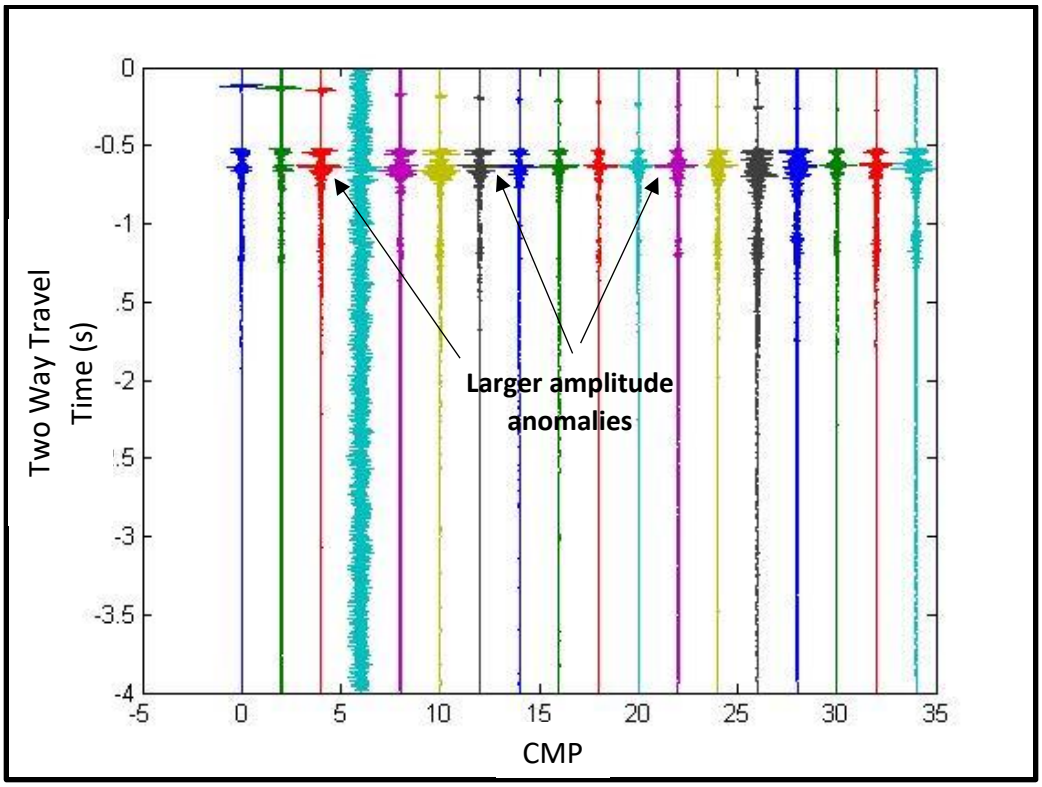

Figure 38 NMO correction of the normalized CMP gather. Note that, larger amplitude anomalies are observed with offset.

After NMO correction, I observed that some far offset traces exhibit larger amplitudes with offset (consistent with gas existing in pore space, see example in Figure 38), while other reflections that appear to have a relative reduction in amplitude. We should note that based on our early Hamilton modeling, high pore pressures should result in strong short offset amplitude events that reduce in amplitude with offset, whereas zones of high gas concentration should show strong amplitude changes that increase in amplitude with offset. Ultimately, to detect where either gas or high fluid pressures might exist, I need to address where I observe each of these phenomena at levels above expected uncertainties, and can therefore demonstrate such changes are beyond expected values for typical marine sediment that contain no gas and are not over pressured. For

"typical values", I compared results from Marmara to Hamilton (1976) predictions. Currently, based on only very preliminary results, I see the evidence for increased amplitude with offset along hypothesized failure boundaries where creep is suggested to occur (Figure 36). Whether this is an effect of free gas or other changes in the sediment character remains unclear. If it is caused by free gas, I should observe significantly reduced Vp velocities at this boundary. Analysis of Vp data using Dix Equation and CMP supergathers may provide helpful insight.

NMO corrected CMP gathers were stacked with picked RMS velocities (Vrms) at zero offset. This provided me a full stack section. Additionally, for detail AVO analyzes traces belonging to the first 6 channels were stacked as a near offset stack section (average angle of 10 degree, and traces belonging to the last 6 channels were stacked (average angle of 30 degree), I used this for my initial AVO comparison to see if any clear discrepancies exist between near and far offset data for further analysis. I applied Kirchhoff migration to all these post-stack sections to compare near and far offset images.

4.2 Initial AVO Results, Analysis and Discussion using Near and Far Offset Stacks

All three (full, near and far offset) post-stack migrated sections were normalized by dividing their amplitudes to sea floor reflection amplitude in ProMax. Then, they were displayed in MATLAB.

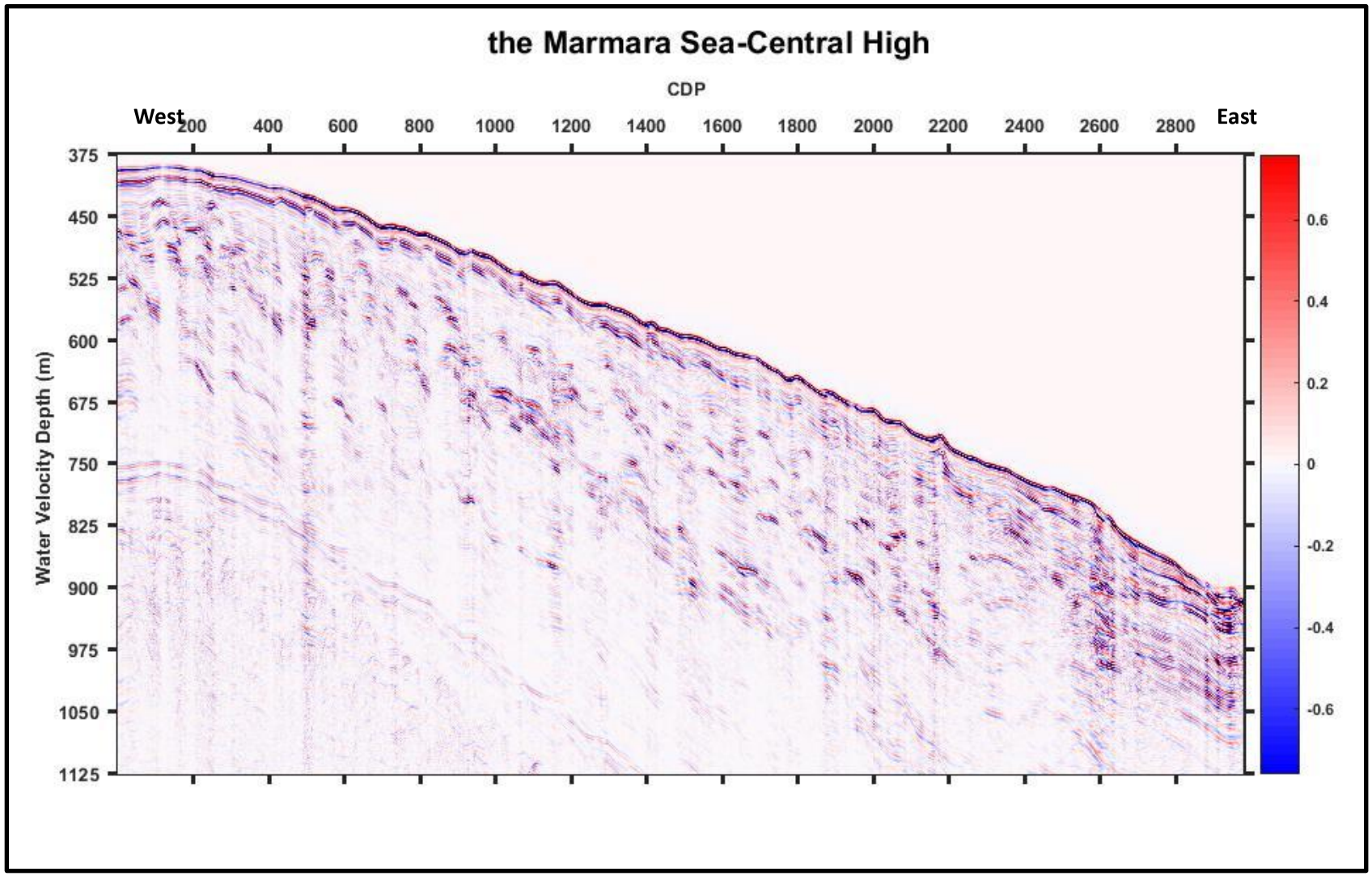

Figure 39 Marmara 2D Seismic Line Full Stack-Time Migrated Section. (Note a clear seafloor multiple observed approximately 365 m below seafloor (~365 mbsf)

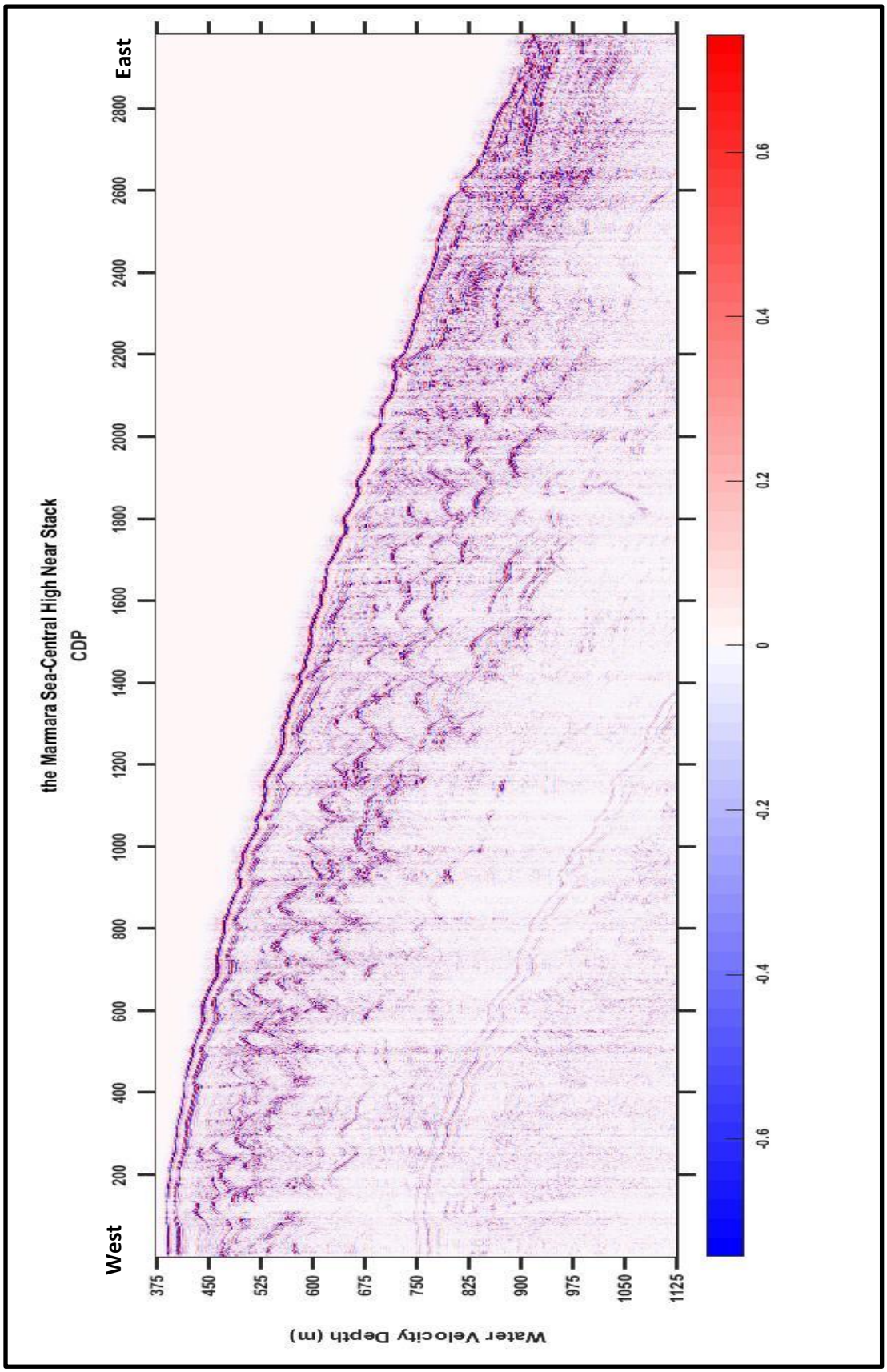

Figure 40 Marmara 2D Seismic Line Far Stack-Time Migrated Section.

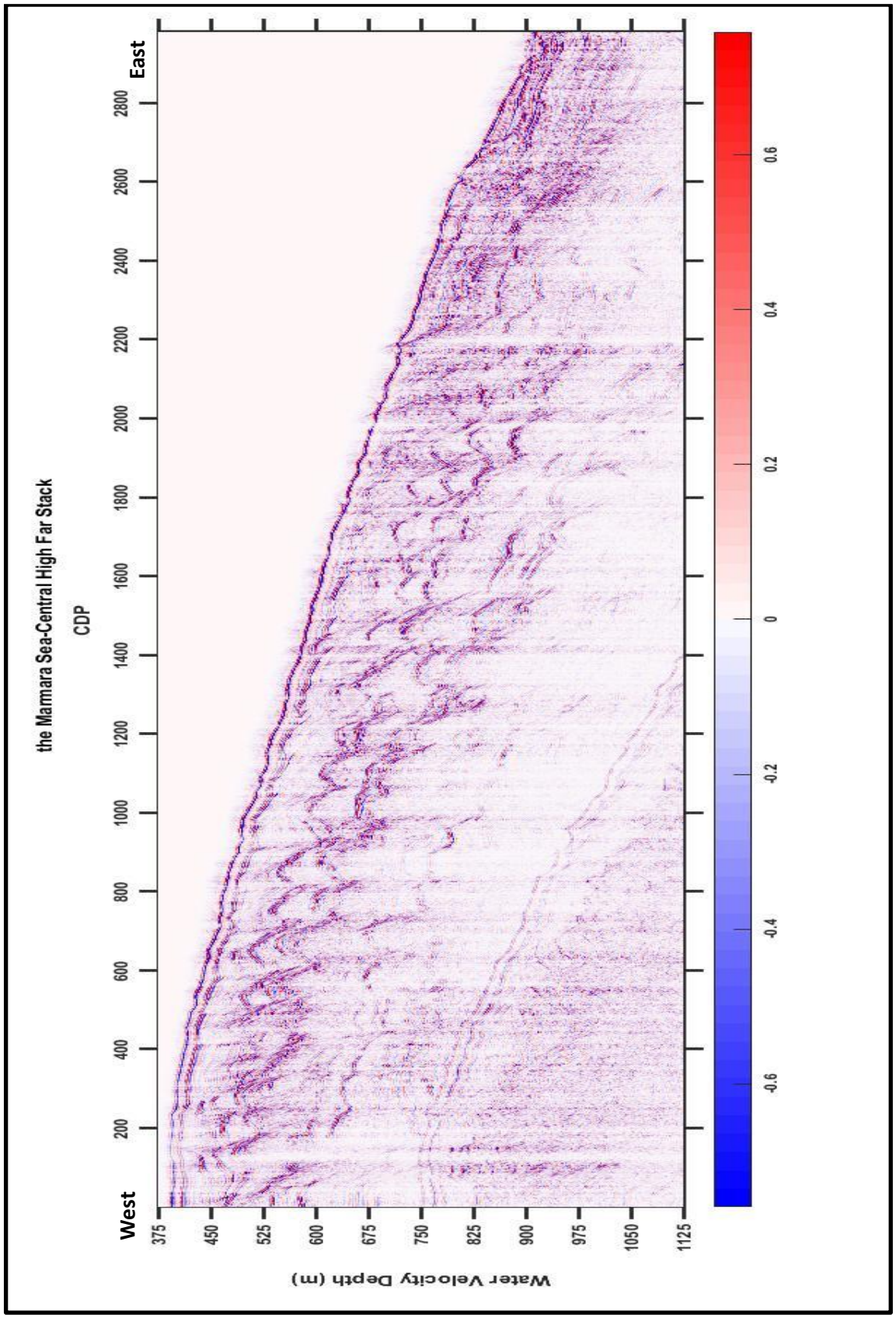

Figure 41 Marmara 2D Seismic Line Far Stack-Time Migrated Section.

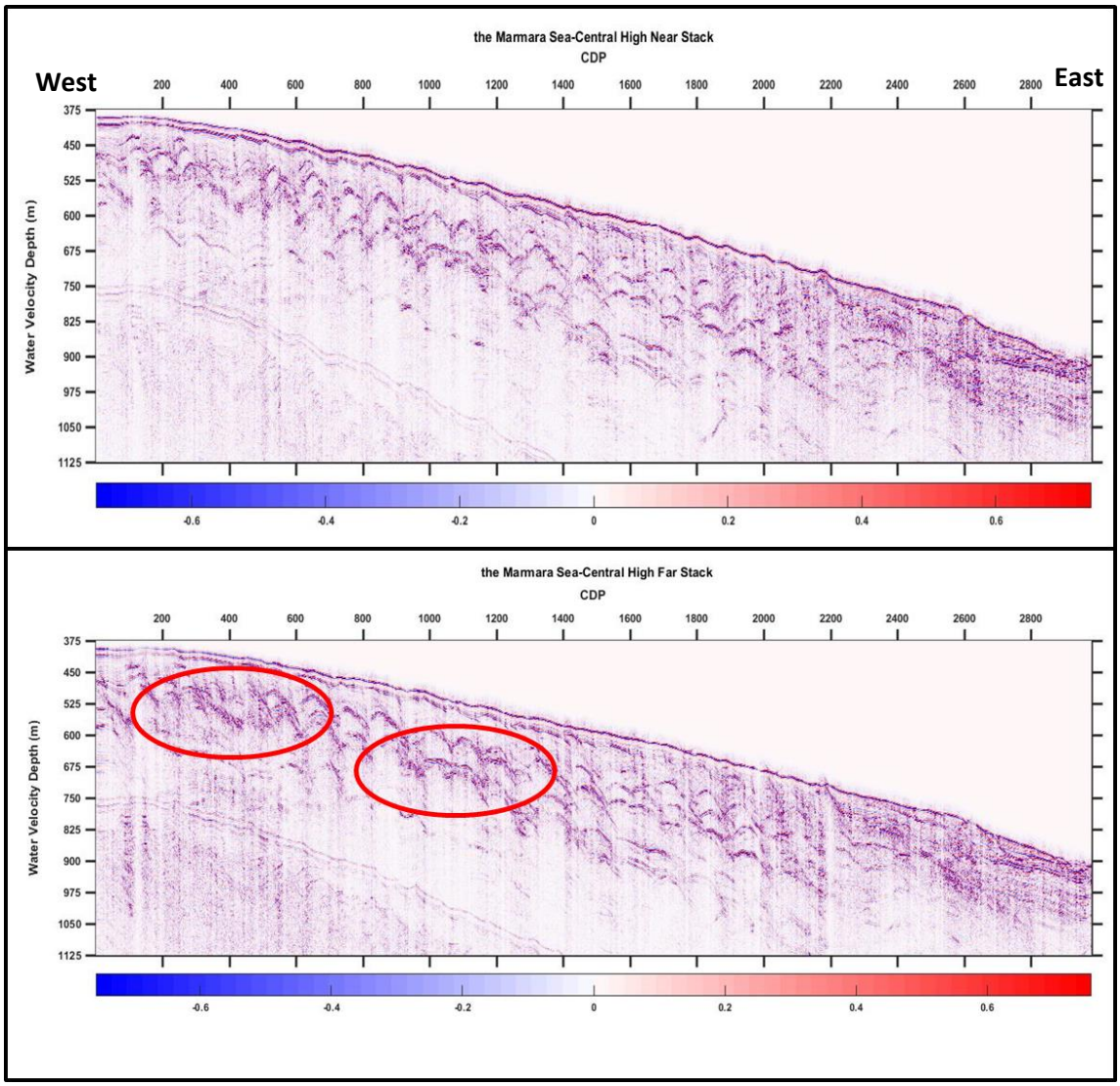

Figure 42 The comparison of Marmara 2D Full, Near and Far Stack Migrated Sections. Several reflections at far offset appeared higher amplitudes on the left side of Far Stack Migrated Section compared to the near offset at depths below ~150 m. (Black-Dashed Circles)

In post stack sections, shallow reflections (100-150 m) appeared with higher amplitudes, especially the upslope, middle portions of the section. This kind of amplitude anomaly is consistent with areas hypothesized for creep like deformation and what I would expect if free gas is present in the subsurface. Assuming very small (<1%) gas in the pore space would cause significant amplitude anomalies that can result in increasing amplitude with offset (Figure 42), this observation is consistent with gas in pores, and supports the idea that trace amounts of gas exist in the pore space at depths greater than 100-150 mbsf.

Then I followed the same method that I used in Blake Ridge section to calculate Vs values by using the average change between the absolute value of far and near offset traces in 75 mbsf depth intervals indicates amplitude anomalies along 20 degrees offset.

After the derivation of S-wave velocities in 75 mbsf depth intervals, I plotted Vp, Vs and Vp/Vs ratio profiles. Low P-wave velocities in shallow zones up to 150 mbsf depth which might be suggested as gas or overpressure, but this profile indicates higher uncertainty (Figure 42). For S-wave velocity profile, lower S-wave velocities are observed in mostly shallow zones and they are more consistent to hypothesized overpressure zones in previous research (Shillington et. al., 2014) (Figure 43).

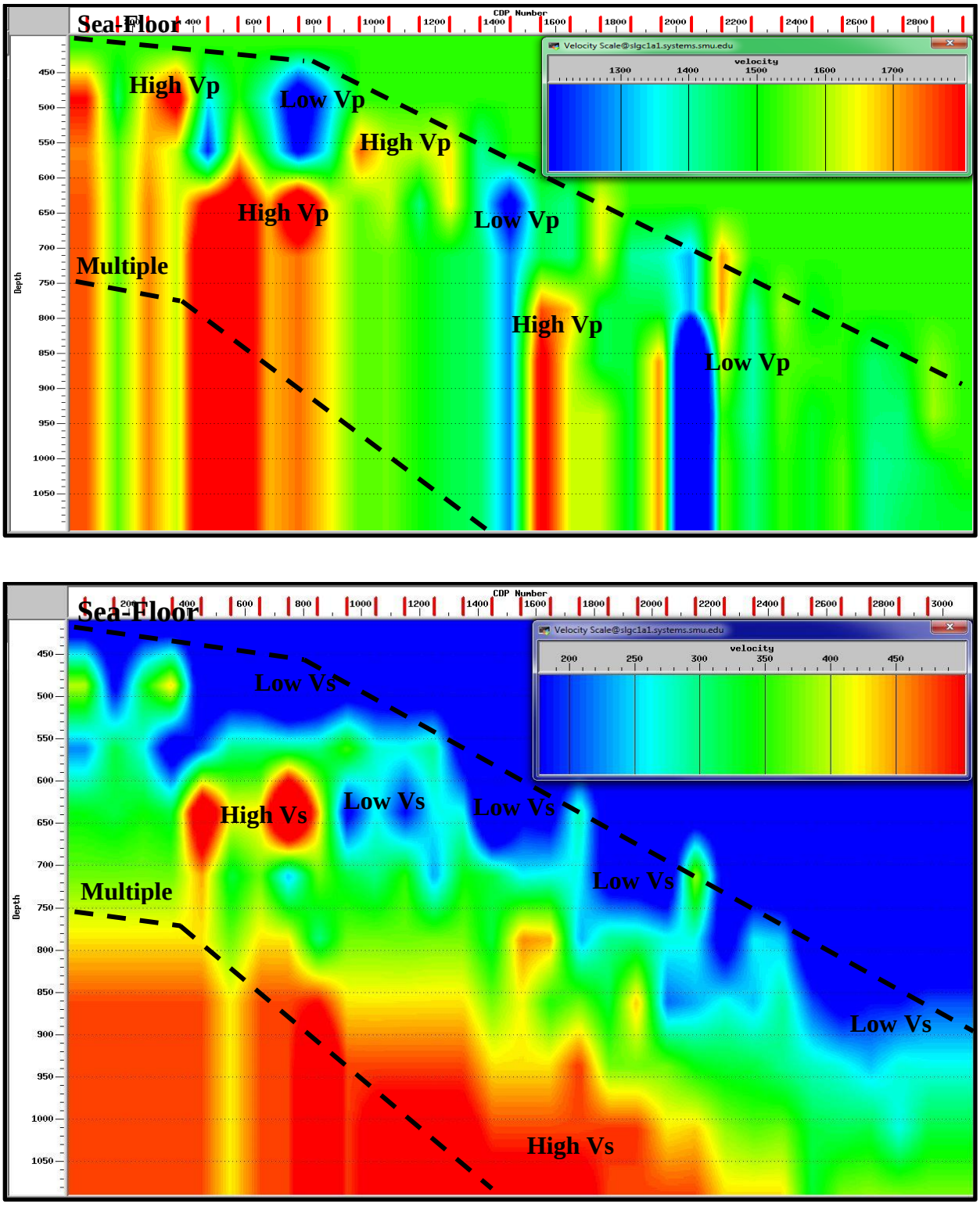

Figure 43 Central High-Marmara Vp (top) and Vs (below) profiles. Vp (top) and Vs (below) velocity profiles. In both velocity profiles low velocity zones are shown by blue colors and high velocity zones are shown by red colors.

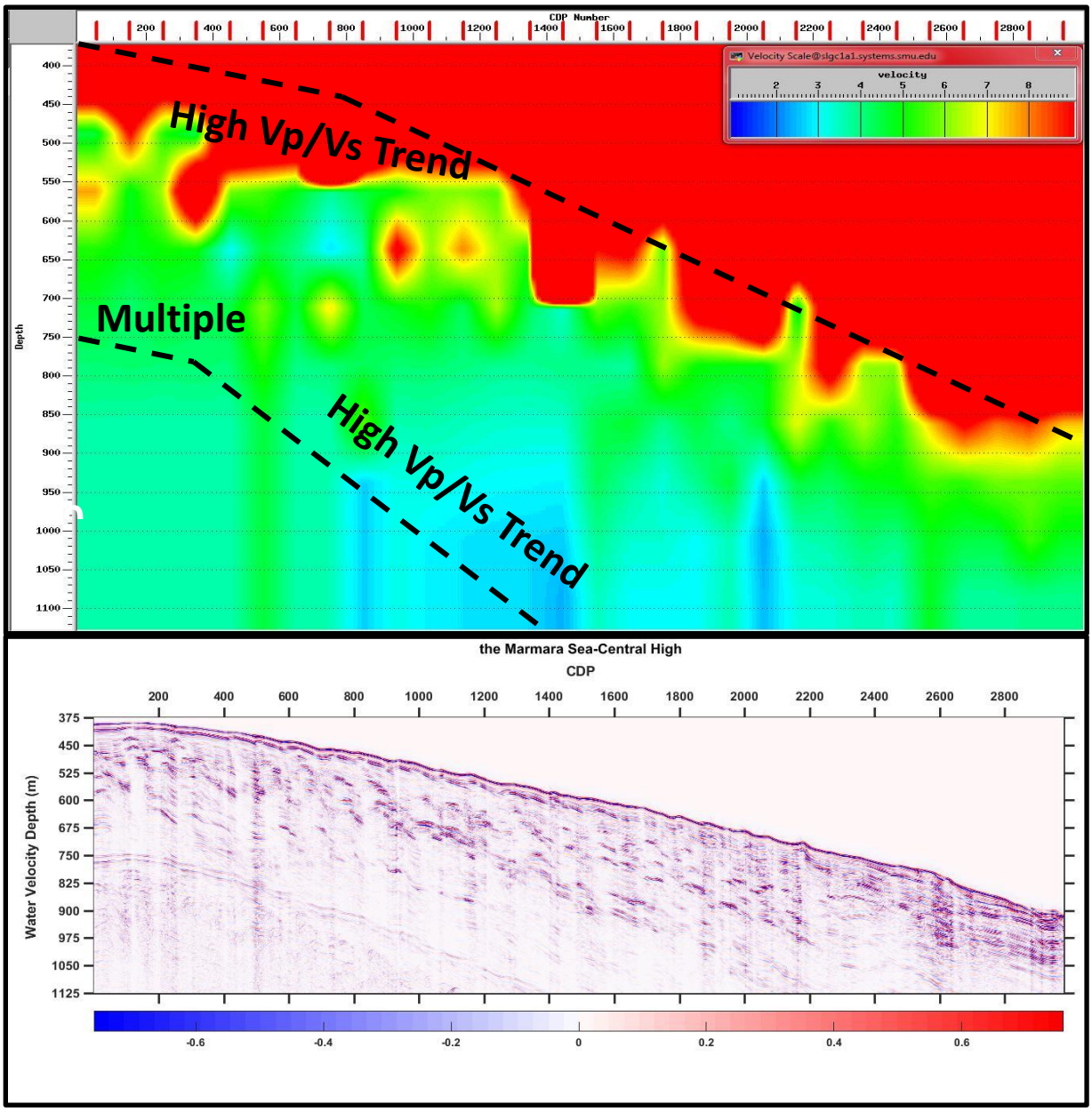

Figure 44 Vp/Vs ratio profile (top) and Marmara-Central High Full Stack Seismic Section (below). The high Vp/Vs ratios (>7) suggested for high pore pressure zones, are generally observed in shallow sediments above 200 meters depth below sea-floor, whereas the low Vp/Vs ratios (<3.5), suggested gas concentrations, and mineralogy changing are observed at deeper levels.

The higher Vp/Vs ratios were observed up to 200 m below seafloor depth where lower Vp/Vs ratios were observed for deeper zones.

The Vp/Vs ratios were significantly higher (>8) for shallow zones where creep like deformations mostly occur (~150 mbsf). These results are consistent with suggested overpressure from Shillington et al. (2012) however these profiles have large uncertainties. To improve this result and to understand the detectability of overpressure I compared these velocity values to Hamilton based expected velocities for typical marine sediments I calculated using my rock physics models.

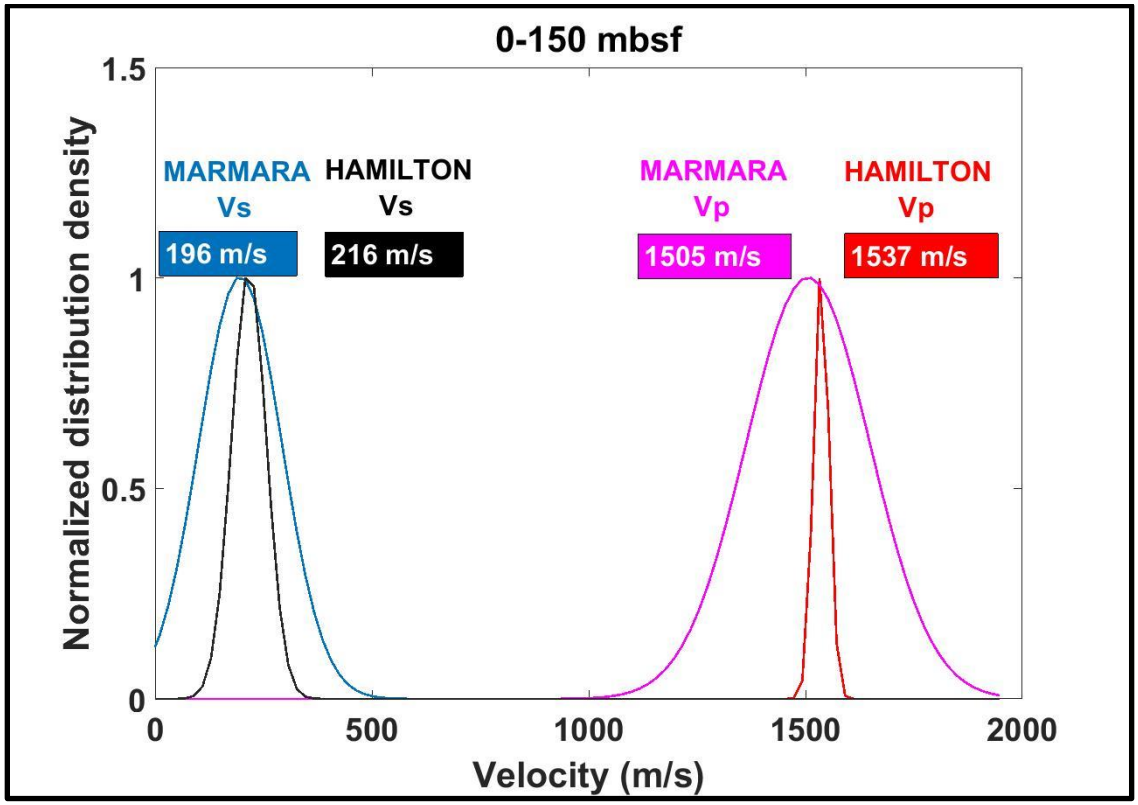

Figure 45 The normal distribution of Vp and Vs for upper 150 m sediments in the Marmara Sea-Central High sediments and expected values in Hamilton like sediments at the same depth.

In these shallow zones upper 150 mbsf, the mean value of S-wave velocities was 5% lower than Hamilton based expected S-wave velocities. The mean value of P-wave velocities was also 3% lower than Hamilton based expected P-wave velocities.

Both empirical calculations and the effective medium models suggest that Vs is lower in the upper sediments until 150 m below sea floor depth. According to the sensitivity model calculations, 50% of observed P-wave velocities and 24% of S-wave velocities were below the 2-standard deviation confidence level of non-overpressure Hamilton based sediments.

Additionally, at greater depths below these shallow zones Vp/Vs ratios approach a value of 3 at further depths, as a result of gas or mineralogy variations from clay to sand. These values were compared with Hamilton like sediments in 150 m-300 m below seafloor depth range.

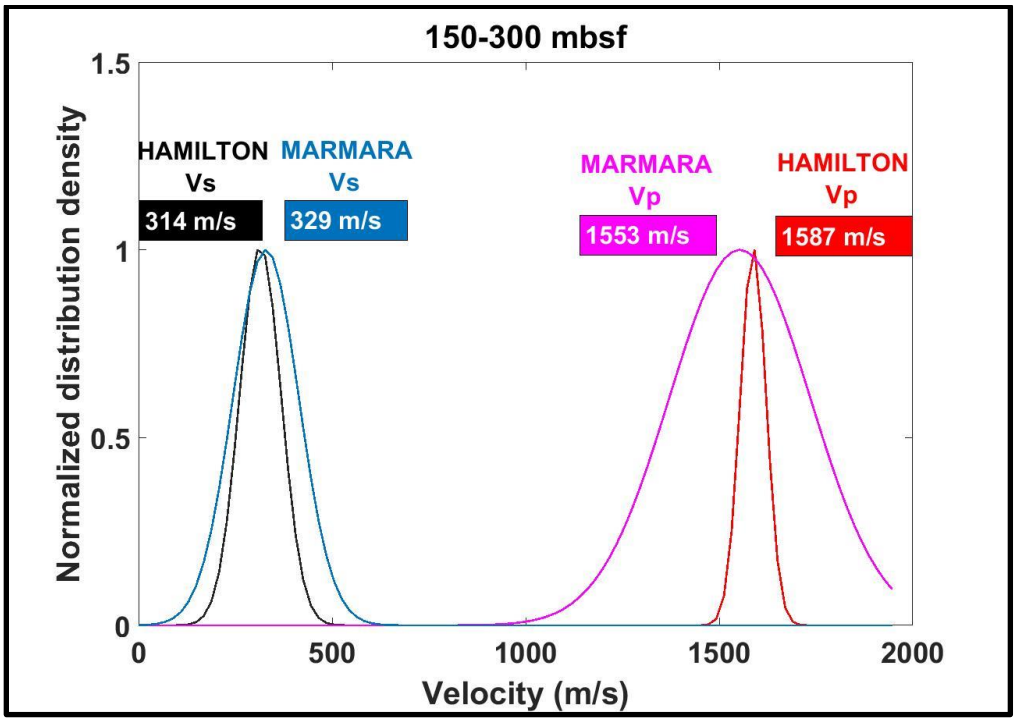

Figure 46 The normal distribution of Vp and Vs for 150-300 m depth range sediments below sea floor in the Marmara Sea-Central High and expected values in Hamilton like sediments at the same depth. Both P-wave and S-wave velocities are lower than expected values in at this depth range.

In this depth range, the mean value of P-wave velocities for the Marmara Sea sediments is 3% lower than Hamilton based expected P-wave velocities. The mean S-wave velocity is almost equal to the Hamilton based expected S-wave velocities. In sensitivity analysis, 42% of observed P-wave velocities were below the 2-standard deviation confidence level of non-overpressure Hamilton based sediments.

I already knew from my rock physics models that these two factors cause low Vp/Vs ratios, however their impacts on seismic velocities were opposite (Figure 23). This helped me to define two low Vp/Vs ratios is that I observed at different CDP locations with different reasons.

For instance, for CDP 800, both P-wave and S-wave velocities increased at 600 m depth, I suggest this low Vp/Vs ratio is caused by mineralogy variations from sand to clay by considering previous stratigraphic interpretations from drill logs and my rock physics model.

For CDP 1400 and CDP 2000 P-wave velocities decrease below 700 m depth and the subjacent layers were observed with lower Vp/Vs ratios (Figure 44). At these zones while P-wave velocities significantly decreases, S-wave velocities are not affected. I suggest this low Vp/Vs ratios are caused by gas.

In order to determine the main reason of this velocity anomalies, I compared Marmara Sea velocities with Blake Ridge velocities, in two different depth ranges, from seafloor to 150 m and from 150 m to 300 m depth.

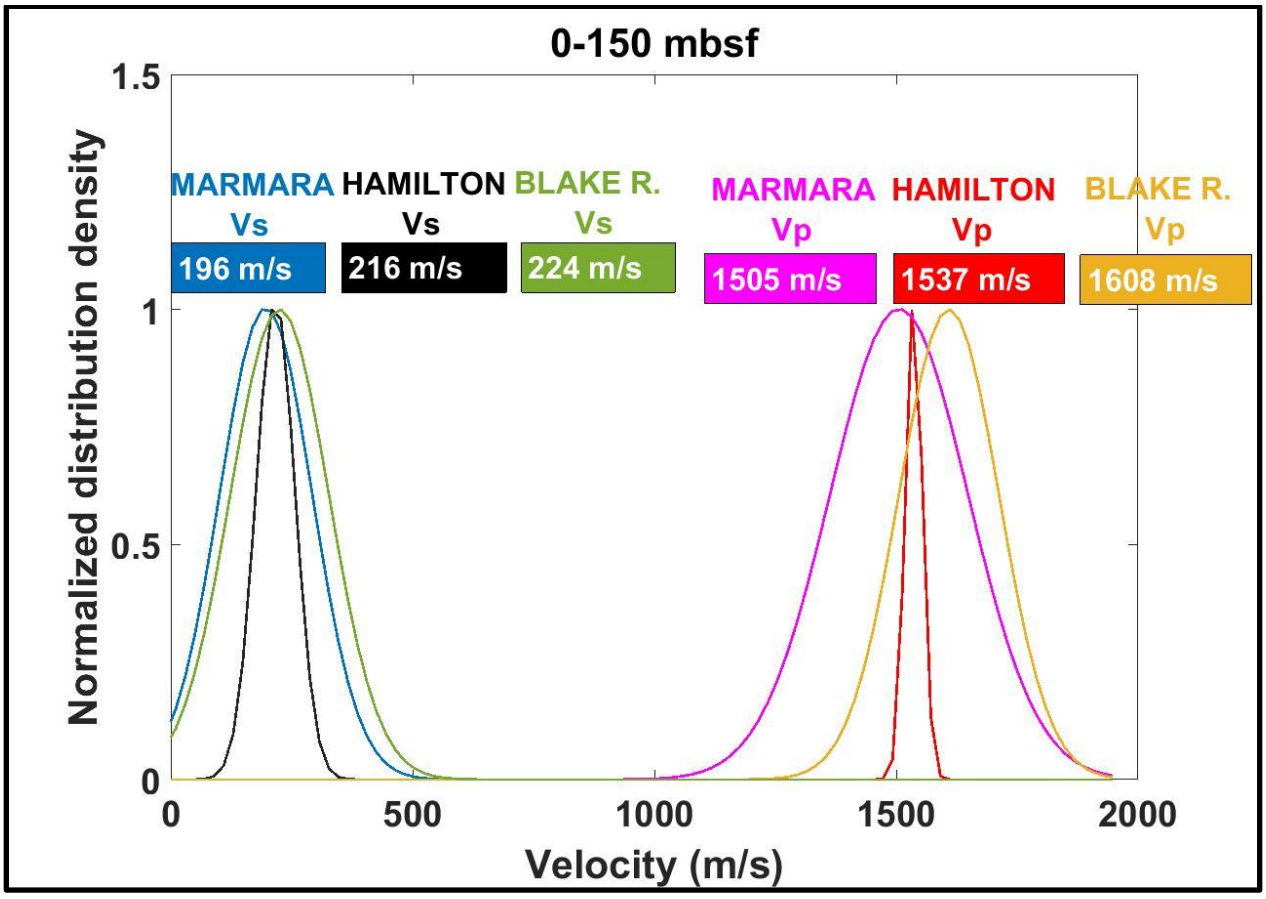

Figure 47 The normal distribution of Vp and Vs for upper 150 m sediments in the Marmara Sea-Central High and Blake Ridge sediments and expected values in Hamilton like sediments at the same depth.

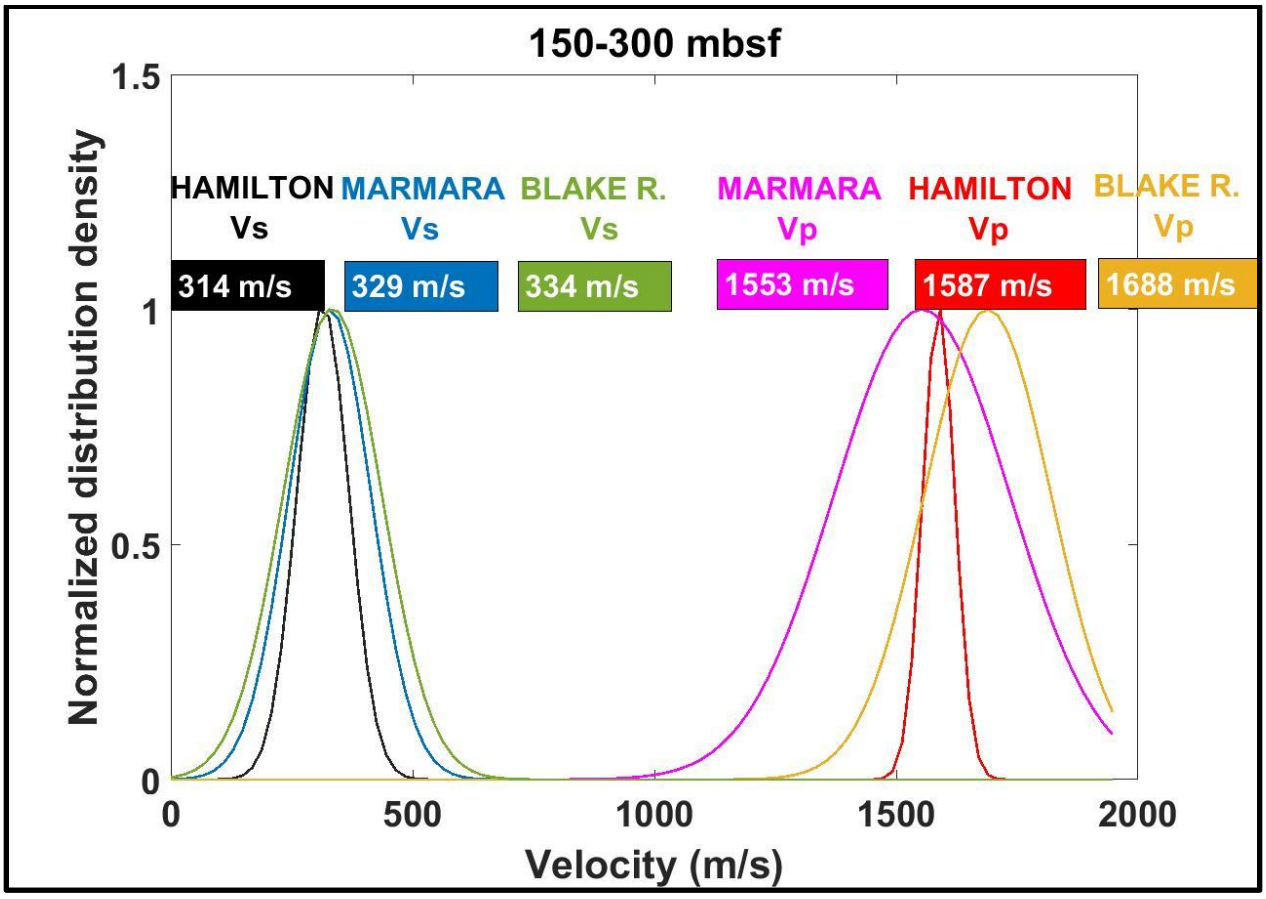

Figure 48 The normal distribution of Vp and Vs for 150-300 m depth range sediments below sea floor in the Marmara Sea-Central High, Blake Ridge sediments and expected values in Hamilton like sediments at the same depth.

In normal distribution analysis, I observed that both Vp and Vs velocities are lower, Vp/Vs ratios are higher for the upper 150 m of sediments in the Marmara Sea compared to Blake Ridge. This provided me with an essential information.

In Central High, S-wave velocities are lower and Vp/Vs ratios were significantly higher (>8) for shallow zones where suggested creep like deformations mostly likely occur (~150 mbsf). However, model based normal distribution sensitivity showed only half of these values are below

the 2-standard deviation confidence level. The known higher sedimentation rate (0.2-0.5 m/kyr), and lower seismic velocity profile compared to Blake Ridge (0.1-0.35 m/kyr) indicates overpressure.

Since I know the sedimentation rate on Central High-the Marmara Sea is higher than Blake Ridge (Cagatay et al., 2017), I conclude that low velocities in shallow zones and suggested creep like deformations are caused by elevated pore fluid pressures, and that pressure is the result of high sedimentation rate in this region.

CONCLUSIONS

This study provided a detailed quantitative geophysical analysis by combining of AVO analysis with rock-physics modeling to detect overpressure and gas. However, there are still higher uncertainties in mineralogy and porosity profiles. Only high pore pressures which approach 90 % of lithostatic pressure can be detectable with given my uncertainties. Accordingly, results are consistent with sedimentation rate. Higher Vp/Vs ratios consistent with high pore pressure where we observed higher sedimentation rate.

The results of this study are open to improvement. The evidences in this study are supporting the overpressure hypothesis from previous studies (Shillington et al., 2012), but not clearly statistically significant. Ultimately, we need higher resolution data (larger offset-more channels) for tighter constraint on velocities. Then, this provides more accurate velocity results represent the study site.

APPENDIX

Methodology: Gas Hydrate and Free Gas Detection

Methane is the most frequently encountered gas in marine sediments, might has thermogenic or biogenic origin. (Tary, 2011) Due to the geothermal gradient below the sea-floor, under low-temperature and high-pressure conditions these methane gas molecules are trapped and stabilized in solid crystalline form by sufficient water molecules as hydrate or gas-hydrate in marine sediments. These gas hydrate accumulation areas under favorable conditions are called Gas Hydrate Stability Zones (GHSZ) and have different rock physics character than other sediment layers above and below GSZH.

Bottom Simulating Reflectors (BSR) form at the bottom of Gas Hydrate Stability Zones (GHSZ). They refer to strong reflections that indicate large amplitude anomalies sourced by the impedance contrast between Gas Hydrate Stability Zones (GHSZ) and subjacent layers. In most areas, these subjacent layers are free gas reservoirs trapped by BSRs. However, Bottom Simulating Reflectors still can be observed at the bottom of the Gas Hydrate Stability Zones without free gas concentration. (Hyndman & Spence, 1992)

Gas hydrates show different rock physics properties in relation to where they concentrate in rock and their amount. These accumulations are principally observed either as gas hydrates filling the pore space, or as gas hydrates loading solid frame. (e.g. Helgerud et al., 1999) Both these scenarios differ in their seismic wave velocities and cause different AVO responses.

Where gas hydrates are considered as a part of the pore space, it is also assumed that they become concentration in pore space (S_h) ,as calculated by Reuss (1929) formula considering average of water and gas hydrate bulk moduli (e.g. Helgerud et al., 1999)

$$S_h = C_h/\varphi \tag{27}$$

$$newK_f = [\frac{S_h}{K_h} + \frac{1 - S_h}{K_f}]^{-1} \tag{28}$$

where (C_h) volumetric concentration of gas hydrate in the rock, (K_h) is the bulk modulus of gas hydrates and (K_f) is the bulk modulus of water.

Where gas hydrates are considered as a part of the solid frame of rock, they reduce the original porosity(φ), and affect solid frame elastic parameters. The bulk modulus of pore fluid $(newK_f)$ will be dependent only on water concentration or porosity (φ) (e.g. Helgerud et al., 1999)

$$new\varphi = \varphi - C_h \tag{29}$$

where $(new\varphi)$ is the reduced porosity, (C_h) volumetric concentration of gas hydrate in the rock,

We created six different scenarios to calculate AVO responses assuming both at the top of Gas Hydrate Stability Zone consider gas hydrate concentration either in pore space or in solid frame of rock varies from 1% to 10% and at Bottom Simulating Reflector above sediments either 0.5% or

3.0% free-gas filling the pore space. All scenarios assume in mud-rich sediment lithology with 50% porosity. Seismic velocities (Vp,Vs) and densities are derived by using effective medium model, which are equations by Dvorkin et al. (1999), Hertz-Mindlin (1949) and Gassmann (1951) to estimate bulk & shear moduli of saturated clay-rich sediments. Then, AVO responses are (calculated) based on Shuey AVO Approximation. (Shuey, 1985). For mud rich sediment lithology with 50% porosity neither has gas-hydrates or free-gas concentration; The P-wave and S-wave velocities of the sediment were derived as 1636.5 m/s and 331.4 m/s; density was 1806 kg/m^3.

$$R(\theta) \cong R_0 + \left(A_0 + R_0 + \frac{\Delta\sigma}{1-\sigma^2}\right) sin^2\theta_I + \frac{1}{2}\frac{\Delta\alpha}{\alpha}(tan^2\theta_I - sin^2\theta_I)$$

where R_o is the normal incidence reflection coefficient, and σ is Poisson's Ratio

$$\sigma = \frac{1}{2}(\sigma_2 - \sigma_1)$$

$$\Delta\sigma = \sigma_2 - \sigma_1$$

$$R_0 = \frac{1}{2}\left(\frac{\Delta\alpha}{\alpha} + \frac{\Delta\rho}{\rho}\right)$$

$$A_0 = \frac{\frac{\Delta\alpha}{\alpha}}{\frac{\Delta\alpha}{\alpha} + \frac{\Delta\rho}{\rho}} - 2\left(1 + \frac{\frac{\Delta\alpha}{\alpha}}{\frac{\Delta\alpha}{\alpha} + \frac{\Delta\rho}{\rho}}\right)\frac{1-2\sigma}{1-\sigma}$$

Table 10 Shuey AVO Approximation (Shuey, 1985)

Scenario 1: 0%-10% Hydrate Concentration filling pore space in Gas Hydrate Stability Zone (GHSZ) in Mud-Rich Sediment Lithology with 50% porosity

In the first scenario, gas hydrate concentration changes from 0% to 10%, assumed present within the pore space in Gas Hydrate Stability Zone in mud-rich sediment lithology with 50% porosity. AVO responses at the top of Gas Hydrate Stability Zone are calculated.

With increased gas hydrate concentration filling pore space, P-wave velocity increases by 3.0%, while S-wave velocity decreases by 1% which can be considered negligible. Since gas hydrates filling pore space, they behave as a component of pore fluid, shear modulus of solid frame (e.g. Helgerud et al., 1999) and S-waves are unaffected; only bulk modulus changes.

Scenario 1	P-wave (m/s)	S-wave (m/s)	Density (kg/m^3)
Mud-Rich Sediments	1636.5	331.4	1806.0
Gas Hydrates (0%-10%) in Pore Space	1636.5 -- 1687.2	331.0 -- 327.9	1806.0 -- 1844.4

Table 11 Seismic velocity and density results for Scenario 1

Scenario 2: 0%-10% Hydrate Concentration as a part of solid frame of rock in Gas Hydrate Stability Zone (GHSZ) in Mud-Rich Sediment Lithology with 50% porosity

In the second scenario, gas hydrate concentration changes from 0% to 10%, assumed present as a part of solid frame of rock in Gas Hydrate Stability Zone in mud-rich sediment lithology with 50% porosity. AVO responses at the top of Gas Hydrate Stability Zone are calculated.

As a result of the gas hydrate accumulation in solid frame of rock and increased bulk and shear moduli of solid frame, both P-wave and S-wave velocities increases by 8% and 11%, respectively.

Scenario 2	P-wave (m/s)	S-wave (m/s)	Density (kg/m^3)
Mud-Rich Sediments	1636.5	331.4	1806.0
Gas Hydrates (0%-10%) in Load Frame	1636.5 -- 1771.2	331.4 – 368.2	1806.0 -- 1756.8

Table 12 Seismic velocity and density results for – Scenario 2

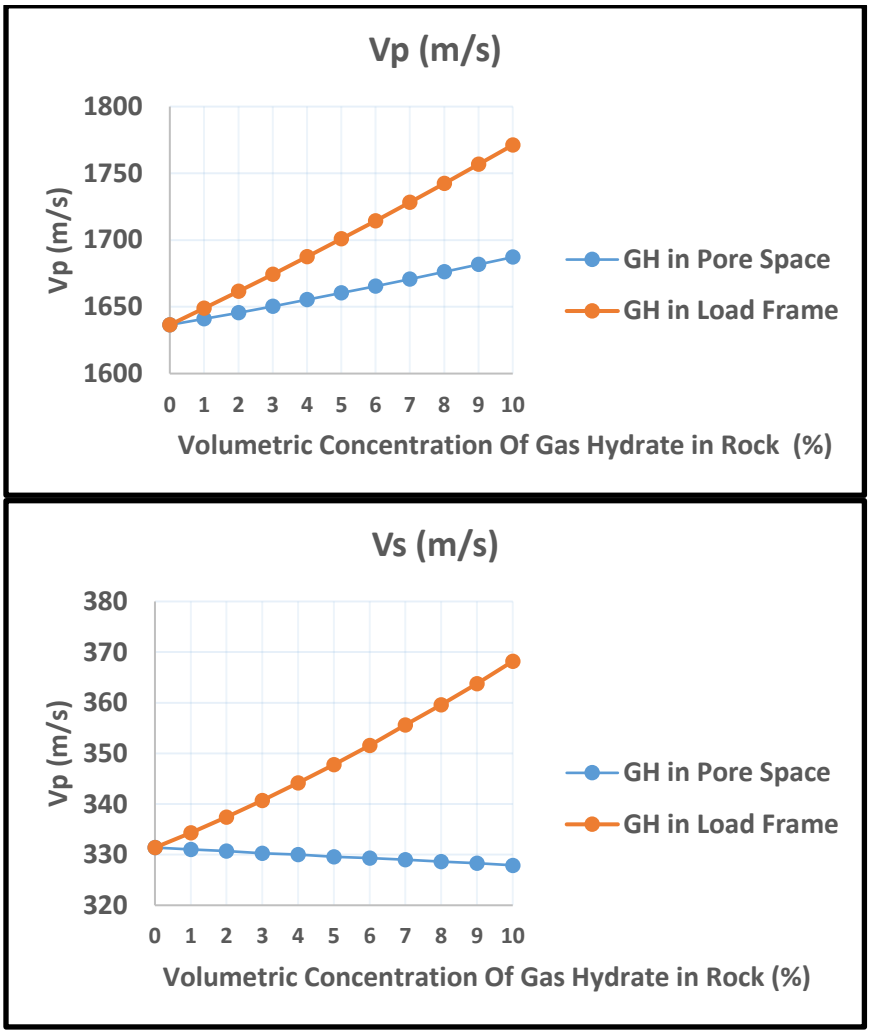

Figure 49 P-wave and S-wave velocity profiles for Gas hydrate concentration filling Pore Space vs. as a part of solid frame of rock in Mud-Rich Sediment Lithology with 50% porosity. P-wave velocity increases with increased gas hydrate concentration during both scenarios while S-wave shows decreasing gradient. Gas hydrates filling pore space does not have any effect on solid frame and solid frame shear modulus.

This difference in P-wave and S-wave velocities during the first and the second scenarios relates to solid shear modulus. It also appears in both Vp/Vs and Poisson's ratio as opposite gradients with different slopes.

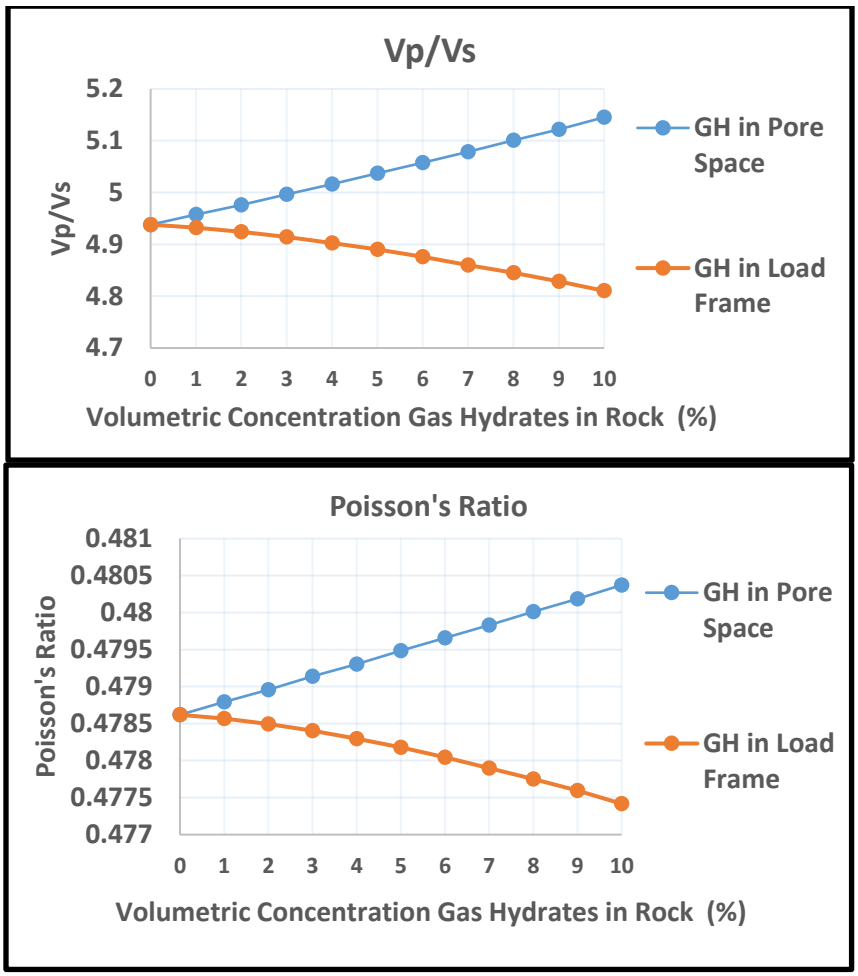

Figure 50 Vp/Vs ratio and Poisson's Ratio profiles for Gas Hydrate in Pore Space vs. Load Frame in Mud-Rich Sediment Lithology has 50% porosity. Different accumulate locations in rock changing from pore space to load frame for gas hydrates cause different gradients.

Both scenarios have positive reflection coefficients that increased with volumetric concentration of gas hydrates in rock. Gas hydrates in pore space lithology shows a small

amplitude increase with offset while gas hydrates in load frame lithology shows larger amplitude increase with offset. Event for 10% gas hydrates in load frame causes 30% bigger amplitudes at far offset (30 degree) than zero offset (0 degree), while this increase is 15% for gas hydrates in pore space.

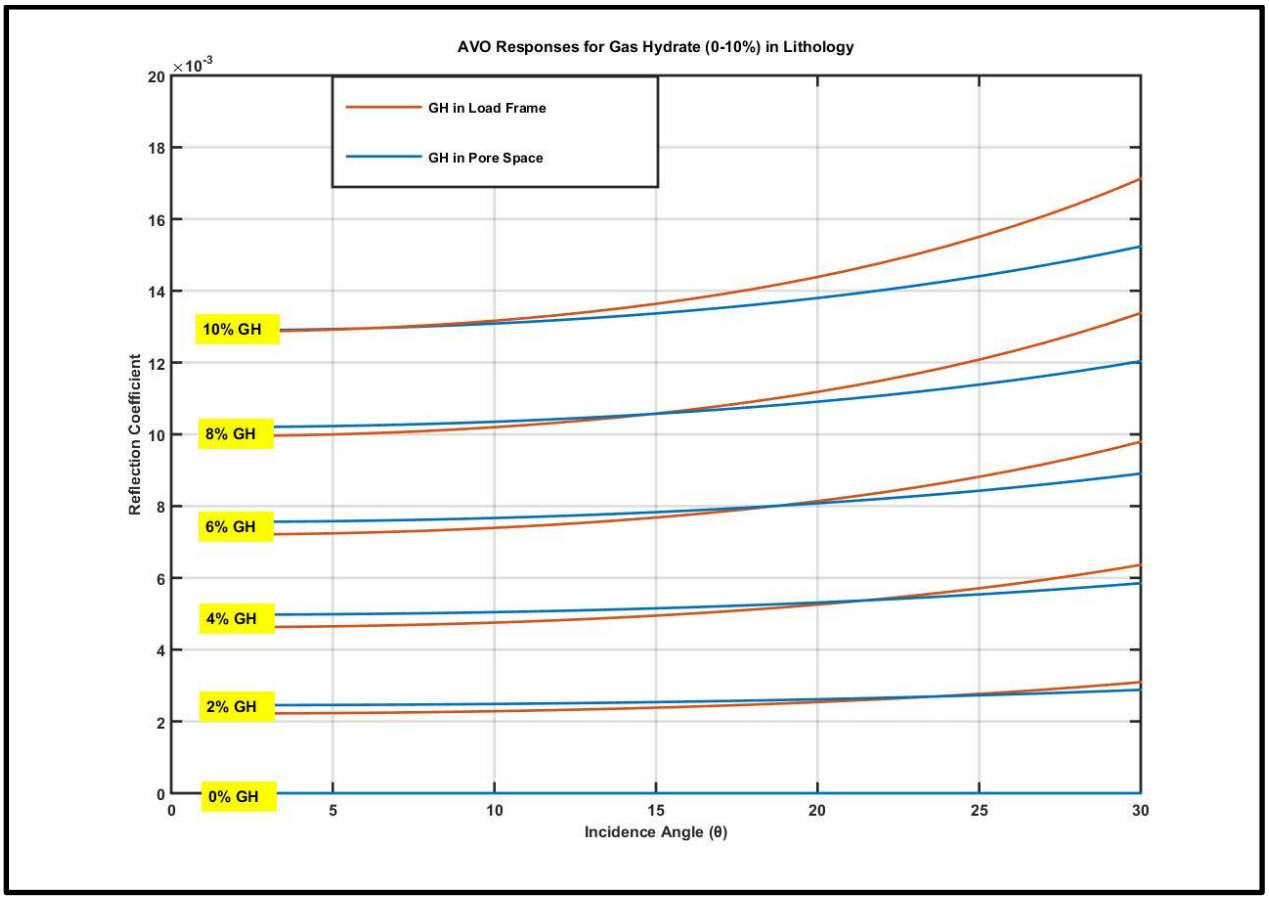

Figure 51 AVO responses at the top of Gas Hydrate Stability Zone due to changing gas hydrate concentration from pore space to solid frame (in pore space - blue lines vs. in load frame - orange lines) with increased amount (0% GH-10% GH) in Mud-Rich Sediment lithology with 50% porosity. Reflection coefficients have building up at zero offset and increase through offset with increased amount of gas hydrate both in pore space and solid frame. Note that, AVO response events for gas hydrate concentration, two scenarios start to differentiate from each other with different slope values through far offset as a result of increased gas hydrate concentration.

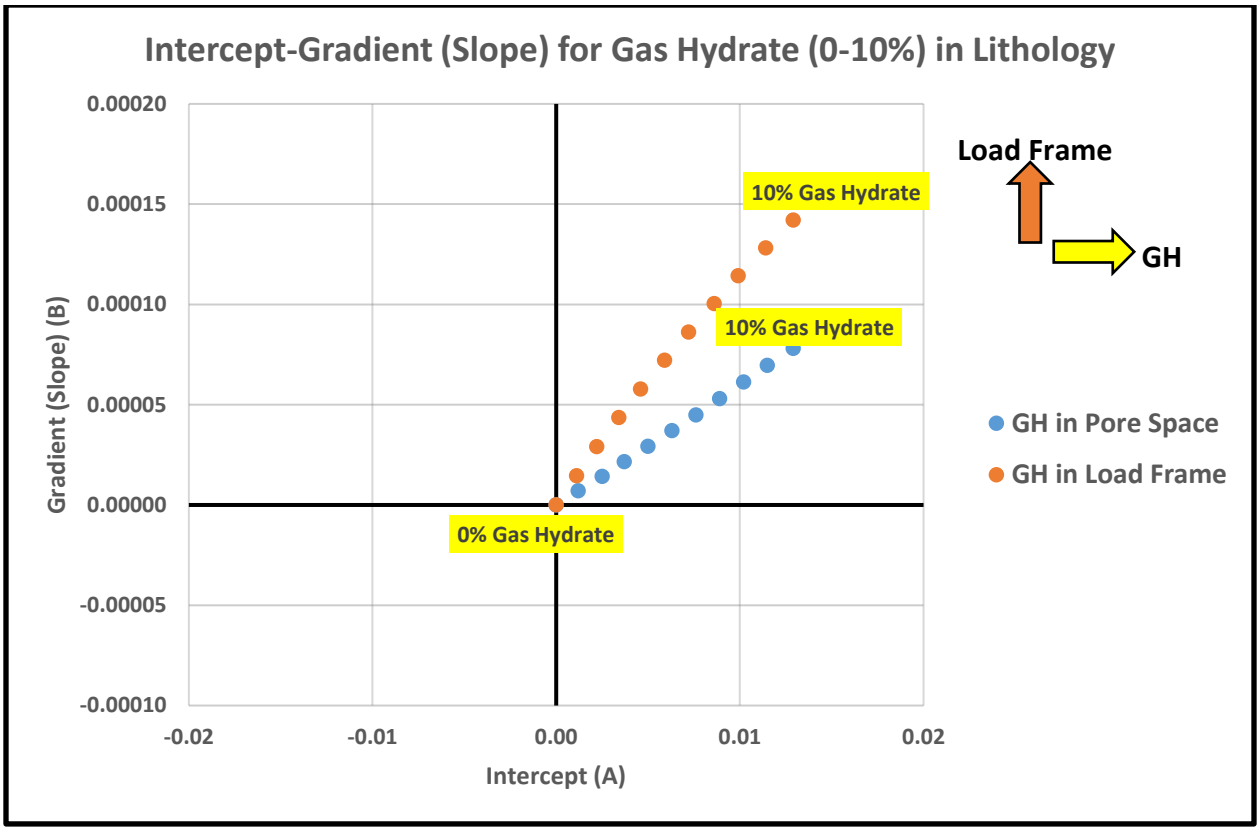

Figure 52 Intercept-Gradient (Slope) for Gas Hydrates (0%-10% GH) in Mud-Rich Sediment Lithology with 50% porosity. For both scenarios, positive intercept and gradient (slope) values are observed.

Scenario 3: The Bottom Simulating Reflector (BSR) below 0%-10% Hydrate Concentration filling pore space in Gas Hydrate Stability Zone (GHSZ) above sediments 0.5% free-gas filling pore space in Mud-Rich Sediment Lithology with 50% porosity

In the third scenario, Bottom Simulating Reflector assumed wedged between gas hydrate concentration changes from 0% to 10% present within the pore space in Gas Hydrate Stability Zone, and sediments 0.5% free-gas filling pore space in mud rich sediment lithology with 50% porosity. AVO responses at Bottom Simulating Reflector (BSR) are calculated.

The 0.5% free-gas pore filled sediments underneath 10% gas hydrate concentration in pore space causes 11% decrease in P-wave velocity at BSR Since we know from our initial methods,

P-wave is highly sensitive to free-gas existence, even 0.5% free-gas amount below BSR is able to dominate AVO responses negatively by dropping P-wave velocity from Gas Hydrate Stability Zone through free gas filling pore space sediments. This effect also be observed in their AVO responses with negative intercept and gradient (slope). S-wave velocity increases 1% to (331.4 m/s) assume mud rich sediment lithology has 50% porosity has neither gas hydrate nor free-gas. This reveals as either gas hydrates in pore space or free gas below BSR has no effect on S-wave velocity.

Scenario 3	P-wave (m/s)	S-wave (m/s)	Density (kg/m^3)
Gas Hydrates (0%-10%) in Pore Space	1636.5 -- 1687.2	331.0 -- 327.9	1806.0 -- 1844.4
0.5% Free Gas in Mud Rich Sed.	1512	332.0	1801.0

Table 13 Seismic velocity and density results for– Scenario 3

Scenario 4: Bottom Simulating Reflector (BSR) below 0%-10% Hydrate Concentration as a part of solid frame of rock in Gas Hydrate Stability Zone (GHSZ) above sediments 0.5% free-gas filling pore space in Mud-Rich Sediment Lithology with 50% porosity

In the fourth scenario, Bottom Simulating Reflector assumed wedged between gas hydrate concentration changes from 0% to 10% present as a part of solid frame in Gas Hydrate Stability Zone, and sediments 0.5% free-gas filling pore space in mud rich sediment lithology with 50% porosity. AVO responses at the Bottom Simulating Reflector (BSR) are calculated.

The 0.5% free-gas concentration filling pore space of sediments underneath 10% gas-hydrate concentration as a part of solid frame of rock in Gas Hydrate Stability Zone causes 17% decrease in P-wave velocity at BSR. For S-wave velocity, we observe a decreasing gradient at BSR as a result sediments with free-gas. While S-waves increases with stiffness caused by gas hydrates in solid frame, with an absence of gas hydrates below BSR S-wave returns to 331.4 m/s assumes mud rich sediment lithology with 50% porosity neither has gas hydrates or free-gas. Even though there is 0.5% free gas below BSR, this has no effect on S-wave velocity.

Scenario 4	P-wave (m/s)	S-wave (m/s)	Density (kg/m^3)
Gas Hydrates (0%-10%) in Load Frame	1636.5 -- 1771.2	331.4 – 368.2	1806.0 -- 1756.8
0.5% Free Gas in Mud Rich Sed.	1512	332.0	1801.0

Table 14 Seismic velocity and density results for– Scenario 4

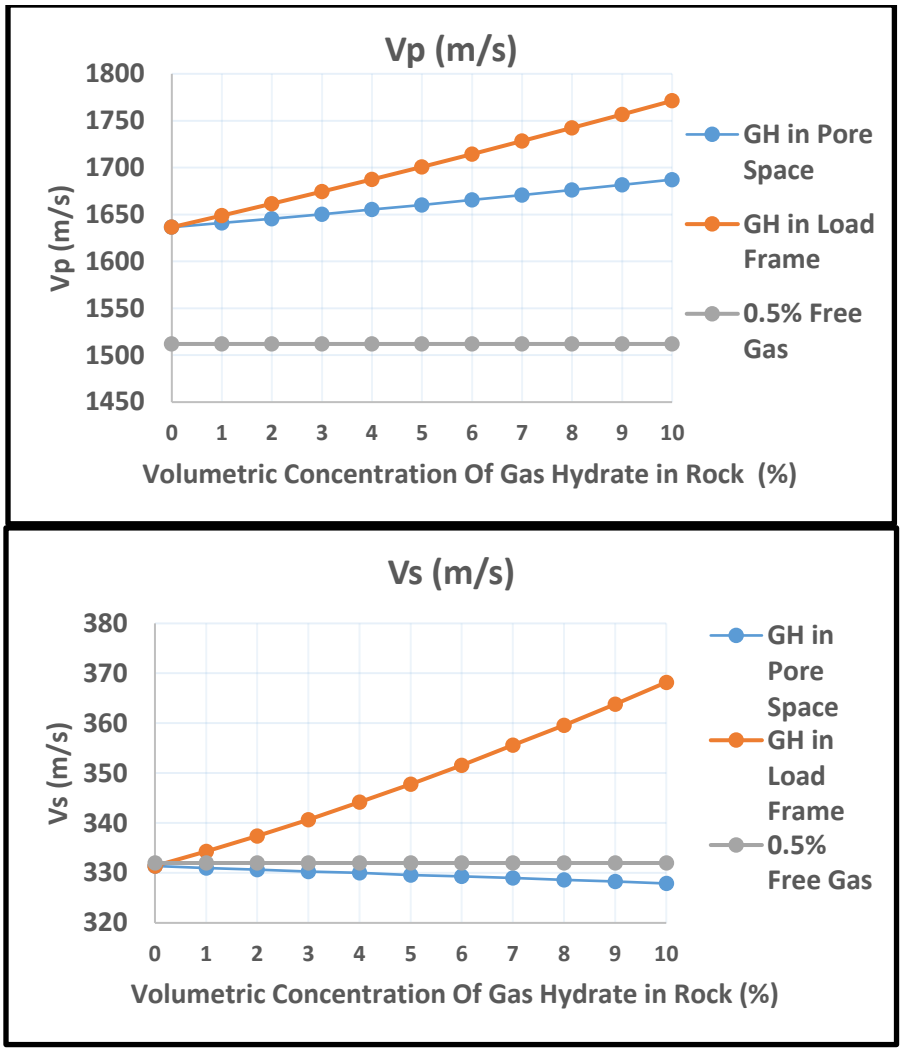

Figure 53 P-wave and S-wave velocity profiles at Bottom Simulating Reflector (BSR) between Gas Hydrate Stability Zone (GHSZ) above 0.5% Free-Gas filling pore space in Mud-Rich Sediment Lithology has 50% porosity. P-wave velocity decreases with an increased gas hydrates either in pore space or in solid frame while S-wave velocity shows a decreasing gradient for only a case of gas-hydrates in load frame. It returns to initial velocity assumes mud rich sediment lithology neither has gas hydrates or free gas. Event for BSR above free-gas filling pore space and below gas hydrates in pore space, S-wave velocity is not affected by free-gas deposits.

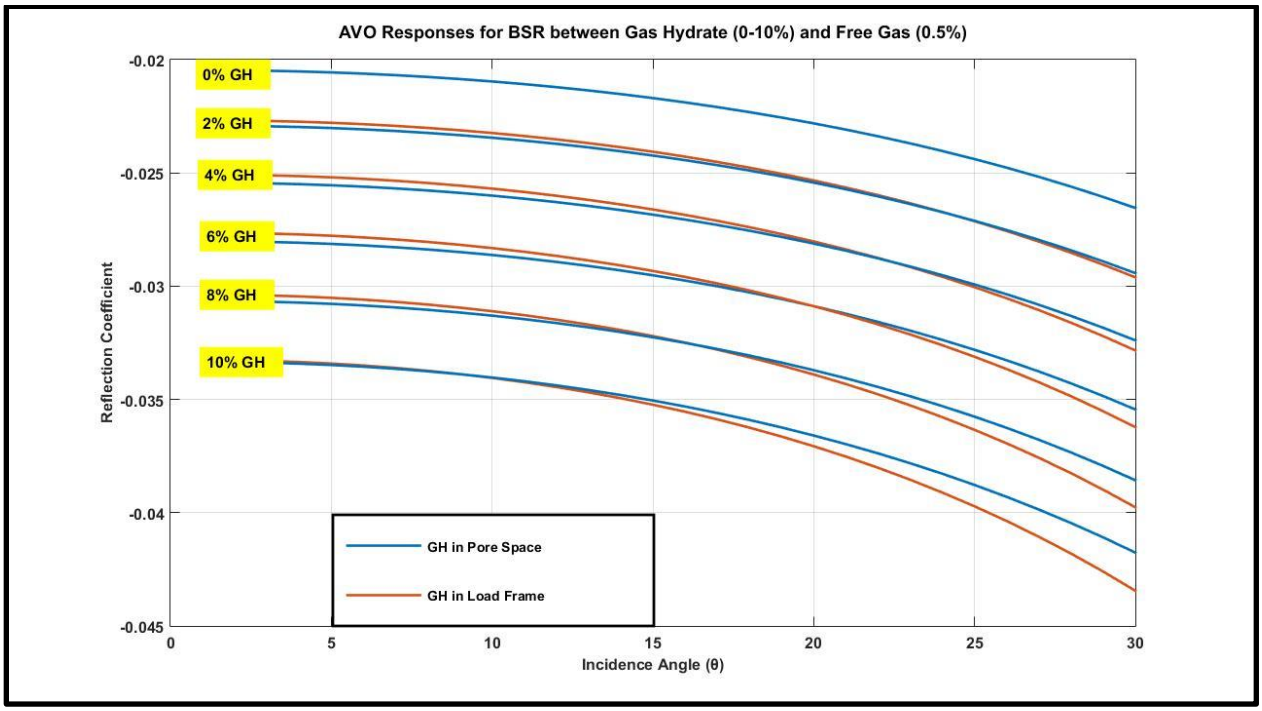

Figure 54 AVO responses due to the BSR underneath gas hydrate concentration changing from pore space to solid frame (in pore space - blue lines vs. in load frame - orange lines) with increased amount (0% GH-10% GH) of gas hydrates above 0.5% free-gas in Mud-Rich Sediment lithology has 50% porosity. Reflection coefficients (Amplitudes) builds up at zero offset and increase negatively through far offset with increased amount of gas hydrates either in pore space or in solid frame.

Scenario 5: Bottom Simulating Reflector (BSR) below 0%-10% Hydrate Concentration filling pore space in Gas Hydrate Stability Zone (GHSZ) above sediments 3.0% free-gas filling pore space in a Mud-Rich Sediment Lithology with 50% porosity

In the fifth scenario, Bottom Simulating Reflector assumed wedged between gas hydrate concentration changes from 0% to 10% present within the pore space in Gas Hydrate Stability Zone, and sediments 3.0% free-gas filling pore space in mud rich sediment lithology with 50% porosity. AVO responses at Bottom Simulating Reflector (BSR) are calculated.

Increasing free gas amount to 3.0% below BSR causes 21% decreasing in P-wave velocity while S-wave velocity is not affected. This decreasing is larger than the third scenario which

assumes 0.5% free-gas filling pore space below BSR and it also reveals P-wave velocity is significant for free gas existence.

Scenario 5	P-wave (m/s)	S-wave (m/s)	Density (kg/m^3)
Gas Hydrates (0%-10%) in Pore Space	1636.5 -- 1687.2	331.0 -- 327.9	1806.0 -- 1844.4
3.0% Free Gas in Mud Rich Sed.	1338.0	333.0	1793.0

Table 15 Seismic velocity and density results for– Scenario 5

Scenario 6: The Bottom Simulating Reflector (BSR) below 0%-10% Hydrate Concentration as a part of solid frame of rock in Gas Hydrate Stability Zone (GHSZ) above sediments 3.0% free-gas filling pore space in a Mud-Rich Sediment Lithology with 50% porosity

In the sixth scenario, Bottom Simulating Reflector assumed wedged between gas hydrate concentration changes from 0% to 10% present as a part of solid frame in Gas Hydrate Stability Zone, and sediments 3.0% free-gas filling pore space in mud rich sediment lithology with 50% porosity. AVO responses at Bottom Simulating Reflector (BSR) are calculated.

As we expected, increasing the free-gas amount to 3% below BSR causes 25% decreasing in P-wave velocity as larger than the fourth scenario assumes 0.5% free-gas in solid rock frame of sediments below the BSR. With an absence of gas hydrates below BSR S-wave returns to the velocity assumes mud rich sediment lithology with 50% porosity neither has gas hydrates or free-gas. Even though there is 3.0% free gas below BSR, this has no effect on S-wave velocity.

Scenario 6	P-wave (m/s)	S-wave (m/s)	Density (kg/m^3)
Gas Hydrates (0%-10%) in Load Frame	1636.5 -- 1771.2	331.4 – 368.2	1806.0 -- 1756.8
3.0% Free Gas in Mud Rich Sed.	1338.0	333.0	1793.0

Table 16 Seismic velocity and density results for– Scenario 6

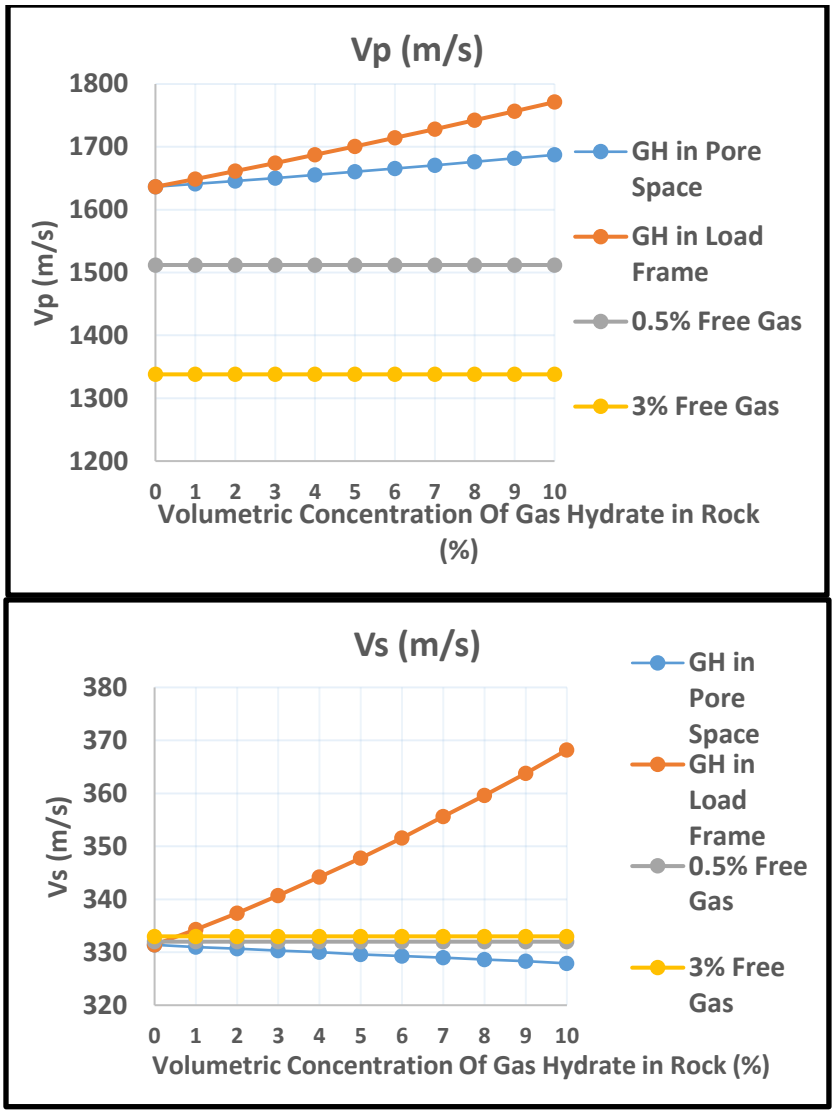

Figure 55 P-wave and S-wave velocity profiles at Bottom Simulating Reflector (BSR) below Gas Hydrates (GH) either in pore space filling or in solid rock frame above sediments 3.0% free-gas filling pore space in a Mud-Rich Sediment Lithology with 50% porosity. P-wave velocity decreases significantly such as 21% and 25% for both scenarios with increased free gas amount below BSR. S-wave velocity shows only increasing in Gas Hydrate stability zone free-gas below BSR. Event for a BSR with free-gas deposits underneath gas hydrates, S-wave velocities returns to the to the approximately initial S-wave velocity (331.4 m/s) assumes mud rich sediment lithology has 50% porosity has either no gas hydrates or free-gas as a result of no free-gas effect on S-waves.

Increased free gas amount underneath BSR causes increased slope and gradient negatively and pulls AVO responses through negative direction with approximately 2 times (~x2) bigger intercept and gradient (slope) values.

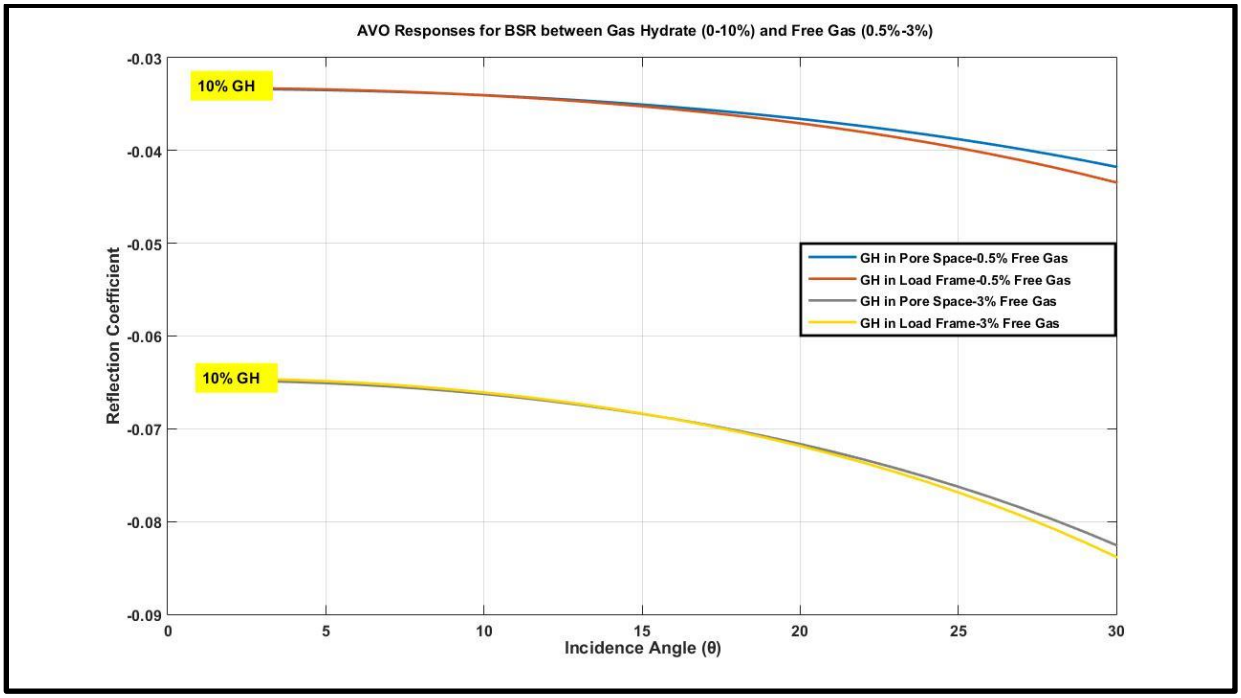

Figure 56 AVO responses due to the BSR underneath 10% gas hydrates (GH) either in pore space or in load frame above sediments has 0.5% and 3.0% free-gas. In Mud-Rich Sediment lithology with 50% porosity. Event for increase of free-gas in mud rich sediment lithology underneath gas hydrates, BSR reflection coefficients (amplitudes) also builds up negatively approximately 2 times (~2x) bigger than assuming 0.5% free-gas deposits. That shows, AVO responses at BSR are more sensible to changing amount of free-gas underneath gas hydrates than changing amount of gas hydrate concentration.

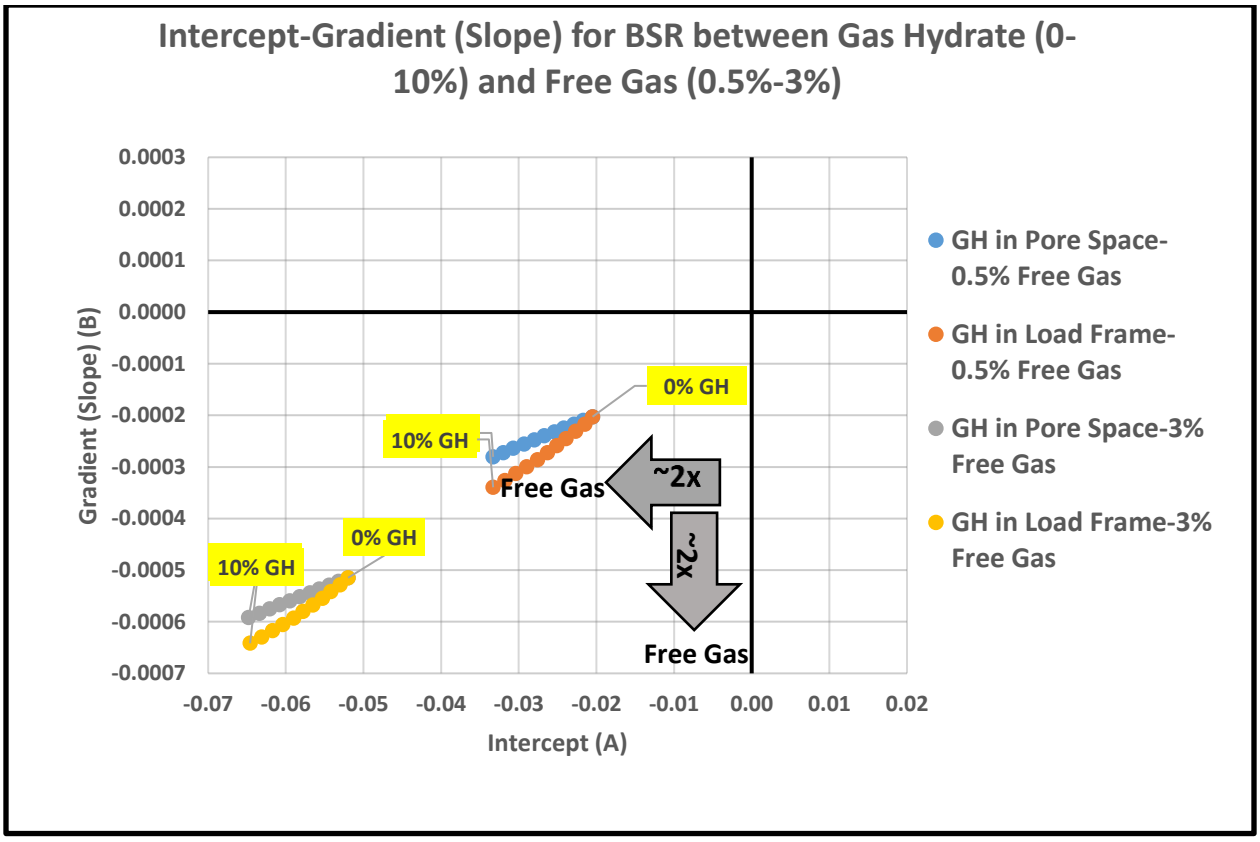

Figure 57 Intercept-Gradient (Slope) 10% gas hydrates (GH) either in pore space or in load frame above sediments has 0.5% and 3.0% free-gas. 0.5% and 3% Free-Gas in sediments in Mud-Rich Sediment lithology has 50% porosity. Since free-gas surpasses gas hydrate, increasing of free-gas from 0.5% to 3.0% in sediments below BSR causes larger AVO anomalies with 2 times (~2x) bigger gradient (slope) and intercept values.

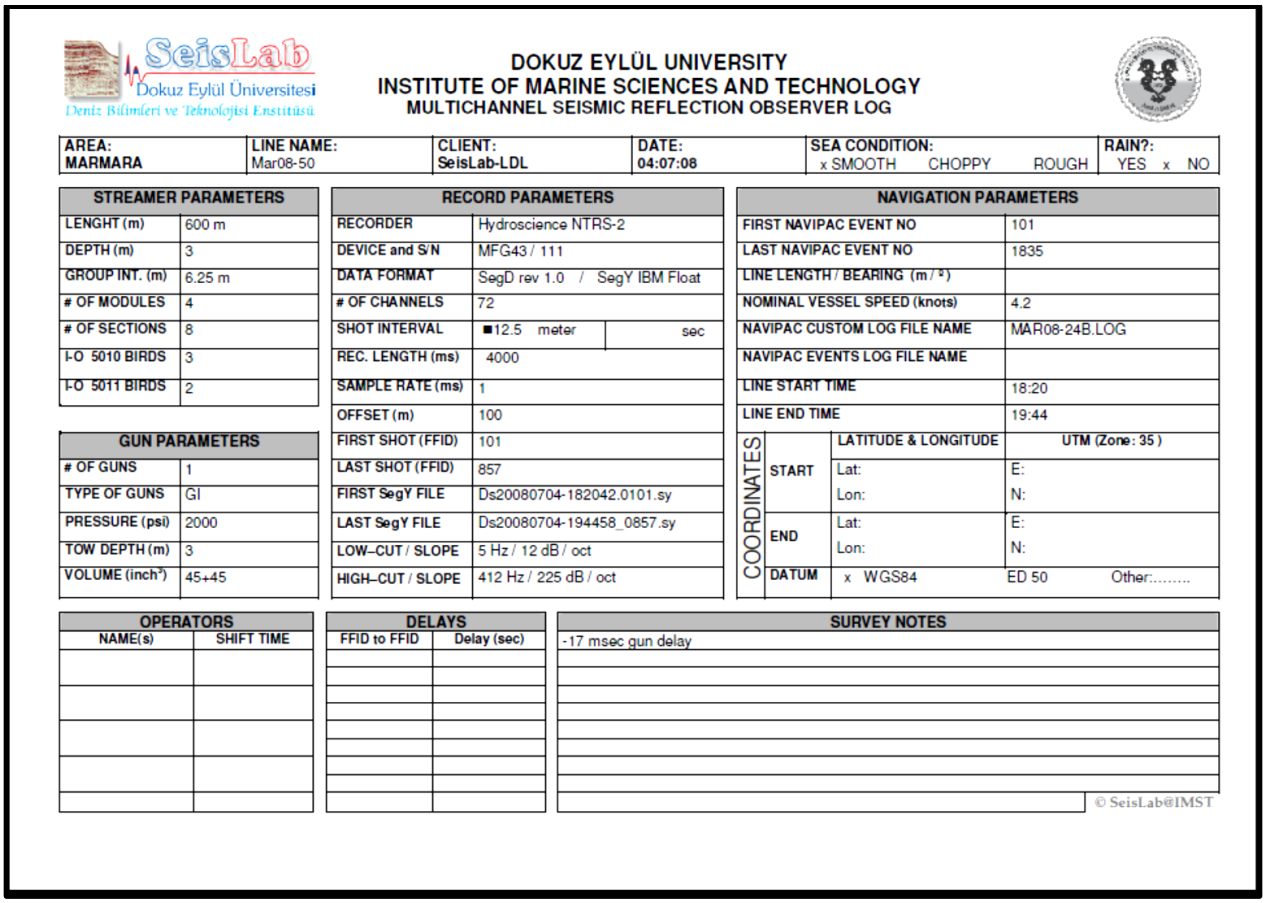

DOKUZ EYLÜL UNIVERSITY
INSTITUTE OF MARINE SCIENCES AND TECHNOLOGY
MULTICHANNEL SEISMIC REFLECTION OBSERVER LOG

AREA:	LINE NAME:	CLIENT:	DATE:	SEA CONDITION:	RAIN?:
MARMARA	Mar08-50	SeisLab-LDL	04:07:08	x SMOOTH CHOPPY ROUGH	YES x NO

STREAMER PARAMETERS	
LENGHT (m)	600 m
DEPTH (m)	3
GROUP INT. (m)	6.25 m
# OF MODULES	4
# OF SECTIONS	8
I-O 5010 BIRDS	3
I-O 5011 BIRDS	2

GUN PARAMETERS	
# OF GUNS	1
TYPE OF GUNS	GI
PRESSURE (psi)	2000
TOW DEPTH (m)	3
VOLUME (inch³)	45+45

RECORD PARAMETERS		
RECORDER	Hydroscience NTRS-2	
DEVICE and S/N	MFG43 / 111	
DATA FORMAT	SegD rev 1.0 / SegY IBM Float	
# OF CHANNELS	72	
SHOT INTERVAL	■12.5 meter	sec
REC. LENGTH (ms)	4000	
SAMPLE RATE (ms)	1	
OFFSET (m)	100	
FIRST SHOT (FFID)	101	
LAST SHOT (FFID)	857	
FIRST SegY FILE	Ds20080704-182042.0101.sy	
LAST SegY FILE	Ds20080704-194458_0857.sy	
LOW-CUT / SLOPE	5 Hz / 12 dB / oct	
HIGH-CUT / SLOPE	412 Hz / 225 dB / oct	

NAVIGATION PARAMETERS			
FIRST NAVIPAC EVENT NO	101		
LAST NAVIPAC EVENT NO	1835		
LINE LENGTH / BEARING (m / °)			
NOMINAL VESSEL SPEED (knots)	4.2		
NAVIPAC CUSTOM LOG FILE NAME	MAR08-24B.LOG		
NAVIPAC EVENTS LOG FILE NAME			
LINE START TIME	18:20		
LINE END TIME	19:44		
COORDINATES		LATITUDE & LONGITUDE	UTM (Zone: 35)
	START	Lat:	E:
		Lon:	N:
	END	Lat:	E:
		Lon:	N:
	DATUM	x WGS84	ED 50 Other:.....

OPERATORS	
NAME(s)	SHIFT TIME

DELAYS	
FFID to FFID	Delay (sec)

SURVEY NOTES
-17 msec gun delay

Figure 58 Cruise Report-Mar08-50

REFERENCES

Aksoy, A. (1997). Active Tectonics of Northwestern Anatolia: The Marmara Poly-Project: a Multidisciplinary Approach by Space-geodesy, Geology, Hydrogeology, Geothermics and Seismology. C. Schindler, & M. Pfister (Eds.). vdf Hochschulverlag AG.

Altinok, Y., Ersoy, S., Yalciner, A. C., Alpar, B., & Kuran, U. (2001, August). Historical tsunamis in the Sea of Marmara. In *International Tsunami Symposium ITS* (pp. 4-2).

Armijo, R., Pondard, N., Meyer, B., Uçarkus, G., De Lépinay, B. M., Malavieille, J. , ... & Sarikavak, K. (2005). Submarine fault scarps in the Sea of Marmara pull-apart (North Anatolian Fault): Implications for seismic hazard in Istanbul. Geochemistry, Geophysics, Geosystems, 6(6).

Barka, A., The North Anatolian fault zone, *Ann. Tectonicae*, 6, Suppl, 164–195, 1992.

Bayrakci, G., Scalabrin, C., Dupré, S., Leblond, I., Tary, J. B., Lanteri, N., ... & Tsabaris, C. (2014). Acoustic monitoring of gas emissions from the seafloor. Part II: a case study from the Sea of Marmara. *Marine Geophysical Research*, *35*(3), 211-229.

Bécel, A., Laigle, M., De Voogd, B., Hirn, A., Taymaz, T., Yolsal-Cevikbilen, S., & Shimamura, H. (2010). North Marmara Trough architecture of basin infill, basement and faults, from PSDM reflection and OBS refraction seismics. Tectonophysics, 490(1), 1-14.

Bourry, C., Chazallon, B., Charlou, J. L., Donval, J. P., Ruffine, L., Henry, P., ... & Moreau, M. (2009). Free gas and gas hydrates from the Sea of Marmara, Turkey: chemical and structural characterization. Chemical Geology, 264(1), 197-206.

Bowers, G. L. (1995). Pore pressure estimation from velocity data: Accounting for overpressure mechanisms besides undercompaction. SPE Drilling & Completion, 10(02), 89-95.

Bowers, G. L. (2002). Detecting high overpressure. The Leading Edge, 21(2), 174-177.

Broichhausen, H., Littke, R., & Hantschel, T. (2005). Mudstone compaction and its influence on overpressure generation, elucidated by a 3D case study in the North Sea. International Journal of Earth Sciences, 94(5-6), 956-978.

Çagatay, M. N., Uçarkus, G., Eris, K. K., Henry, P., Geli, L., & Gasperini, L. (2017, April). Morphotectonics of Sea of Marmara: A Basin on North Anatolian Continental Transform Plate Boundary. In *EGU General Assembly Conference Abstracts* (Vol. 19, p. 4595).

Carcione, J. M., & Cavallini, F. (2002). Poisson's ratio at high pore pressure. Geophysical prospecting, 50(1), 97-106.

Dix, C. H. (1955). Seismic velocities from surface measurements. *Geophysics*, *20*(1), 68-86.

Dupre, S., Scalabrin, C., Grall, C., Augustin, J. M., Henry, P., Şengör, A. M., ... & Géli, L. (2015). Tectonic and sedimentary controls on widespread gas emissions in the Sea of Marmara: Results from systematic, shipborne multibeam echo sounder water column imaging. *Journal of Geophysical Research: Solid Earth*, *120*(5), 2891-2912.

Dutta, N. C. (2002), Geopressure prediction using seismic data: Current status and the road ahead, Geophysics, 67(6), 2012–2041.

Dvorkin, J., Mavko, G., & Nur, A. (1999). Overpressure detection from compressional-and shear-wave data. Geophysical research letters, 26(22), 3417-3420.

Dvorkin, J., & Nur, A. (2002). Critical-porosity models. *MEMOIRS-AMERICAN ASSOCIATION OF PETROLEUM GEOLOGISTS*, 33-42.

Garrels RM, Meckenzie FT (1970) Evolution of sedimentary rocks. W.W. Norton and Co., pp 1–397

Gassmann, F. (1951). Elasticity of porous media. Vierteljahrsschrder Naturforschenden Gesselschaft, 96, 1-23.

Gibson, R. E. (1958), The progress of consolidation in a clay layer increasing in thickness with time, Geotechnique, 8(4), 171–182

Gorur, N., Oktay, F.Y., Seymen, I. and Sengor, A.M.C., 1984. Palaeotectonic evolution of the Tuzgolu Basin Complex, Central Turkey: sedimentary record of the Neo-Tethyan closure. In: J. Dixon and A.H.F. Robertson (Editors), Geological Evolution of the Eastern Mediterranean. Geol. Soc. London~ Spec. Publ., 17: 467-481.

Güreli, O. (2013, May). Boşluk Basıncının ve Sıcaklığın Sismik Hızlar Üzerine Etkileri Pore Pressure and Temperature Effects on the Seismic Velocities. In 19th International Petroleum and Natural Gas Congress and Exhibition of Turkey.

Gürer, Ö. F., Kaymakçı, N., Çakır, Ş., & Özburan, M. (2003). Neotectonics of the southeast Marmara region, NW Anatolia, Turkey. Journal of Asian Earth Sciences, 21(9), 1041-1051.

Han, D. H., & Batzle, M. L. (2004). Gassmann's equation and fluid-saturation effects on seismic velocities. *Geophysics*, *69*(2), 398-405.

Hornbach, M. J., Saffer, D. M., Holbrook, W. S., Van Avendonk, H. J., & Gorman, A. R. (2008). Three-dimensional seismic imaging of the Blake Ridge methane hydrate province: Evidence for large, concentrated zones of gas hydrate and morphologically driven advection. *Journal of Geophysical Research: Solid Earth*, *113*(B7).

Hornbach, M. J., & Manga, M. (2014). The ability of rock physics models to infer marine *in situ* pore pressure. Geochemistry, Geophysics, Geosystems, 15(12), 4769-4780.

Hyndman, R. D., & Spence, G. D. (1992). A seismic study of methane hydrate marine bottom simulating reflectors. Journal of Geophysical Research: Solid Earth, 97(B5), 6

Imren, C., Le Pichon, X., Rangin, C., Demirbağ, E., Ecevitoğlu, B., & Görür, N. (2001). The North Anatolian Fault within the Sea of Marmara: a new interpretation based on multi-channel seismic and multi-beam bathymetry data. *Earth and Planetary Science Letters*, *186*(2), 143-158.

Imren, C., Le Pichon, X., Rangin, C., Demirbağ, E., Ecevitoğlu, B., & Görür, N. (2001). The North Anatolian Fault within the Sea of Marmara: a new interpretation based on multi-channel seismic and multi-beam bathymetry data. *Earth and Planetary Science Letters*, *186*(2), 143-158.

Kitamura, K., Masuda, K., Takahashi, M., & Nishizawa, O. (2006). The influence of pore fluids on seismic wave velocities under high temperature and high-pressure conditions: Development of a new technique with gas apparatus at AIST, Japan. Earth, planets and space, 58(11), 1515-1518.

Le Pichon, X., Taymaz, T., & Sengor, A. M. C. (2000, May). Important problems to be solved in the Sea of Marmara. In *NATO Advanced Research Seminar: Integration of Earth Sciences Research on the 1999 Turkish and Greek Earthquakes and Needs for Future Cooperative Research* (pp. 66-67).

Makse, H. A., N. Gland, D. L. Johnson, and L. Schwartz (2004), Granular packings: Nonlinear elasticity, sound propagation, and collective relaxation dynamics, Phys. Rev. E, 70(6), 061302.

Marmara-1. Final well report, Turkey, 26pp.

Marza, V. I. (2004). On the death toll of the 1999 Izmit (Turkey) major earthquake. *ESC General Assembly Papers, European Seismological Commission, Potsdam*.

Mavko, G., T. Mukerji, and J. Dvorkin (2009), The Rock Physics Handbook: Tools for Seismic Analysis of Porous Media, Cambridge Univ.Press. N. Y.

Mindlin, R. D. (1949), Compliance of elastic bodies in contact, J. Appl. Mech., 16, 259–268

Nur, A., G. Mavko, J. Dvorkin, and D. Galmudi (1998), Critical porosity: A key to relating physical properties to porosity in rocks, Leading Edge, 17(3), 357–362.

Okay, A. I., Demirbağ, E., Kurt, H., Okay, N., & Kuşçu, İ. (1999). An active, deep marine strike-slip basin along the North Anatolian fault in Turkey. *Tectonics*, *18*(1), 129-147.

Okay, A.I., Kaslilar-Ozcan, A., Imren, C., Boztepe-Guney, A., Dermirbag, E., and Kuscu, I., 2000, Active faults and evolving strike-slip basins in the Marmara Sea, northwest Turkey: a multichannel seismic reflection study: Tectonophysics, v. 321, p. 189-218.

Paull, C. K., & Matsumoto, R. (2000). 1. Leg 164 overview. In *Proceedings of the ocean drilling program. Scientific Results* (Vol. 164, pp. 3-10).

Pinar, A., Honkura, Y., & Kuge, K. (2001). Seismic activity triggered by the 1999 Izmit earthquake and its implications for the assessment of future seismic risk. *Geophysical Journal International*, *146*(1), F1-F7.

Prasad, M. (2002). Acoustic measurements in unconsolidated sands at low effective pressure and overpressure detection. Geophysics, 67(2), 405-412.

Rangin, C., Le Pichon, X., Demirbag, E., & Imren, C. (2004). Strain localization in the Sea of Marmara: Propagation of the North Anatolian Fault in a now inactive pull-apart. *Tectonics, 23*(2).

Ruffine, L., Fandino Torres, O., Etoubleau, J., Cheron, S., Donval, J. P., Germain, Y., ... & Gasperini, L. (2012). Geochemical dynamics of the natural-gas hydrate system in the Sea of Marmara, offshore Turkey.

Schmittbuhl, J., Karabulut, H., Lengliné, O., & Bouchon, M. (2016). Seismicity distribution and locking depth along the Main Marmara Fault, Turkey. *Geochemistry, Geophysics, Geosystems, 17*(3), 954-965.

Sengor A.M.C., Gorur, N., Saroglu, F., 1985. Strike–slip faulting and related basin formation in zones of tectonic escape: Turkey as a case study. In: Biddle, K.T., Christie-Blick, N. (Eds.), Strike–Slip Deformation, Basin Formation and Sedimentation, Special Publication Society of Economic Paleontology and Minerology No. 37, pp. 227–264.

Shillington, D. J., Seeber, L., Sorlien, C. C., Steckler, M. S., Kurt, H., Dondurur, D., ... & Gürçay, S. (2012). Evidence for widespread creep on the flanks of the Sea of Marmara transform basin from marine geophysical data.Geology, 40(5), 439-442.

Shuey, R. T. (1985). A simplification of the Zoeppritz equations. Geophysics, 50(4), 609-614.

Steckler, M. S., Cifci, G., Demirbag, E., Akhun, S. D., Büyükasik, E., Cevatoglu, M., ... & Imren, C. (2008, December). Cruise report of TAMAM Project

Straub, C., Kahle, H. G., & Schindler, C. (1997). GPS and geologic estimates of the tectonic activity in the Marmara Sea region, NW Anatolia. Journal of Geophysical Research: Solid Earth (1978–2012), 102(B12), 27587-27601. Oil, M. (1975).

Swarbrick, R. E., Osborne, M. J., & Yardley, G. S. (2002). Comparison of overpressure magnitude resulting from the main generating mechanisms. MEMOIRS-AMERICAN ASSOCIATION OF PETROLEUM GEOLOGISTS, 1-12.

Tary, J. B. (2011). Case studies on fluids and seismicity in submarine environments based on Ocean Bottom Seismometers (OBS) recordings from the Sea of Marmara and application to the Niger Delta (Doctoral dissertation, Université de Bretagne occidentale-Brest).

Taymaz, T., 2001, Active tectonics of the north and central Aegean Sea, Symposia on Seismotectonics of the north-western Anatolia Aegean and Recent Turkish Earthquakes, May 8, 2001, Istanbul Technical University, Maslak, Istanbul.

Yilmaz, Ö. (2001). *Seismic data analysis: Processing, inversion, and interpretation of seismic data*. Society of exploration geophysicists.

Wong, H. K., Lüdmann, T., Ulug, A., & Görür, N. (1995). The Sea of Marmara: a plate boundary sea in an escape tectonic regime. Tectonophysics, 244(4), 231-250.

Wyllie, M. R. J., Gregory, A. R., & Gardner, G. H. F. (1958). An experimental investigation of factors affecting elastic wave velocities in porous media. Geophysics, 23(3), 459-493.